2014

STUDY OF THE DYNAMIC RESPONSE OF MINIMUM WEIGHT STRUCTURES

Peter Thomas Phelps
University of Rhode Island, pphelps@my.uri.edu

STUDY OF THE DYNAMIC RESPONSE OF MINIMUM WEIGHT STRUCTURES

WRITTEN BY

PETER THOMAS PHELPS

A THESIS SUBMITTED IN PARTIAL FULFILLMENT OF THE

REQUIREMENTS FOR THE DEGREE OF MASTER OF SCIENCE

IN

MECHANICAL ENGINEERING AND APPLIED MECHANICS

UNIVERSITY OF RHODE ISLAND

2014

MASTER OF SCIENCE IN MECHANICAL ENGINEERING AND APPLIED MECHANICS THESIS

OF

PETER PHELPS

APPROVED:

Thesis Committee:

Major Professor David Taggart

Arun Shukla

George Tsiatas

Nasser H. Zawia
DEAN OF THE GRADUATE SCHOOL

UNIVERSITY OF RHODE ISLAND
2014

ABSTRACT

Topology optimization is a tool used during the early stages of design to identify configurations that might not be intuitive. In this thesis, topologies that have been optimized for static loading are evaluated for their performance under dynamic loading conditions. The response of these structures to dynamic loads is not understood and has yet to be investigated. This study seeks to compare the dynamic response of structures that have been optimized for static stiffness to more traditional weight minimizing structures consisting of periodic geometric patterns. A domain is optimized for a loading case using an available static optimization scheme. The domain and case were chosen specifically so that it can be tested dynamically in the laboratory, using an instrumented drop weight impact test machine. The drop test experiment is simulated using a Finite Element Analysis (FEA). The experimental data for a particular topology with a low volume fraction is used to validate the FEA model. Similar topologies with higher volume fraction are then evaluated by FEA simulations.

Understanding the dynamic response of statically optimized structures will provide insight into the development of an algorithm that could optimize a structure subjected to dynamic loading conditions. Such an algorithm would be very useful in the design of lightweight bulkheads for underwater vehicles, torpedoes, cruise missiles and other aerospace applications. In such applications, structural weight savings are critical and static loads are well defined. However, these structures are also subjected to dynamic loads which must be characterized and taken into account during the design phase.

As expected, the optimized topologies exhibit very high stiffness when subjected to either static or dynamic loading. At low energy levels where no critical damage is observed, optimized topologies perform better with a much high stiffness before and after impact and deflected less during the impact. The optimized topologies perform better than the traditional topologies until the kinetic energy increases enough to compromise the structure in the form of tensile failures, as observed in the lower volume fraction topologies. At critical high impact conditions, however, high stiffness can prove to be a hindrance. Statically optimized structures are uniformly stressed at all material points. Under high impact conditions, the structure is quickly loaded to a failure state, typically tensile failure in regions subjected to stress concentrations or compressive failure of slender compressive members. Such failures dramatically reduce the stiffness of the structure since the optimized structure requires all members to remain intact to effectively transmit the loads. As a result, due to their high stiffness and loss of structural integrity after initial failure, the statically optimized structures do not allow sufficient time prior to failure to decelerate the dropped mass. By comparison, the more traditional lightweight structures have lower stiffness and decelerate the mass over a longer distance and time. These structures also experienced localized failures, most often due to buckling, but were able to carry loads effectively after failures because the structure had multiple load paths. Topologies optimized for stiffness do not perform well under high impact conditions because some compliance is required to effectively absorb high impact energy.

One of the objectives of this study is to provide insights that can be used to develop new algorithms for the optimization of structures for resisting dynamic loads. The results of this study reveal that the optimization schemes for a structure's dynamic response will need to identify design parameters that provide an optimal combination of initial stiffness, initial failure, and post-failure energy absorption.

ACKNOWLEDGEMENT

I would like to express my gratitude to my advisor, Professor David Taggart, for his support, patience, and encouragement throughout my graduate studies. I appreciate how generous he is with his time and his input. His technical and editorial advice was essential to the completion of this thesis. It is a pleasure to work with him and I hope to continue to in the future.

I would also like to thank the rest of my thesis committee: Professor Shukla, Professor Tsiatas, and Professor Bradshaw.

I would also like to my fellow lab mates, Prathmesh Parrikar, Sachin Gupta, Payam Fahr, Emad Makki, and Nicholas Heeder.

DEDICATION

I dedicate this thesis to my family. My children, Wyatt, Logan, Seana, Marie and Elizabeth remind me how far I have come to get to this point. Norman and Harle Phelps, my parents, remind me that hard work and patience pay off. Tara, my wife, challenges me to be spontaneous and keep moving forward.

TABLE OF CONTENTS

LIST OF TABLES

LIST OF FIGURES

1. INTRODUCTION

1.1 LITERATURE REVIEW

Advancements in topology optimization date back to the work of Michell (Michell 1904), where he proved that an optimal truss must follow the orthogonal network of lines of maximum and minimum strain in a constant-magnitude strain field. The material is optimized such that the structure is stressed evenly throughout. Increasing the load to critical levels would theoretically cause the structure to fail everywhere at once. The failure criteria for Michell structures was stated as "the greatest tensile stress allowable in the material which is to be employed is P, and the greatest compressive stress Q, the least volume of material in a given frame, consistent with security" (Michell 1904). The term security is taken to mean the failure of the structure. Figure 1shows a case described by Michell in his 1904 paper. The case has a single load, a force 'F' applied at point 'A'. The boundary conditions of this case is an equal and opposite force and a couple, of moment 'F x AB' applied at 'B'.

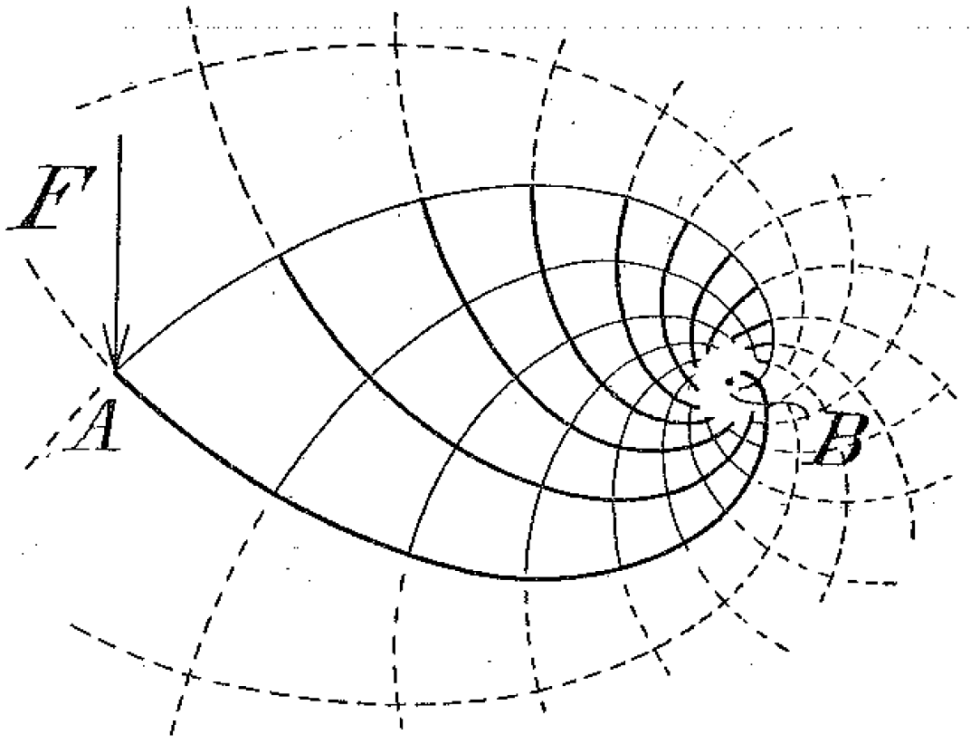

Figure 1- Michell Topology

The minimum weight frame to support the load from B is depicted by the solid black lines. Michell's work on optimization has been applied and used as a base line for the development of several numerical methods based on the finite element method to find minimal weight structures for complex problems. One well known numerical optimization method, referred to as "solid, isotropic microstructure with penalty" (SIMP) was developed by Rozvany et al. (Rozvany 1992). The SIMP method requires the user to select a penalization factor, typically around 3.0, and filtering parameters to avoid a numerical instability known as checker boarding. A simpler evolutionary procedure for structural optimization was proposed by Xie and Steven (Xie 1993). This procedure uses an iterative finite element analysis on the domain in which a rejection criterion (RC) to remove low stress elements from the domain. If the RC is taken to be the von Mises effective stress, if the rejection criterion of an element is

below the rejection ratio (RR) times the maximum von Mises stress for that iteration, then that element is deleted from the domain. The process continues with the RR increasing as the iterations advance. The drawback to this method is that once an element is deleted it cannot be reintroduced. The statically optimized topologies investigated in this study are the result of a method called the prescribed material redistribution (PMR) developed by Taggart et al. (Taggart 2008) which is described below. . Numerical topology optimization methods such as these have been integrated into several leading FEA and CAD software packages such as Abaqus (Simulia) and HyperWorks (Altair). These tools are used to guide designers and engineers by showing optimized topologies that they can incorporate into their designs.

Topology optimization starts by creating a domain to be optimized. In the optimized design, only a fraction of the domain will be solid material and the rest of the domain will be void. The boundary conditions and loads are specified to completely define the case. As stated about, the prescribed material redistribution (PMR) method (Taggart 2008) will be used in this study. In previous work by Taggart et al. (Taggart 2008) (Taggat 2010), the PMR method has been validated by comparison with well-known classical two dimensional topology. These are shown in Figure 2. Case 1 shows a Michell arch (Michell 1904). This case has a domain above the loading in the center and the simply supported (pin / roller) boundary conditions in the corners. Case 2 is similar to Case 1 but with pin supports a both corners. Expanding the domain for Case 3 mirrors the structure of Case 2 below the horizontal. Case 4 is a cantilever proven to be the optimal structure by Chan (Chan December 1960).

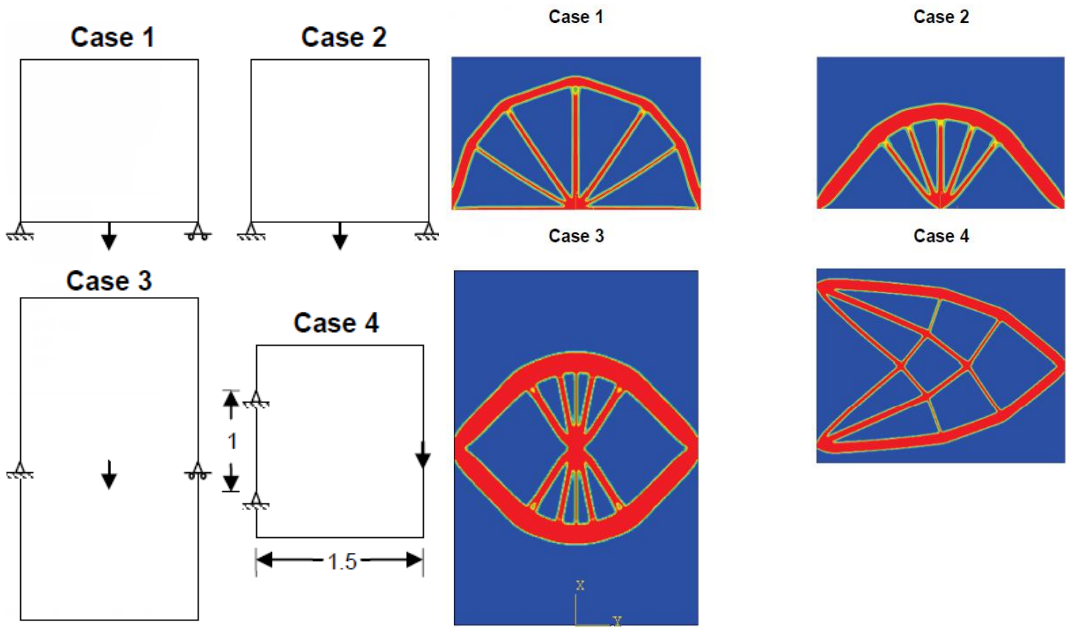

Figure 2- Minimal Weight Structures (Taggart 2008)

1.2 PRESCRIBED MATERIAL REDISTRIBUTION

The Prescribed Material Redistribution (PMR) method was developed by Taggart and Dewhurst (Taggart 2008). In the procedure the fraction of the domain that is intended to be filled is specified. This volume fraction (VF) would be greater than zero and less than unity. Initially, the corresponding total material mass is distributed uniformly throughout the domain. As a result, the initial density of all the nodes is given as shown in Equation 1.

$$\rho = V_f / V_D \tag{1}$$

Where the final volume of the solid material is V_f, and V_D is the volume of the entire domain. The PMR algorithm has previously been implemented in MATLAB for both 2-D and 3-D (Okruta 2014) topology optimization problems. For these codes, the user must create an input file that defines the size of the domain, loads, boundary conditions, volume fraction and number of steps. A finite element analysis is

conducted on the domain for every iteration. Since the density of each node is updated in each iteration, the element stiffness matrix for each element must be recomputed at every iteration. The Young's modulus, E_e, of each element is taken to be proportional to fully dense Young's modulus, E_d and the density, ρ_e, of the particular element as shown in Eq. 2.

$$E_e = E_d \rho_e \tag{2}$$

Where the element density is computed as the average of the nodal densities for that element. At the end of each iteration, the material is redistributed throughout the domain as prescribed below. The densities of nodes with high strain energy are increased and the densities of nodes with low strain energy are reduced. A gradual transition from the initial state of uniformly distributed material to a bi-modal state of fully dense and fully voided regions is imposed through a family of Beta functions as shown in Figure 3 (Taggat 2010).

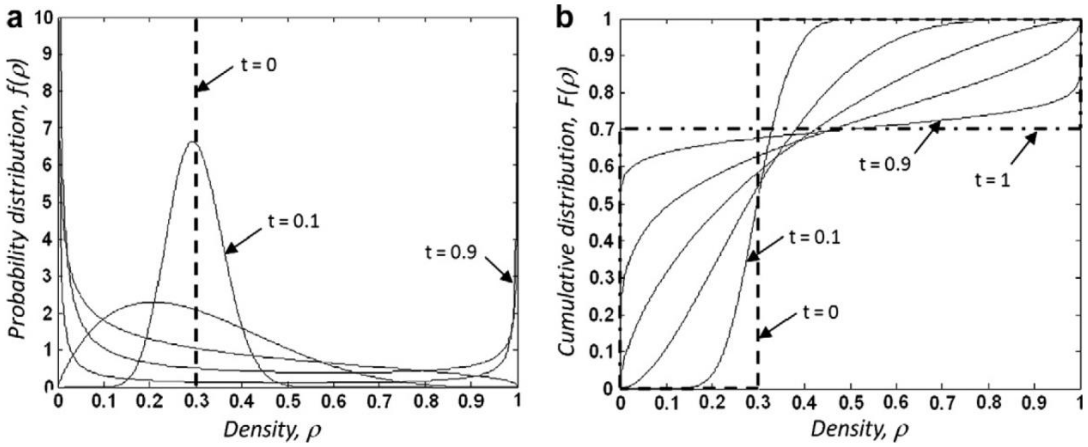

Figure 3 - Beta distributions (a) density (b) cumulative, showing transition from initial to final densities (Taggat 2010)

While the PMR method gives reasonable topologies in just a few iterations, for well-defined topologies at least 25 iterations are recommended. In this study one hundred iterations were used when creating topologies with the PMR program.

1.3 TOPOLOGIES OF INTEREST

The experimental study required the identification of a topology that could be tested in the lab under dynamic conditions. Hence, the configuration of the drop weight test equipment dictated the geometry of the domain, loading conditions and boundary conditions. As shown in Figure 4, the domain to be optimized is a rectangular region eight inches wide and four inches high. The support boundary conditions consist of fixed supports on both the left and right hand side of the domain. To simulate the effect of the striker, a pressure load is applied on a 1 inch region in the center at the top of the h.

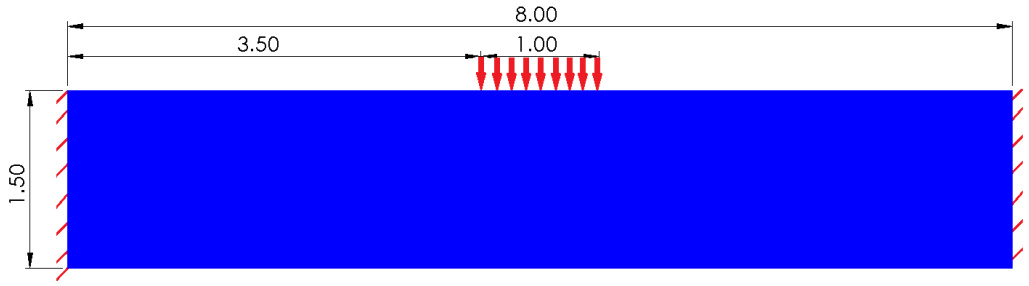

Figure 4 - Sample Domain

To save computational time a symmetry plane is imposed at the middle of the domain; reducing the domain size in half and changing the boundary condition on the right edge to a symmetry condition (see Figure 5). Along the right hand edge, nodes are free to move in the Y direction but are constrained in the X direction.

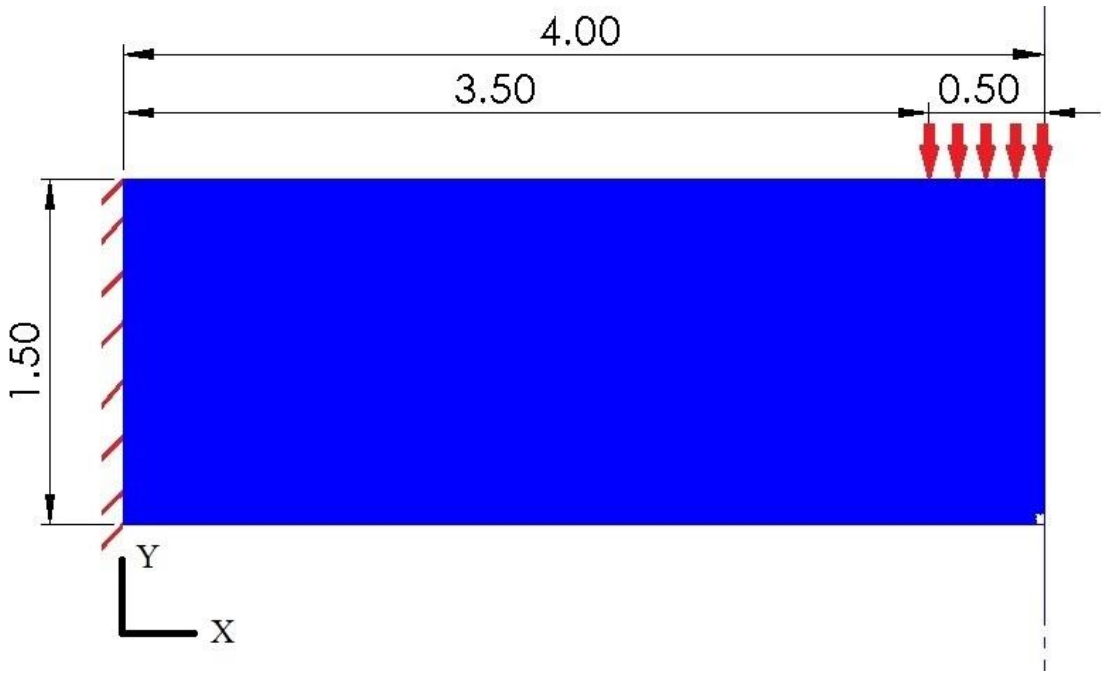

Figure 5- Simplified PMR Domain

Figure 6 shows the evolution of the PMR imposed density fields. In iteration 2 one notices that the domain is largely uniform. As the iterations continue, low density areas are shown in red while higher density areas are shown in blue. At iteration 100 the topology has converged to fully dense regions and completely void regions.

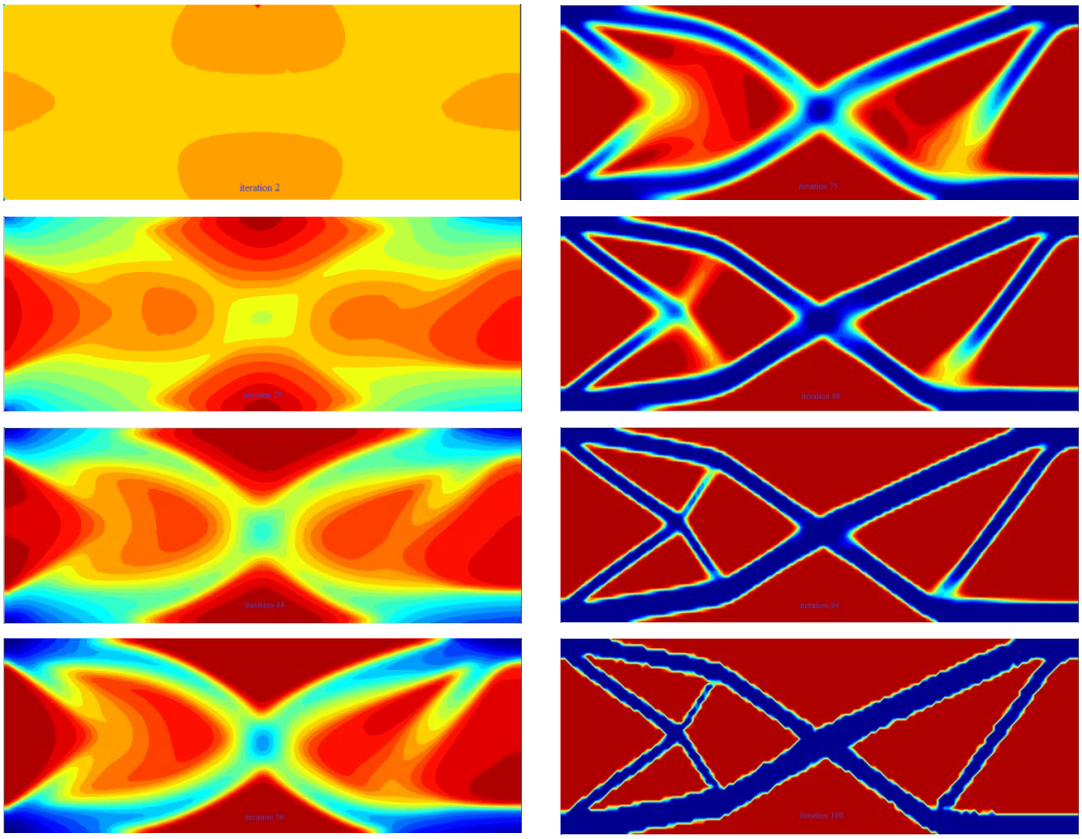

Figure 6- PMR Progression iterations 2, 29, 44, 56, 75, 88, 94 & 100

Nine topologies were created using the PMR method. For all cases, the domain was discretized into as 240 elements in the X direction and 90 elements in the Y direction. The pressure load was applied over 30 elements in the upper right hand corner of the domain. The profiles are designated PMR1 through PMR9 with increasing volume fractions from 0.20 to 0.60. The resulting profiles are shown in Figure 7. The Matlab input file used to call the PMR program is APPENDIX 3.

Table 1 – Profile Designation and Volume Fractions

	PMR1	PMR2	PMR3	PMR4	PMR5	PMR6	PMR7	PMR8	PMR9
Volume Fraction	.20	.25	.30	.35	.40	.45	.50	.55	.60
Figure 7	a)	b)	c)	d)	e)	f)	g)	h)	i)

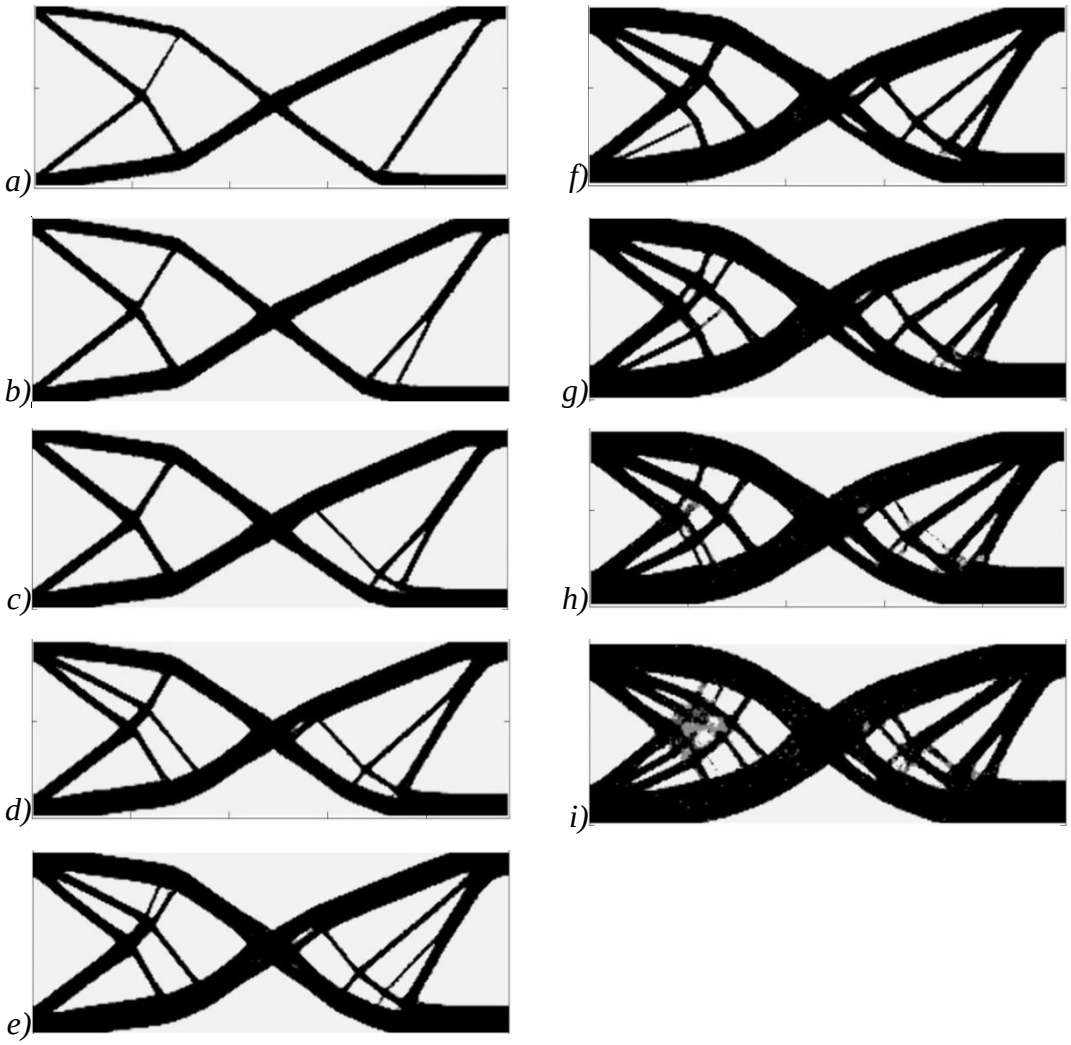

Figure 7- PMR Profiles

The profiles created by the PMR show a similar topology. The outer members are the thickest. They create an elongated X shape pattern that meets halfway through the domain and start and end at the corners of the domain. The large outer members are supported by smaller internal members that reinforce the structure. The left side of the domain bears a strong resemblance to the Chan cantilever shown in Case 4 of Figure 2. The PMR optimized topologies are compared to a more traditional truss structure. A more traditional topology for this kind of application would be a truss structure made of elements of similar thicknesses. For simplicity, a truss structure

made of a single row of equilateral triangles (See Figure 8) was selected for comparison to the optimized topologies. Note that the configuration at the impact location consists of flat surface reinforced by the peak of the center triangle... It is of interest to note that the PMR profiles share this attribute. They each have a nearly equilateral triangular shaped void below the impact location (See Figure 9)

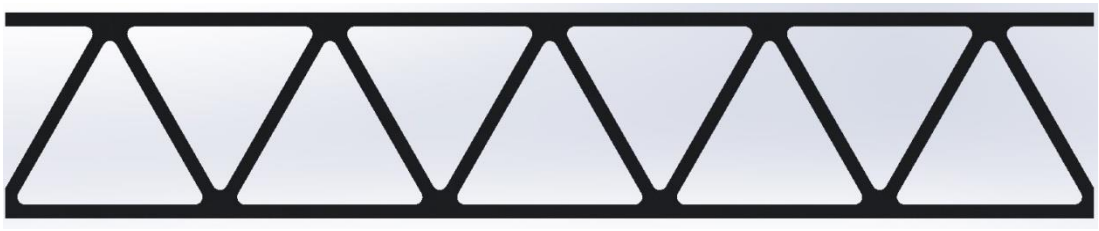

Figure 8- Typical Truss Structure Volume Fraction 0.25

For the traditional truss structure, the thickness of the truss members is uniform throughout. This thickness is adjusted until the volume of the truss structure matched the corresponding PMR case. The corners of the triangles filleted with a constant radius of 7/128".

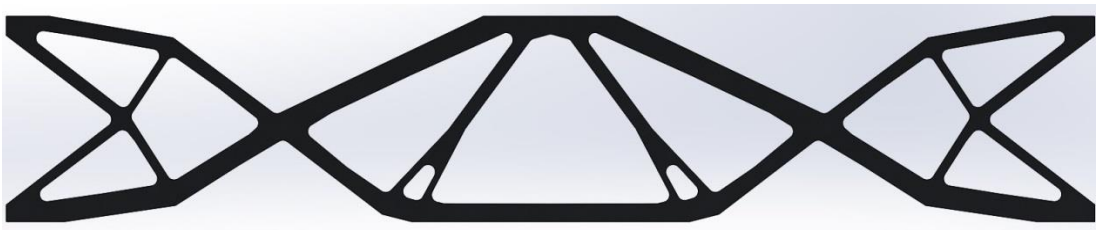

Figure 9 - PMR2 Volume Fraction 0.25

2. EXPERIMENTAL METHODS

In order to compare topologies generated by the PMR algorithm compares to more traditional truss topologies, a number of profiles need to be evaluated. Due to the time and expense associated with experimental characterizations, only two topologies were selected for laboratory testing. The laboratory experiments consist of an instrumented drop weight machine to induce a dynamic impact. The test specimen spans the eight inches and is clamped and supported at both ends. The specimen is impacted on the top side of the span at the midpoint of the specimen. The results of the experiments are correlated with finite element analysis to demonstrate that the model accurately simulates the experiment. Then, additional topologies are evaluated numerically under various load condition using FEA. The maximum and permanent deflections at the top and bottom of the midpoint of the specimen are used to validate the FEA model and evaluate the performance of each design. Experimentally, replicates of each topology were tested under identical load conditions to verify repeatability of the results.

2.1 TEST SAMPLE PREPARATION

All PMR generated topologies are converted from a digital image file to a dxf file. A dxf file is drawing interchange format used by AutoCAD, Solidworks and many other CAD programs. The dxf file is created by importing the image file into a Solidworks sketch. The image is scaled so that the width and height of the domain match the desired part dimensions. In this case, 240 nodes equal 4 inches and 90 nodes equal 1.5 inches. Then the outline of the profile is drawn in the sketch using the Solidworks sketch tools. As shown in Figure 7, the edges of the profile are not

smooth. Sketching over the profile requires the user to approximate the profile with a series of lines shown in blue in Figure 10. This process is in the spirit of topology optimization software in which the results are to be used as a guide for the designer. For this study, the profiles were followed as accurately as possible. Since there is human involvement in this step, some error will occur.

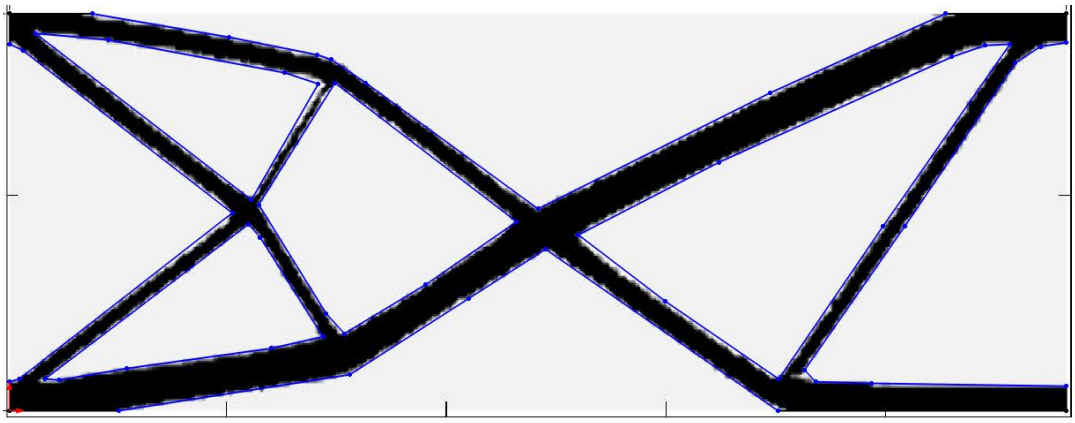

Figure 10- DXF Overlay of PMR1 Image

After smoothing the members, fillets are added in the internal structure. The fillets are necessary both to minimize stress concentration effects and machining of sharp internal corners is not feasible. The radius of these fillets was taken to be 7/128 of an inch. Through smoothing of the members and addition of fillets, the volume added to the original PMR profile was 0.53% of the entire design domain. For attachment to the support fixtures, solid blocks of material are added to the left and right of the design domain. Bolted joints are used to rigidly attach the specimen to the fixture, creating the desired fixed boundary condition on the left and right side of the design domain. The front face of the profile is saved as a dxf file (See Figure 11). The CNC milling machine can use this file to machine the samples. This profile can also be used later by Abaqus for the FEA.

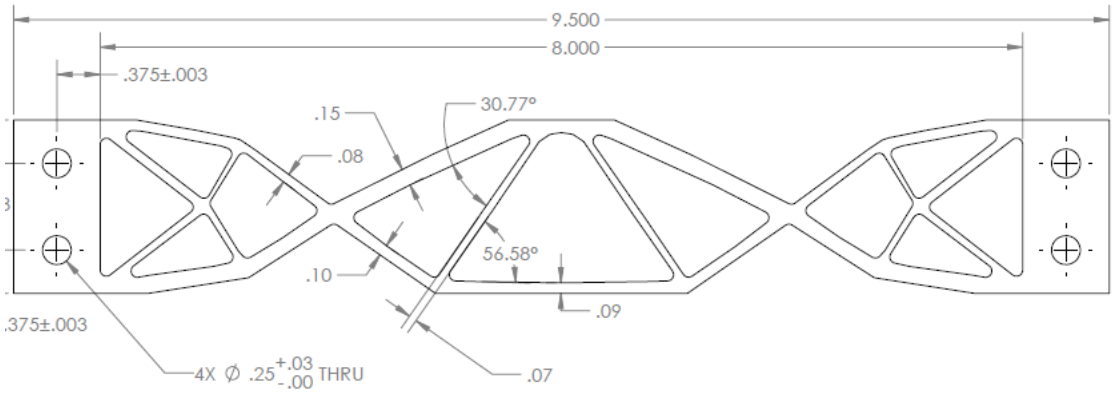

Figure 11 - PMR1 Experimental Specimen VF0.20

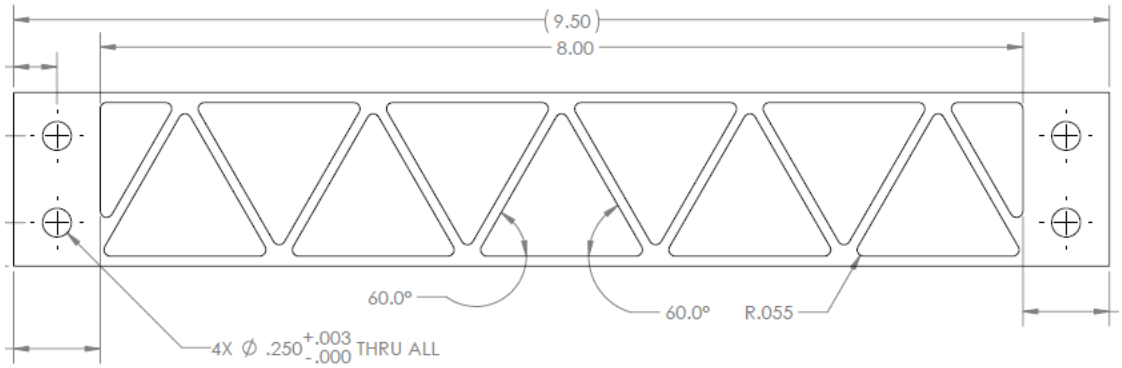

Figure 12 – TRI1 Truss Experimental Specimen VF0.20

Samples were machined from Aluminum 6061-T651 bar stock 1.5” in height and 0.5 inches thick. The stock was cut to a length of 9.5”. The interior profile was then milled on a CNC machine. The dxf profile was read by the CNC machine and a two stage cutting profile was created. A large diameter end mill was used to remove the bulk of the material. Then, the smaller 7/64” end mill removed the remainder of the material and created the small fillets as required.

2.2 EXPERIMENTAL TEST SETUP

The experimental testing was conducted using an Instron 9210 model drop tower impact tester. The tester is equipped with a one channel load cell that captures load, energy, velocity, and deflection at a frequency of 410 kHz. The mounting fixture

is installed below the impact table so that high speed images of the experiments could be recorded. A digital high speed camera is used to record the events at 27,000 frames per second. The test samples are painted white with black speckles so that subsequent Digital Image Correlation (DIC) can be applied to determine the experimental displacement fields.

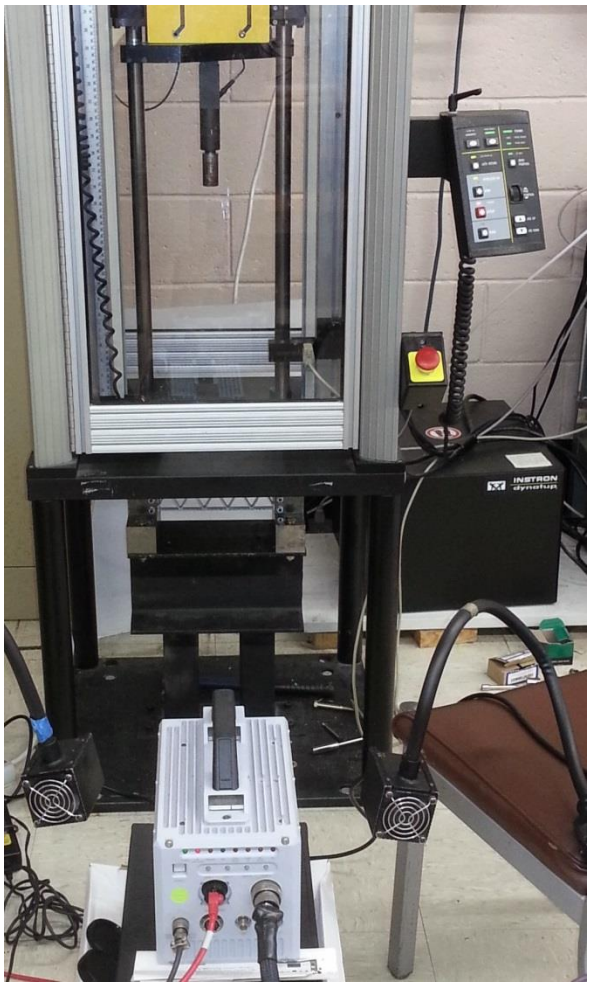

Figure 13 - Experimental Setup

As shown in Figure 13, a specialized fixture is used to mount the specimens beneath the base of the Instron machine. The drawings for the fixture are given in APPENDIX 4. As shown in Figure 11 and Figure 12, each sample has a clamping area at each end of the design domain. The clamping area is inserted into the steel end

blocks on each side of the fixture. Then four quarter inch shoulder bolts are passed through the end blocks and specimen. Two shoulder bolts are on each side of the fixture. The specimen fits snugly into the end blocks. Each face of the clamping area is flush with either the end blocks or the crossbar below. Only the top of the clamping area is exposed. In this case the shoulder bolts and static friction keep the specimen from moving upward. The end blocks are bolted and pinned to the crossbar below. This part is also made of steel. The crossbar is bolted to a steel beam support below the Instron using four 3/8" bolts (see Figure 14).

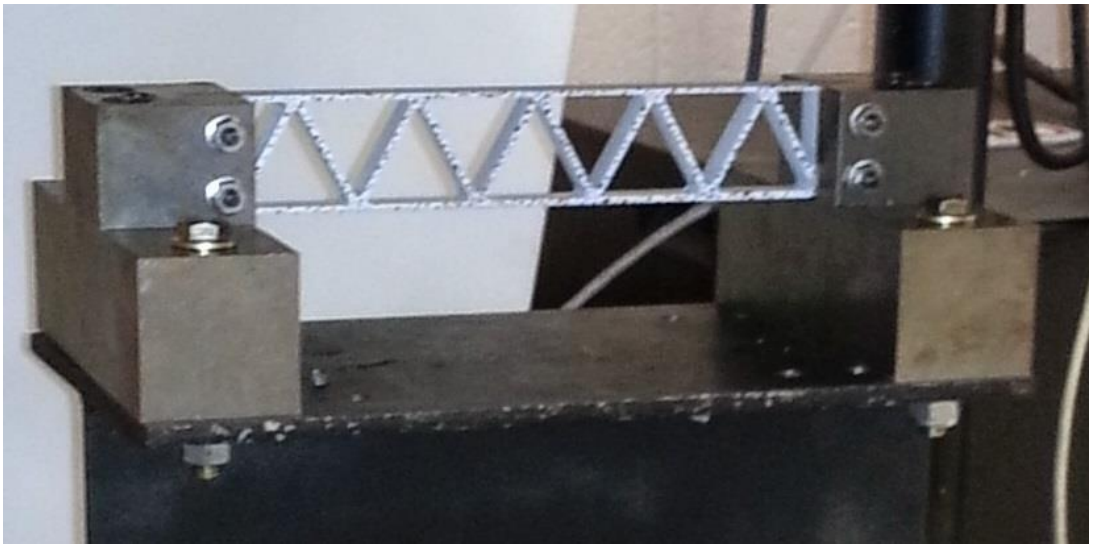

Figure 14 - Sample Fixture

Six experiments were conducted. A one inch in diameter flat cylindrical steel tup was used at the striker in each experiment. The tup and bolt have a combined mass of 1.08 kg. The reaction plate and bolts have a mass of 1.39 kg. The cross head has a mass of 4.79 kg. The mass of the total assembly is 7.26 kg. Two blocks with a mass of 5.02 kg each were added to the assembly for experiments 1 and 2. For experiments 3 through 6 only one block with a mass of 5.02 kg is used. And for experiments 5 and 6 the drop height was reduced from 0.675 meters to 0.525 meters.

The impact speed and kinetic energy are calculated from the total mass of the crosshead assembly and the drop height. Neglecting friction, the potential energy of the crosshead equals the kinetic energy at impact (Equation 3).

$$PE = mgh = KE = \frac{1}{2}\, mV^2 \tag{3}$$

Solving for velocity gives

$$V = \sqrt{2gh} \tag{4}$$

The three different combinations of drop height and mass resulted in three different kinetic energies at impact as shown in Table 2. Samples designated P1 through P3 have the profile PMR1 machined into the design area. Samples designated T1 through T3 have the profile TRI1 machined into the design area.

Table 2 – Experimental Test Parameters

Experiment	Sample	Total Weight [kg]	Drop Height [m]	Impact Speed [m/s]	Kinetic Energy [J]
1	P1	17.300	0.6750	3.639	114.6
2	T1	17.300	0.6750	3.639	114.6
3	P2	12.280	0.6750	3.639	81.3
4	T2	12.280	0.6750	3.639	81.3
5	P3	12.280	0.5250	3.209	63.2
6	T3	12.280	0.5250	3.209	63.2

The mass of each sample (see Table 3) was measured before drop testing. For each replicate pair experiment, the mass of the traditional sample is a greater than that of the PMR optimized sample. This difference may lead to improved performance of give the traditional samples as compared to the PMR samples. The largest difference was between sample P3 and T3. The difference was 1.4 grams. Due to a

manufacturing error, samples P1 through P3 and T1 through T3 had larger holes drilled into the clamping area. The holes were specified to be 0.25" but were drilled out to 0.27". Sample T3 is manufactured without this error and as a result has a greater mass. This explains why sample T3 has the highest mass of all the samples tested. Samples with the larger holes were repaired by machining the holes to 5/16 of an inch and then pressing brass bushings into the holes. The bushings have an external diameter of 5/16" and an internal diameter of ¼". Without the manufacturing anomaly, the difference in the mass of the samples is small, 0.6% at maximum.

Table 3- Sample Masses

Sample	Weight [g]	Sample	Weight [g]
P1	97.1	T1	97.4
P2	96.5	T2	97.1
P3	96.9	T3	98.3

2.3 EXPERIMENTAL RESULTS

The data acquisition during the drop test machine was limited to only 13 milliseconds after impact. In all the experiments the contact time between the tup and sample were longer than this. The samples with the PMR1 profile, designated P1 through P3, showed considerably higher peak loads than the samples with the traditional profile TRI1 as shown in Figure 15 and Table 4.

Table 4 - Maximum Load Cell Values

	Sample	Max Load [kN]	Max Energy [J]	Max Velocity [m/s]
Experiment 1	P1	15.3	117.0	3.700
Experiment 2	T1	8.4	119.5	3.682
Experiment 3	P2	15.0	84.9	3.678
Experiment 4	T2	9.3	85.1	3.690
Experiment 5	P3	14.8	66.4	3.260
Experiment 6	T3	9.8	66.0	3.253

The traditional profiles plateau at their peak load for over two milliseconds before finally dropping. Comparing the load curves between the PMR samples and traditional samples reveals that these topologies exhibit dramatic differences under dynamic loading conditions. Figure 16 shows the first pair of samples, sample P1 and T1. These samples are impacted by the highest kinetic energy, 118 Joules. They are both good representative of the load profile for each topology. The PMR profiles show a high load initially followed by a rapid drop in load. By comparison, the traditional profiles reach a peak load far below the corresponding PMR response but maintain that load level for a longer time period. The test samples were too thin to acquire the displacements across the entire sample. However, the displacements at the middle of the sample on the top and bottom were determined from the images (See Table 5).

Table 5 - Experimental Deflections

Sample	DIC Max Deflection Top Middle [mm]	Time to Max Deflection [ms]	Sample	DIC Max Deflection Top Middle [mm]	Time to Max Deflection [ms]
P1	31.0	12.0	T1	23.8	10.3
P2	25.7	11.4	T2	15.2	11.4
P3	17.0	15.6	T3	9.7	6.5

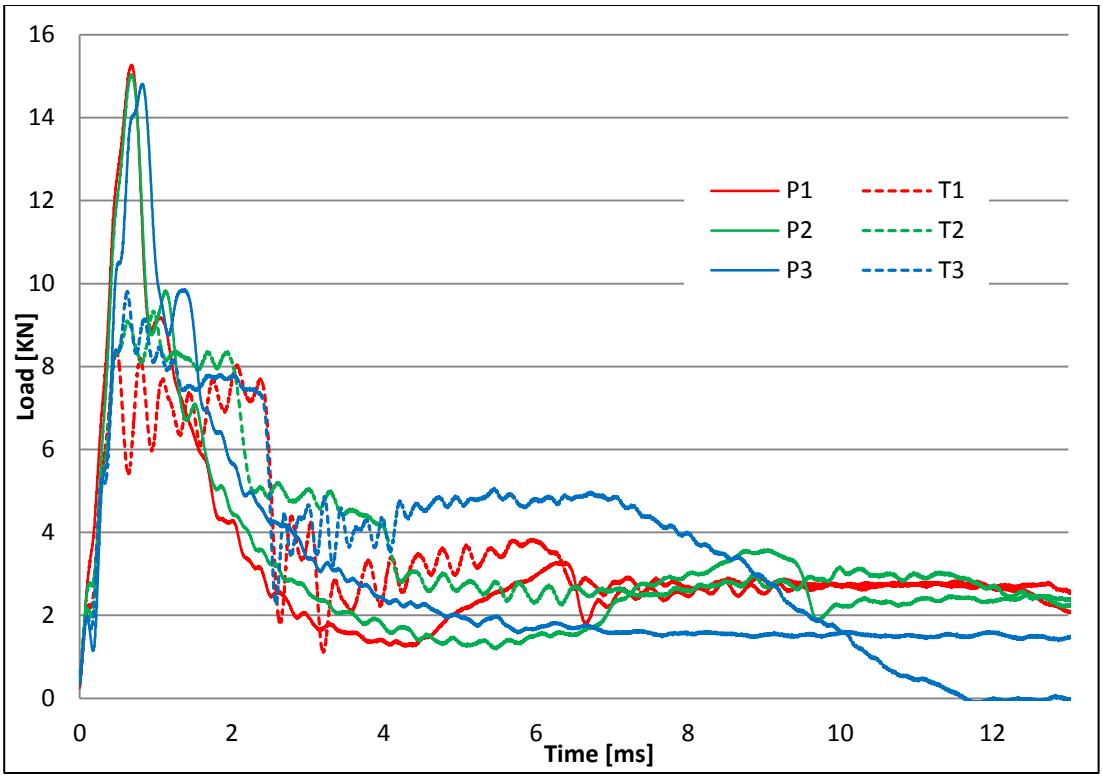

Figure 15 - Experimental Loads

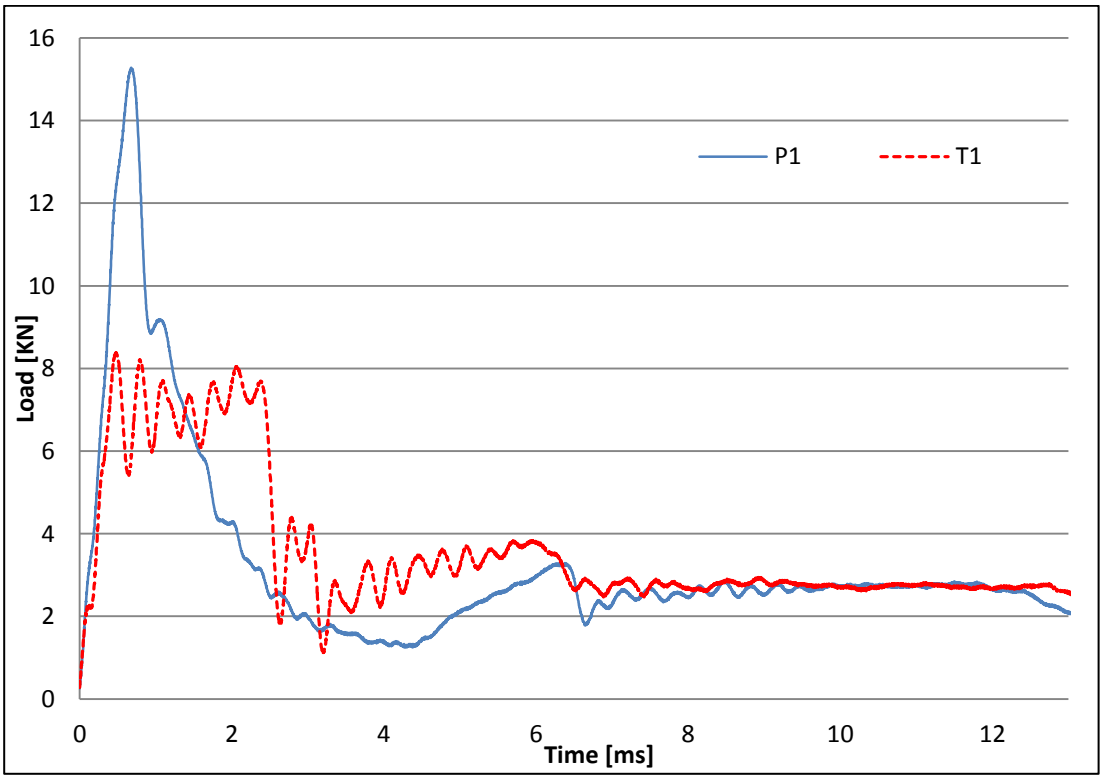

Figure 16 - Experimental Loads First Pair

The kinetic energy lost from the crosshead was recorded by the drop test machine. Figure 17 shows the plot for all six experiments. The typical samples are represented as dashed lines while the PMR samples are solid. In all the experiments half of the energy is absorbed by the sample in the first two milliseconds. This is typically when the sample undergoes the most deformation either by buckling or tensile failure. During this time, the PMR samples show a steeper slope than their typical profiles. This indicates that the PMR samples are absorbing energy more quickly than the typical sample. By four milliseconds all typical samples surpass their PMR counterparts in energy absorbed. It can be clearly seen that in the case of sample T3 energy is returned to the crosshead. Sample T3 was able to absorb kinetic energy of the crosshead, store it as elastic strain energy and return that energy back to the crosshead in the form of kinetic energy. This can also be seen in sample T2 but it is not as prominent. This is a desired attribute in structures designed for impact loadings.

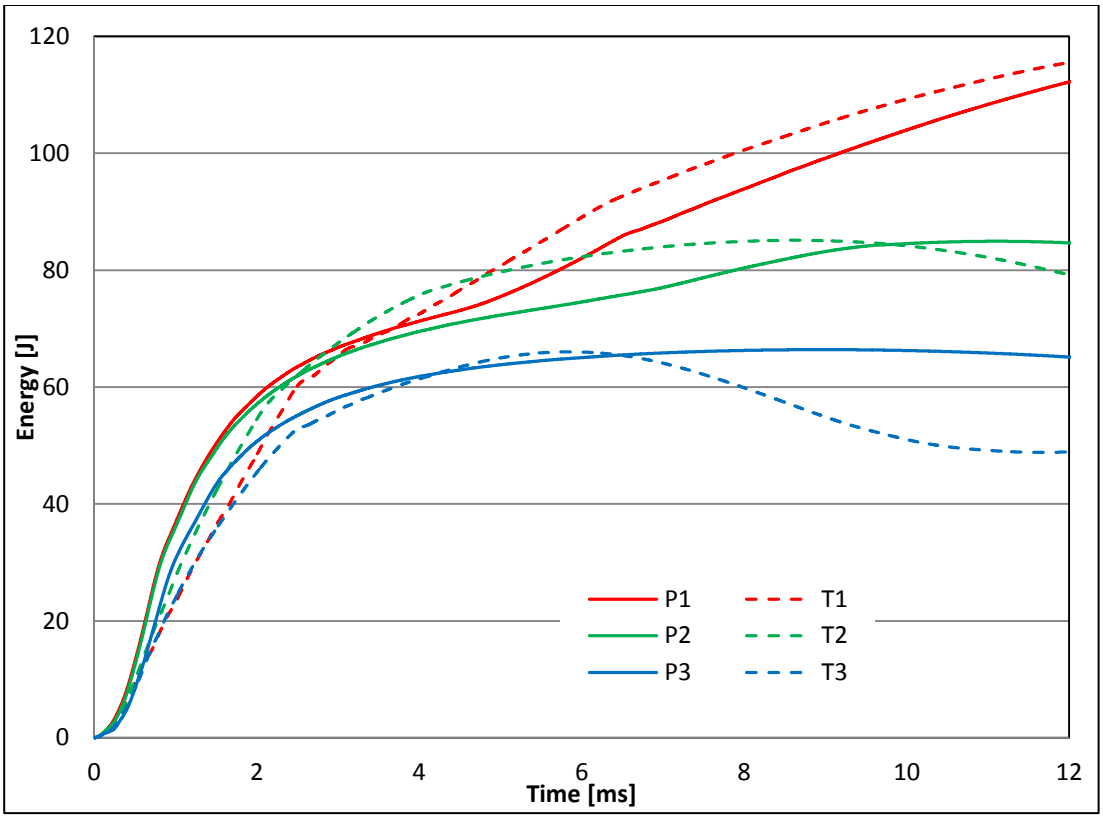

Figure 17- Kinetic Energy Lost from Crosshead

Four experiments were conducted with an impact velocity of 3.6 meters per second. Two experiments were conducted with an impact velocity of 3.2 meters per second. Figure 18 shows us that the PMR profiles quickly decelerate the crosshead during the first two milliseconds. The velocity profiles of P1 through P3 are irregular while the typical samples show as steady deceleration. This change from a quick deceleration to a more gradual one happens early and allows for the typical profiles to stop the mass of the crosshead before the PMR profiles. In fact sample T2 was a high velocity impact and was able to stop its mass in 8.6 milliseconds. This faster than sample P3 which was a lower velocity impact. It took sample P3 9 milliseconds to arrest the crosshead.

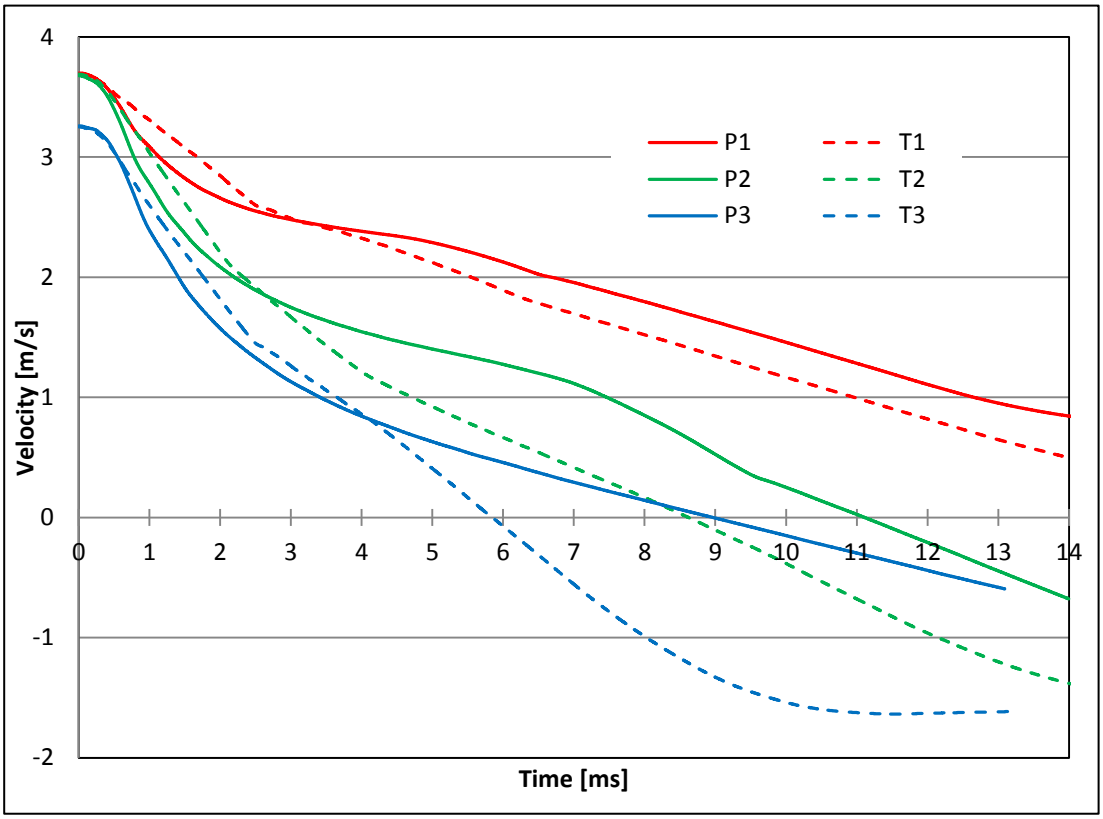

Figure 18 - Velocity of Crosshead

The experimental displacements again show us that the PMR profiles are indeed stiffer initially but lose their stiffness over time. It should be noted that the difference in displacements initially is small (See Figure 19). The PMR profiles differ much greater at the experiment comes to close. Sample P3 shows a steady trend up in displacement, then levels off and returns back to zero.

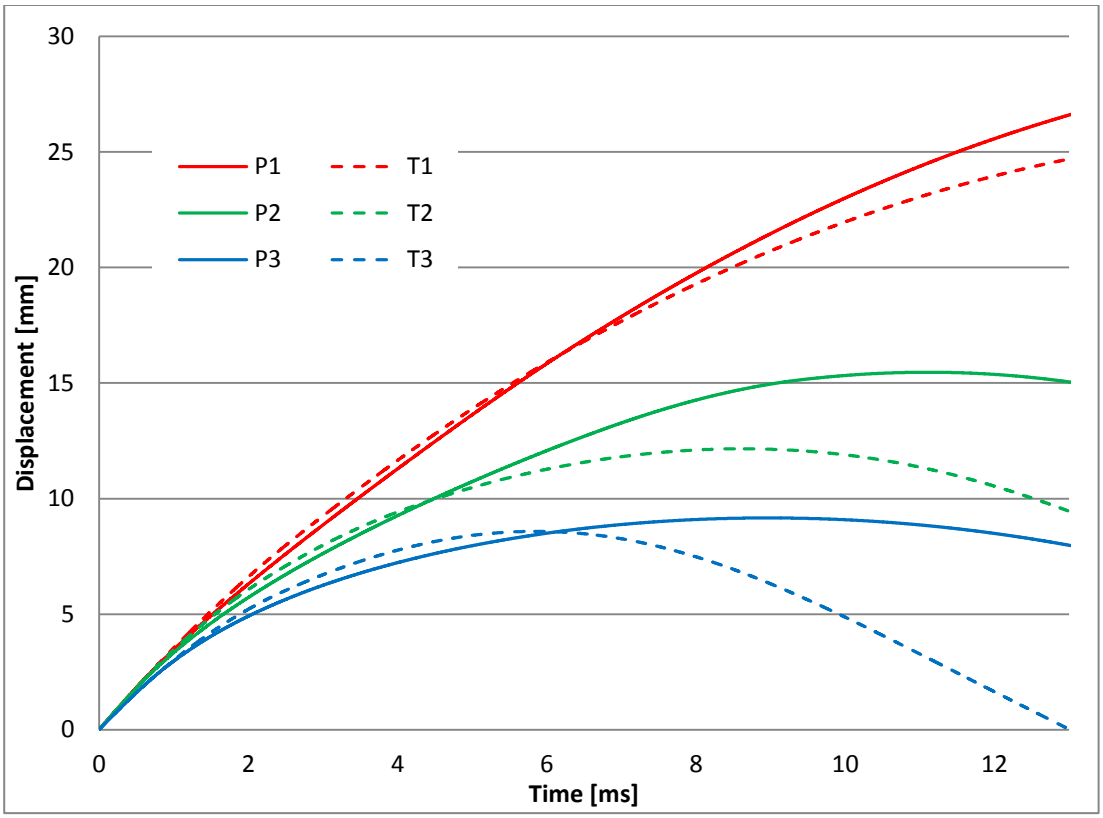

Figure 19- Crosshead Displacements

For the first experiment, Figure 19 shows results the deformation of sample P1 at several points during the impact event. This experiment is one of the highest energy experiments. Sample P1 begins to buckle after 0.66 milliseconds of contact, at the time of the peak load. It can be seen that even with a high speed camera, the image is blurry because it is buckling at a high rate of speed. After 6.5 milliseconds the internal member touches the bottom member and shears into three pieces. It takes 12 milliseconds for the structure to arrest the crosshead and reach its maximum deflection of 31 millimeters. After this experiment, sample P1 is observed to have four members suffer considerable damage. The large outer member at the point of impact buckled

and rebounded slightly. The two internal members below the point of impact buckled severely and one eventually failed.

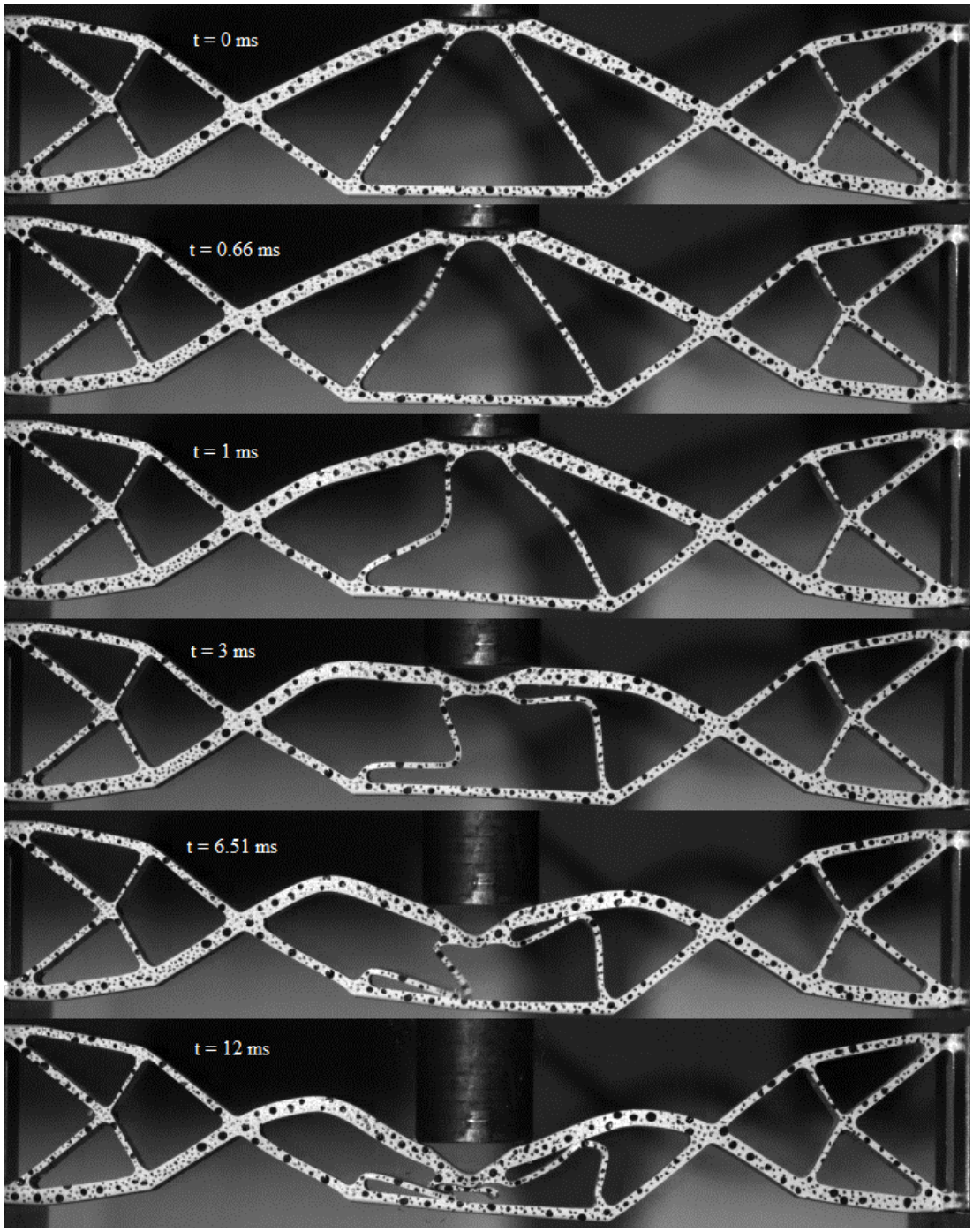

Figure 20 - Experiment 1 Sample P1

The second experiment is also a high energy impact. The kinetic energy of the cross head is 114 Joules. Sample T1 reached its max load sooner at .47 milliseconds. A member on the top of the domain was the first to buckle as shown in Figure 23. This is not surprising since it is in direct contact with the tup. The load plateaus until 2.62 milliseconds when the load drops and a member on the top far right side breaks. After 4.4 milliseconds the member on the top far left side breaks in a similar fashion. Both members were under tension and necking at the point of failure is present. Both failure surfaces are rough (See Figure 21). This indicates a high energy crack because the surface area created is large when compared to the nominal cross sectional area at this point.

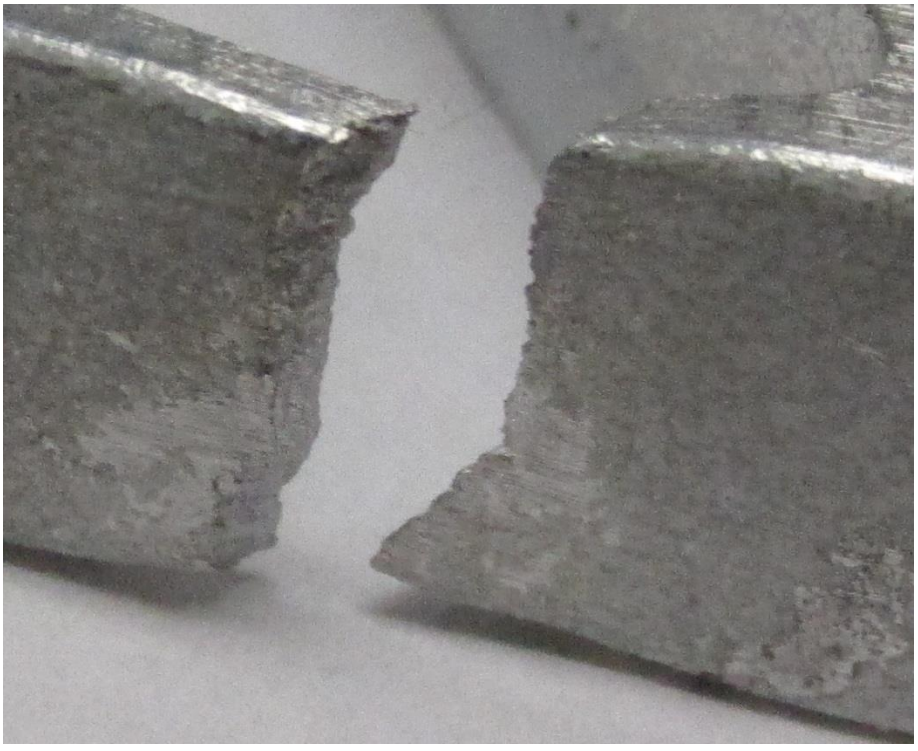

Figure 21- Sample T1 Top Left Failure

The crosshead is arrested after 11.4 milliseconds. At this time the max deflection of the top mid point of the sample occurs and it is 23.8 millimeters. After 20.5 milliseconds the tup loses contact with the sample. After the event four members were severly damaged. Two members failed in tension and two buckled completely.

Experiment 3 was conducted with sample P2. The kinetic energy of the crosshead at impact is 81 Joules. The max load occurred after 0.8 milliseconds. After 9.6 milliseconds an internal member shears after severe buckling. The crosshead is arrested after 15.6 milliseconds. The max deflection of the top middle is 25.7 millimeters. The tup loses contact with the sample after 24.5 milliseconds.

The reduction in kinetic energy used for Experiment 4 allowed for Sample T2 to escape without any failures in tension. However, at the locations where Sample T1 failed in tension slight necking can be observed. A top view of this inelastic deformation can be seen in Figure 22.

Figure 22 - Sample T2 Member Necking

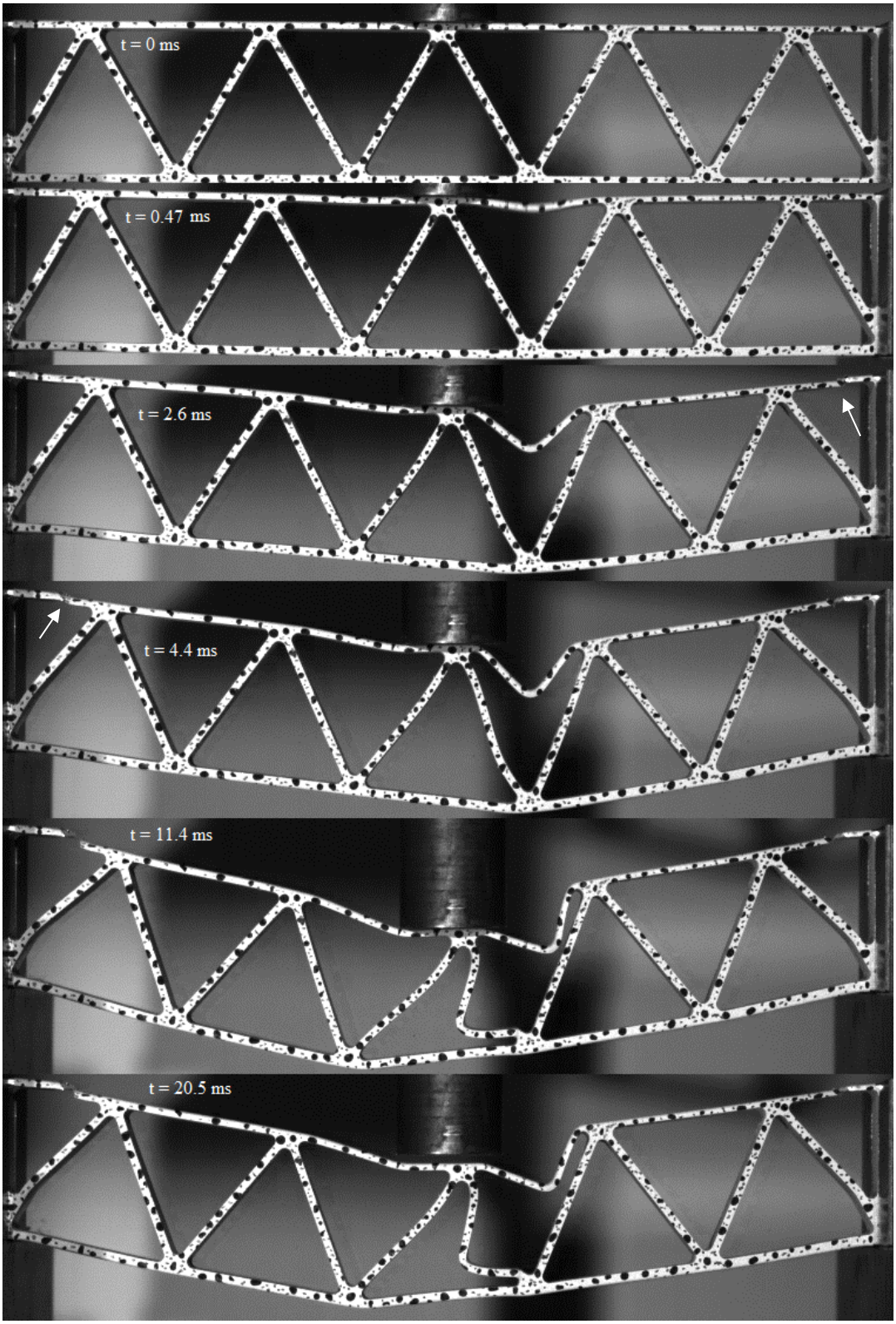

Figure 23- Experiment 2 Sample T1

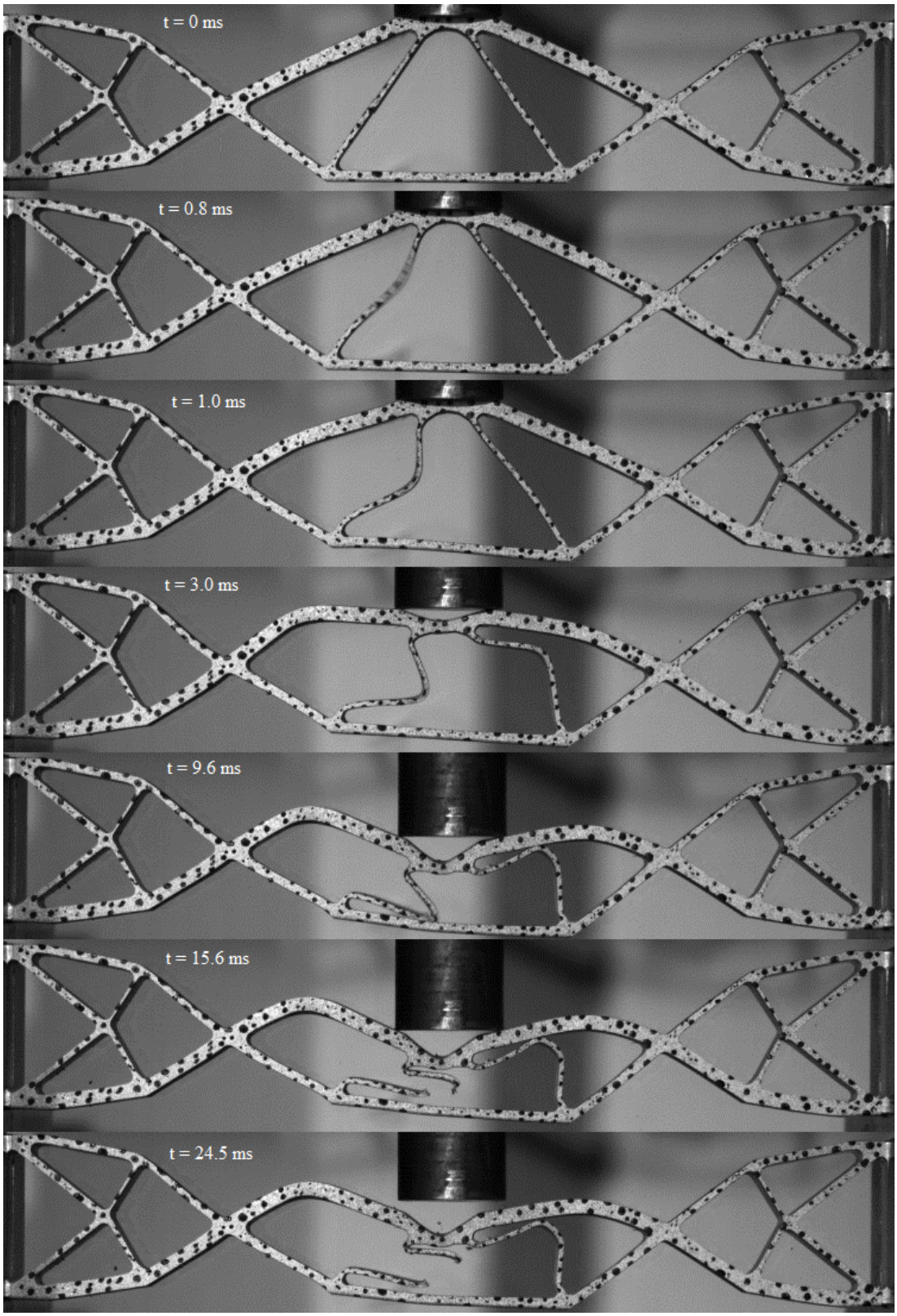

Figure 24- Experiment 3 P2

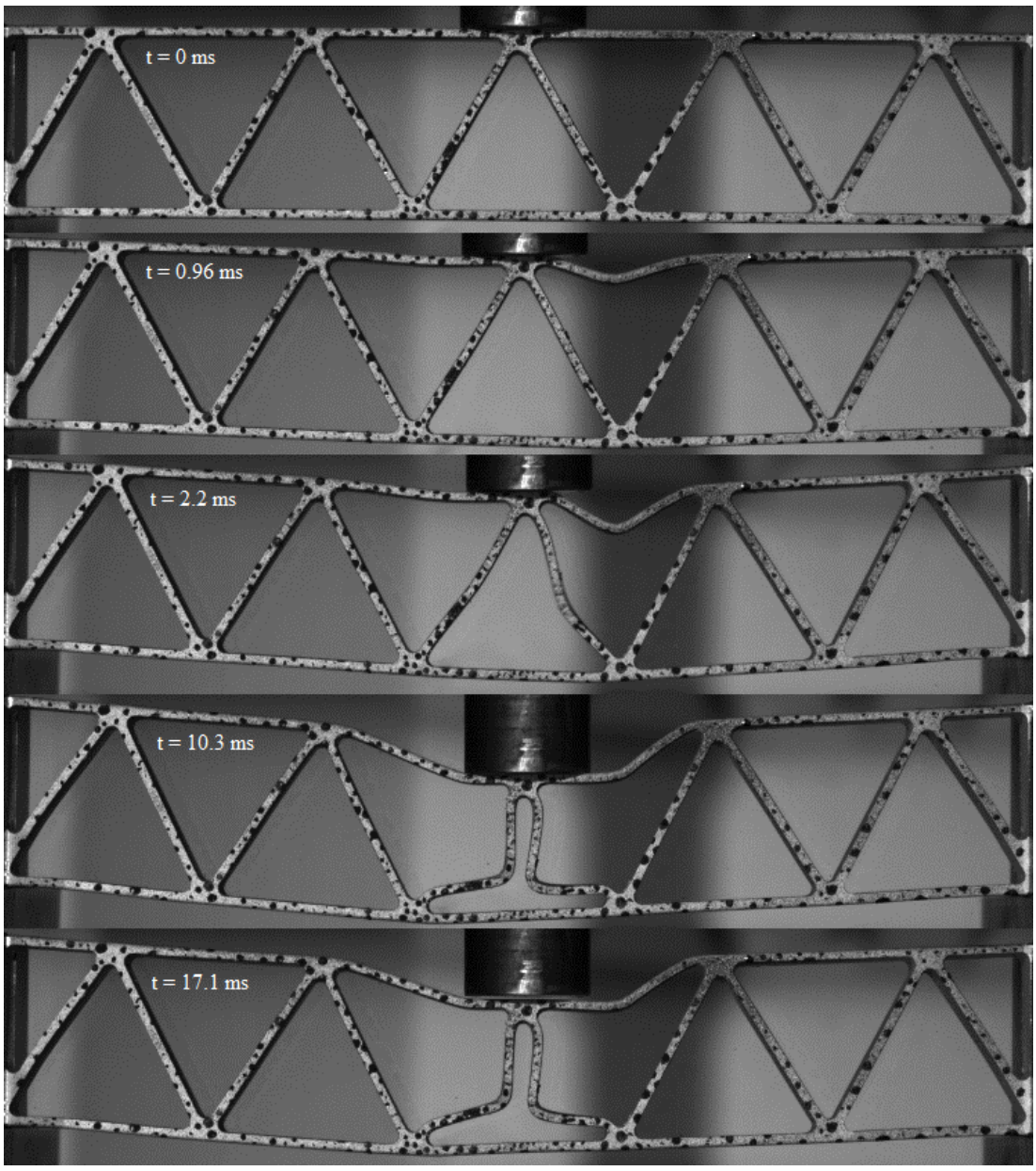

Figure 25- Experiment 4 Sample T2

Sample P3 withstood the lowest kinetic energy impact without any shear or tension failure. The structure may be able to hold considerable load even after the impact.

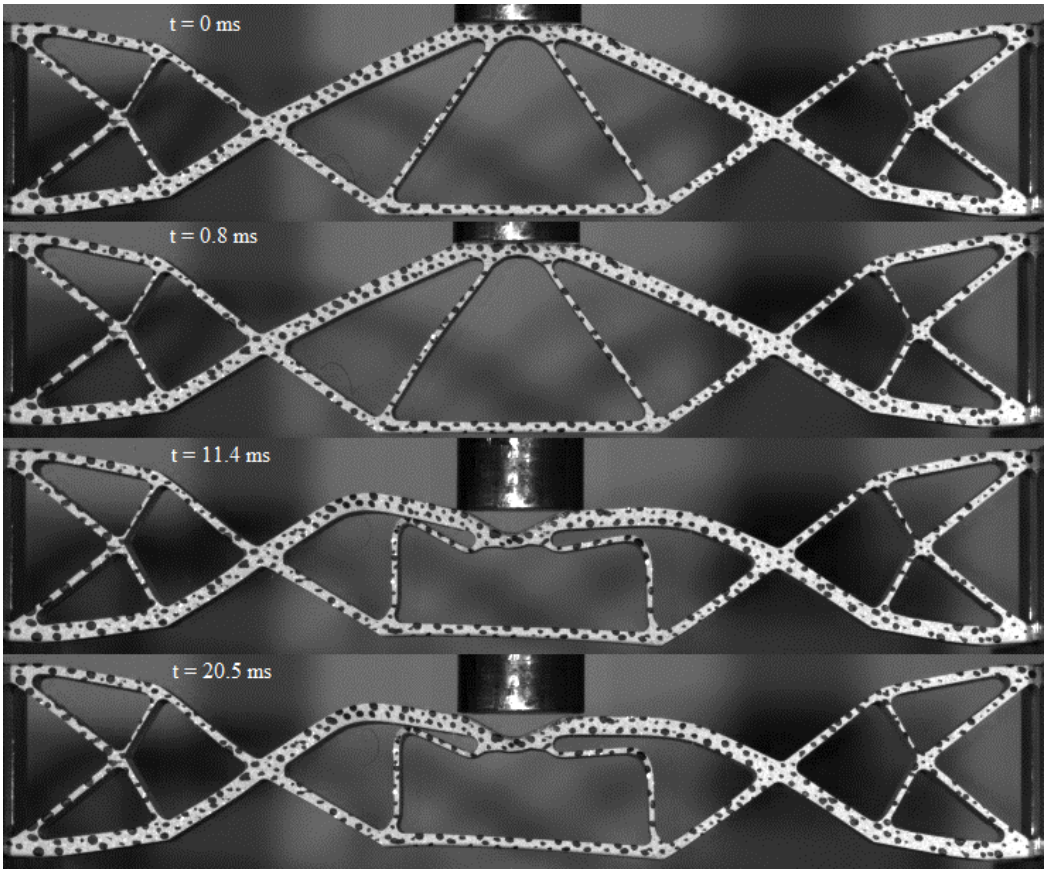

Figure 26- Experiment 5 Sample P3

Sample T4 showed the highest peak load of all the typical samples. This may be due to the fact that the sample deformed symmetrically for the first half of a millisecond. As shown in Figure 27, the top two members to the left and right of the tup buckle slightly in a mirror image. Then the right member begins to buckle

severely. This weakens the right side of the structure. As a result the top right member fails in tension as seen in Sample T1 and T2.

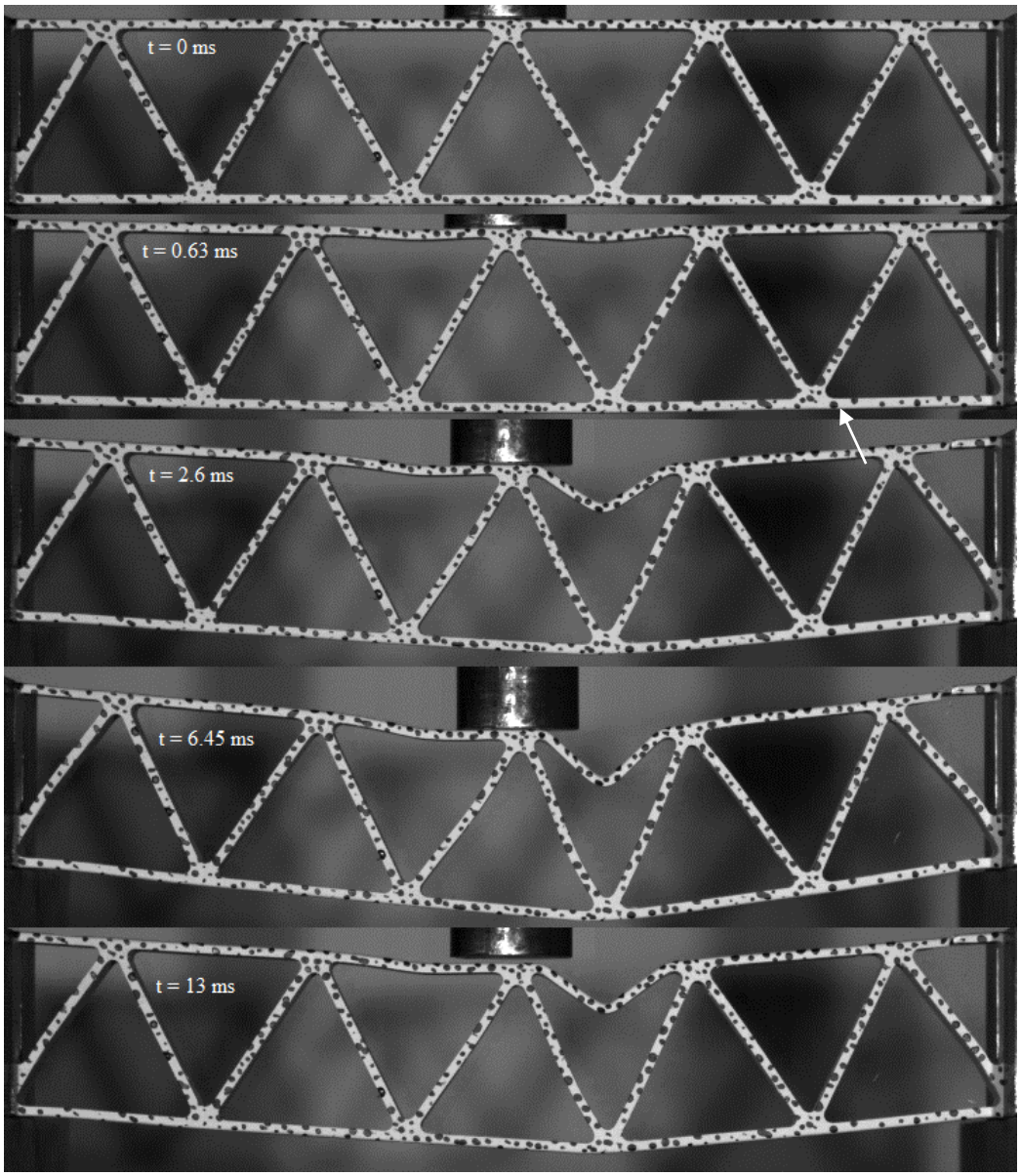

Figure 27- Experiment 6 Sample T3

3. FINITE ELEMENT ANALYSIS

The experimental results showed little out of plane deflections. Some minor necking of the material was evident when the specimens failed in tension but this effect is negligible. Hence, finite element simulations of the experiments assume two dimensional plane stress conditions. These analyses were performed using Abaqus 6-13. To reduce computation time, vertical symmetry conditions down the center of the part were imposed. Nodes on this plane are constrained from movement in the X direction. The assembly is composed of a rigid striker, the tup, the specific topology being evaluated, a fixture base and two shoulder bolts. Only two of these parts are meshed, the topology and the tup, the rest are analytical rigid parts. The fixture base and bolts are rigid and immovable. They interact with the topology by means of contact condition along their adjoining surfaces. The normal behavior is a "hard" contact. The tangential behavior uses a penalty friction formulation with a coefficient of friction of 0.61. The rigid striker is constrained to move only in the Y direction. The tup is the only part of the crosshead assembly that is meshed. It is constrained to move with the adjoining face of the rigid striker and an X symmetry condition is imposed. The contact conditions between the tup and the topology are the same as between the topology and the fixture. The rigid striker is used to model the rest of the crosshead. It has a reference point where the mass of the crosshead is applied to this singular point. This point mass is the total mass of the crosshead minus the mass of the meshed tup. In the experiments, crosshead assembly was equipped with a load cell. This load cell provided the acceleration of the crosshead. The acceleration is then multiplied by the mass of the crosshead to give the loads as shown in Figure 16.

To get similar data from the finite element analysis one could sum all the reaction forces between the tup and topology for every time increment. This is impractical since there are thousands of time increments. To get around this problem, the acceleration of the rigid striker is compared to the load cell data. The contact forces between the tup and the topology travel up the tup as a pressure wave. When the wave reaches the rigid striker they are summed by the program and act as one force on the rigid striker. Unlike the tup, the rigid striker has one node. The displacement, acceleration and velocity of this node are recorded at every time increment. The forces acting on the rigid striker can be obtained by multiplying the numerical acceleration results of the striker by the mass of the striker. These results are compared with the experimental load cell measurements.

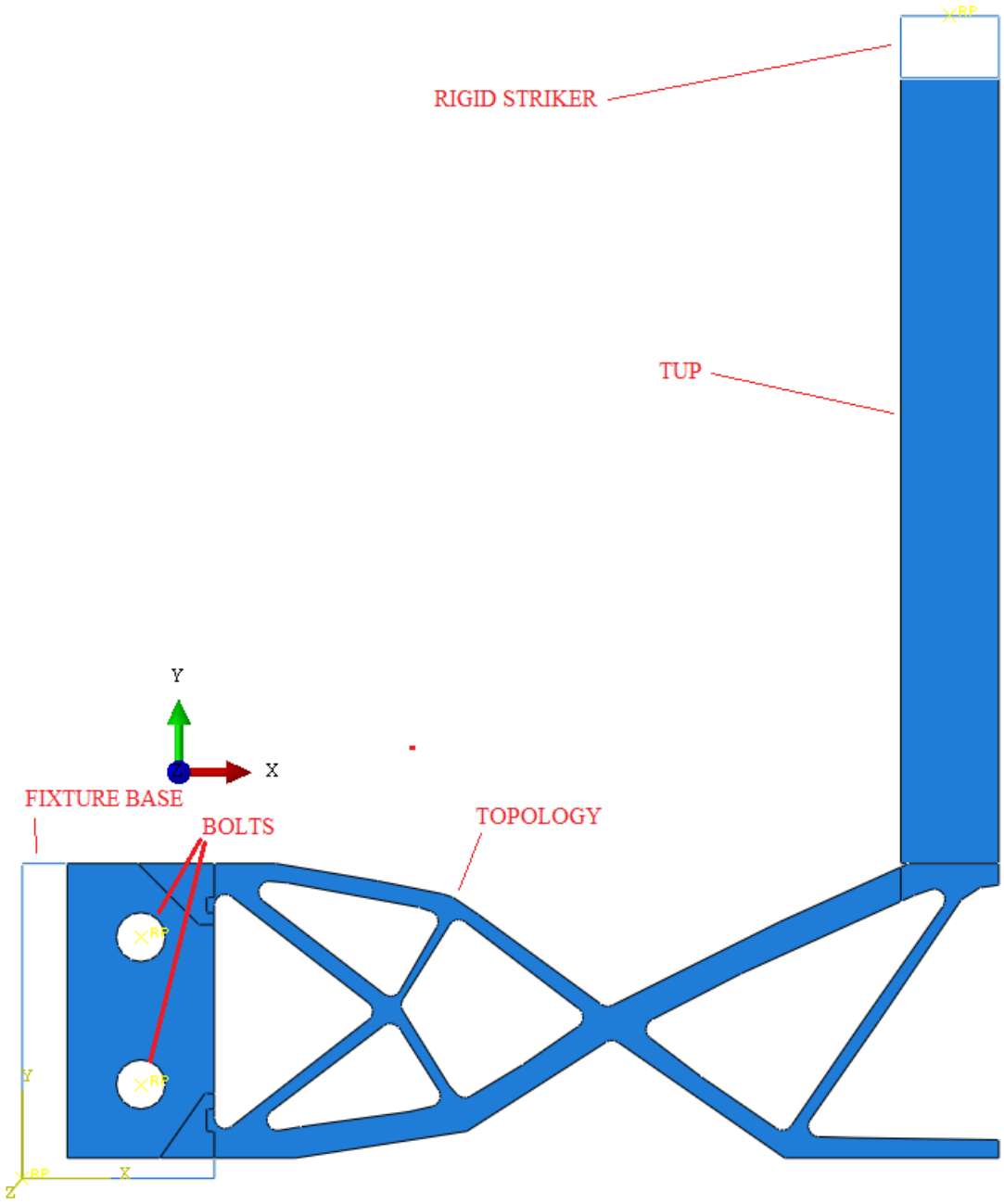

Figure 28- FEA Assembly

Buckling, static stress, dynamic impact and post impact static stress analyses are conducted on the eighteen topologies shown in Figure 29. Each PMR profile (Figures 28 a-i) has a comparable traditional profile (Figures 28 j-r) with the same mass.

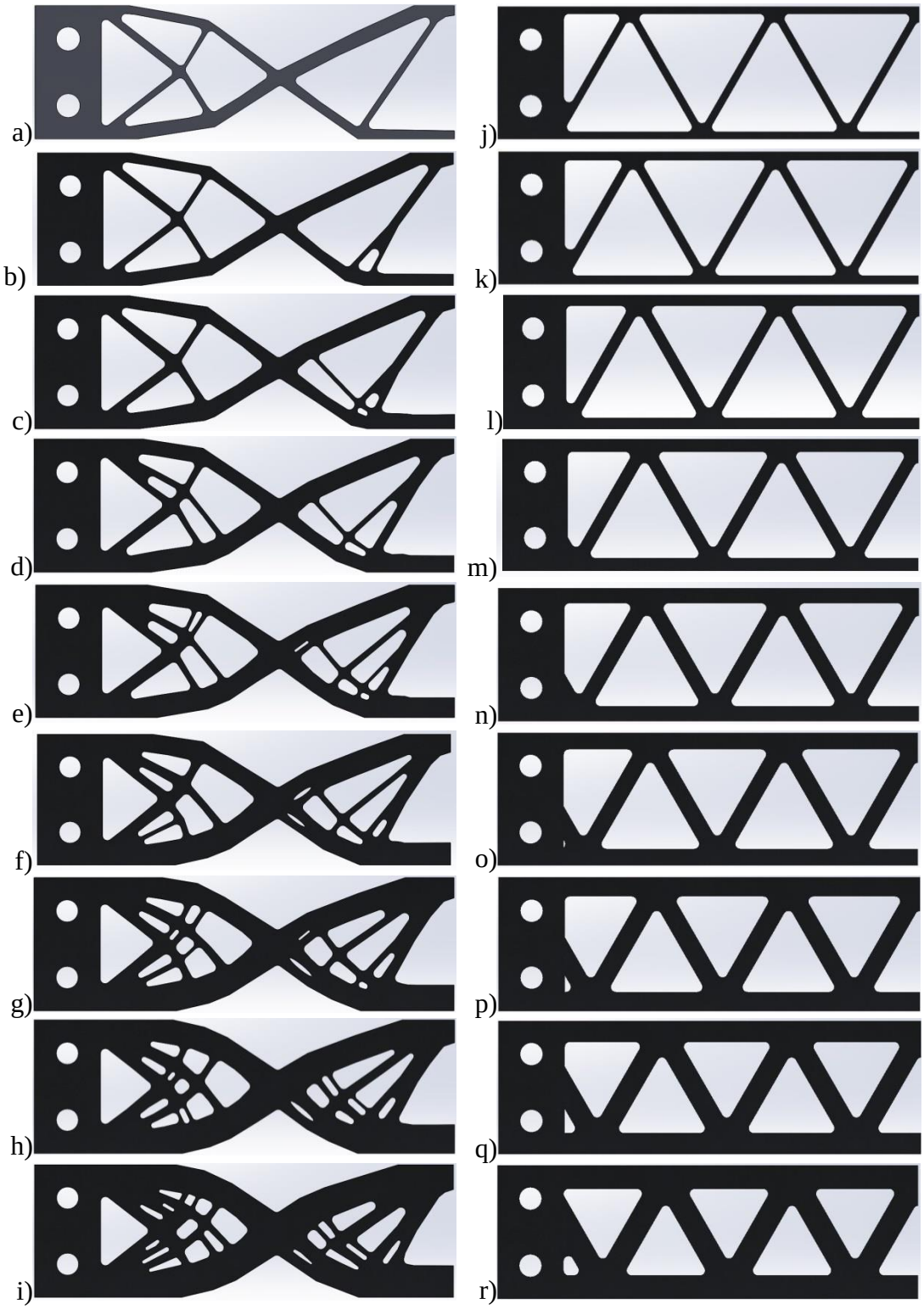

Figure 29 - FEA Topologies

The mass of each profile is shown in Table 6.

Table 6 - Profile Mass and Volume Fraction

PMR Profile	PMR Actual VF	PMR Mass [g]	TRI Profile	TRI Actual VF	TRI Mass [g]
PMR1	22.6%	30.00	TRI1	22.6%	30.00
PMR2	26.5%	35.17	TRI2	26.5%	35.17
PMR3	31.9%	42.28	TRI3	31.9%	42.28
PMR4	37.1%	49.27	TRI4	37.1%	49.27
PMR5	42.6%	56.54	TRI5	42.6%	56.54
PMR6	47.1%	62.51	TRI6	47.1%	62.51
PMR7	52.5%	69.65	TRI7	52.5%	69.65
PMR8	57.6%	76.48	TRI8	57.6%	76.48
PMR9	63.3%	83.99	TRI9	63.3%	83.99

3.1 MATERIAL MODEL

Aluminum 6061-T651 is a common material in manufacturing and the mechanical properties have been extensively studied. Material testing was not required. The data is collected from literature (See Table 7) (ASM Aerospace Specification Metals Inc. n.d.).

Table 7- Elastic Material Properties

	Young's Modulus [MPa]	Poisson's Ratio	Density [tonne/mm^3]	K_{Ic} [MPa-m$^{1/2}$]
AL 6061-T651	69000	.33	2.69E-9	29
Steel AISI 4340	205000	.29	7.85E-9	

The Johnson-Cook constitutive model is used to simulate the plasticity of the sample material. The flow stress is represented by Eq. 5 (Johnson G. 1985).

$$\sigma = [A + B\varepsilon^n]\left[1 + Cln\frac{\dot{\varepsilon}_{pl}}{\dot{\varepsilon}_0}\right]\left[1 - \left(\frac{T - T_a}{T_m - T_a}\right)^m\right] \quad (5)$$

The JC constitutive law is the product of the three terms shown in square brackets. The first term models the stress strain curve. Parameter A is the elastic limit of the material. Parameters *B* and *n* describe the plastic behavior of the material and its hardening. The second term models the effect of strain rate on the material. The parameter, *C*, describes the influence of strain rate. $\dot{\varepsilon}_{pl}$ is the plastic strain rate and $\dot{\varepsilon}_0$ is the reference strain rate. The third term describes the effect of temperature on the stress strain curve. T is the material temperature. T_a is the ambient temperature at which the tests have been done and T_m is the melting temperature of the material. The parameter m is a material characteristic parameter. Our experiments were conducted at ambient temperature and the finite element model will not include temperature effects. Therefore, temperature effects will be neglected in this study. The JC model is easily implemented into commercial finite element codes and is the standard plasticity model in Abaqus 6.13. The parameters used for the Johnson-Cook plasticity model is shown in Table 8 (Lesuer D. 2001). The maximum strain rate observed during finite element analysis is on the order of 300 s-1. The stress-strain curve for the Johnson-Cook plasticity model for strain rates 1 and 300 s-1 is plotted in Figure 30.

Table 8 - AL 6061-T651 Johnson-Cook Plasticity Constants

A [MPa]	B [MPa]	n	C	m	$\dot{\varepsilon}_0$ [s-1]
324	114	.42	.002	1.34	1

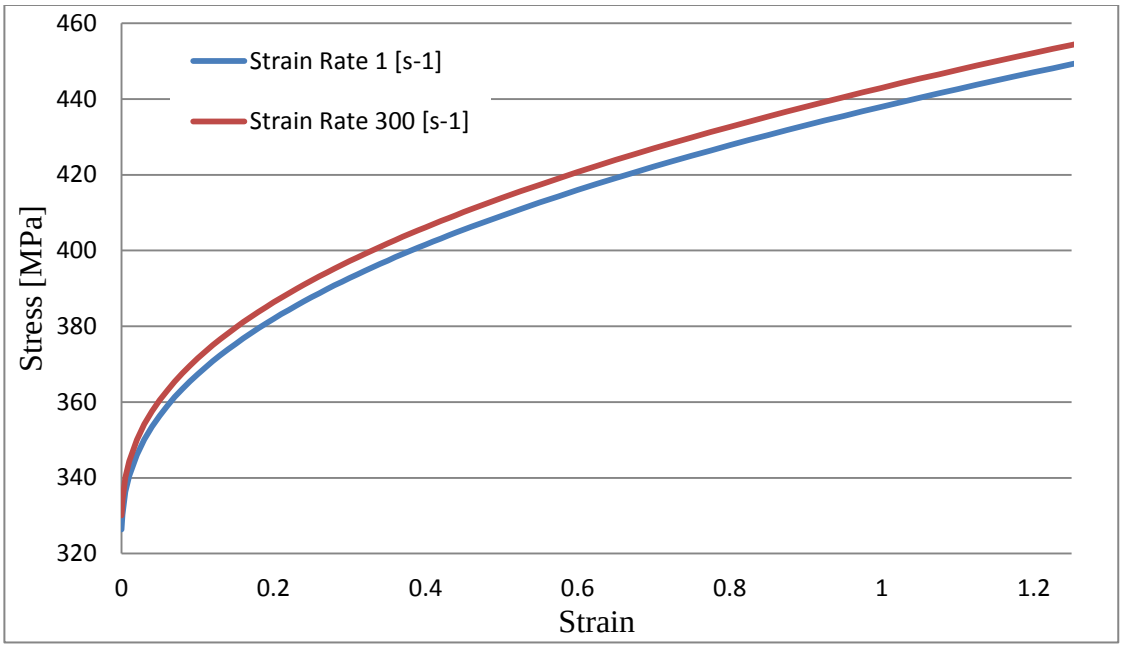

Figure 30 - JC Plasticity Model for AL6061-T651

In combination with the Johnson-Cook plasticity model a general expression for the strain at the initiation of damage is available as described by Eq. 6 (Johnson G. 1985).

$$\varepsilon_f = \left[D_1 + D_2 exp\left(D_3 \frac{\sigma_h}{\sigma_{VM}}\right)\right]\left[1 + D_4 ln\left(\frac{\dot{\varepsilon}_{pl}}{\dot{\varepsilon}_0}\right)\right]\left[1 + D_5 \frac{T - T_a}{T_m - T_a}\right] \quad (6)$$

Like the plasticity model, the expression for the strain at damage initiation is the product of three terms that describe the effect of stress triaxiality, strain rate and temperature effects, respectively. Stress triaxiality is defined as σ_h, the average of the three normal stresses or pressure, divided by σ_{VM}, the von Mises equivalent stress. The von Mises stress is defined in Eq. 7 (Budynas 2008). Where σ_1, σ_2, and σ_3 are the three principal stresses. The term defining strain rate dependence is very similar to the term in the plasticity model. Again, $\dot{\varepsilon}_{pl}$ is the plastic strain rate and $\dot{\varepsilon}_0$ is the

reference strain rate. The parameters used for the Johnson-Cook fracture model are listed in Table 9 (Lesuer D. 2001).

$$\sigma_{VM} = \sqrt{\frac{(\sigma_1 - \sigma_2)^2 + (\sigma_2 - \sigma_3)^2 + (\sigma_1 - \sigma_3)^2}{2}} \tag{7}$$

T_m and T_a are the melting temperature of the material and ambient temperature of the testing.

Table 9 - AL6061-T651 Johnson-Cook Fracture Parameters

D_1	D_2	D_3	D_4	D_5	T_m [°K]	T_o [°K]	$\dot{\varepsilon}_0$ [s^{-1}]
-0.77	1.45	0.47	0	1.6	925	293.2	1

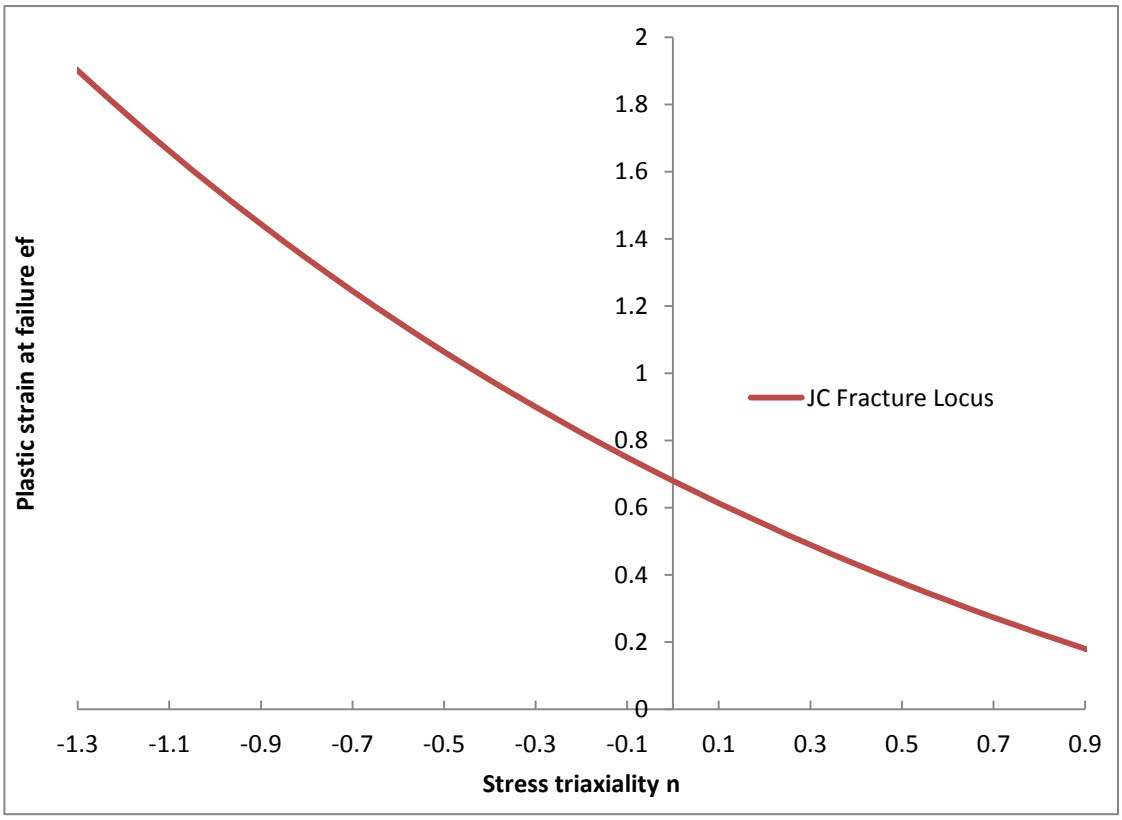

Figure 31 - Johnson-Cook Fracture Locus for Aluminum 6061-T651

Once damage initiation has occurred, the material begins to lose the ability to carry load until it reaches strain at failure, at which point the element is removed from the mesh.

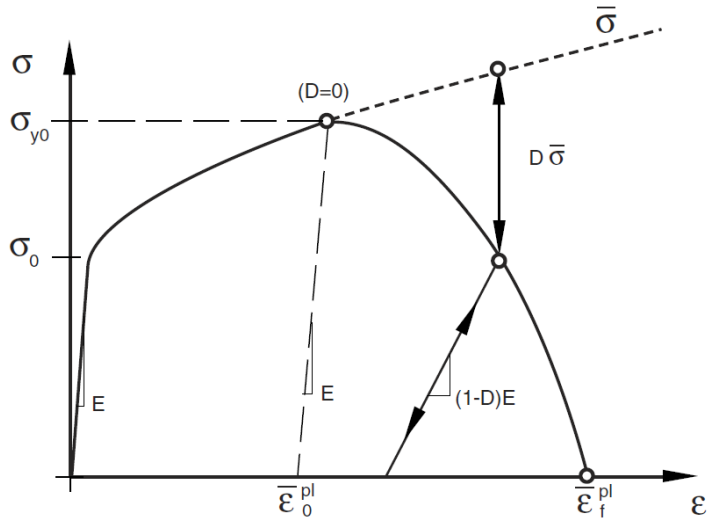

Figure 32- Stress-strain curve with progressive damage degradation (Simulia 2013)

The damage evolution law is specified in terms of fracture energy dissipation, G_f. The value for fracture dissipation can be derived from fracture toughness and Young's modulus using Eq. (8) (Shukla 2005).

$$G = {K_{Ic}}^2/E \tag{8}$$

Evaluating equation 8 for Aluminum 6061-T651 using the properties listed in Table 7 gives fracture dissipation energy of 12.2 Joules per millimeter.

3.2 MESH

A mesh sensitivity study was conducted to determine the best element size for the dynamic and static analyses. In general, the finer the mesh becomes the closer the

results approach the exact solution. Reducing the size of the elements increased computation time for each iteration and increases the number of iterations that must be performed. In dynamic analyses the increment time is governed by the smallest stable time increment. This is computed automatically by Abaqus. The explicit dynamics procedure in Abaqus, solves every problem as a wave propagation problem. The out of balance forces are propagated as stress waves between neighboring elements. The dilatational wave speed, C_d, for a linear elastic material is defined by equation 9 (Shukla 2005). Where E is the elastic modulus of the material and ρ is the density of the material.

$$C_d = \sqrt{\frac{E}{\rho}} \tag{9}$$

The stable time increment of an element is expressed in equation 10. Where Δt is the stable time increment of an element, L_e is the element length and C_d is the wave speed of the material. Abaqus determines the time increment for the analysis by finding the smallest element length in the whole model and using it to find the stable time increment for the analysis.

$$\Delta t = \frac{L_e}{C_d} \tag{10}$$

The aluminum used in our study has a waves speed of 5,064 meters per second. The average elements size is 0.3 millimeters. The time it would take for the dilatational wave to travel across the average element is 5.9E-8 seconds. This is the stable increment time for the average element. The longest analysis time from beginning to end is 0.03 seconds. Using the above increment time the longest analysis

would require five hundred thousand increments. Abaqus calculate the smallest stable increment time for each mesh generated. For the analyses performed in this study the smallest stable increment times were between 5E-9 and 2E-8 seconds.

Two types of elements were used all the analyses. CPS4R is a 4 node bilinear plane stress quadrilateral with hourglass control. SPS3 is a 3 node linear plane stress triangle. Each used second-order accuracy and element deletion. A single mesh is used for both the static and the dynamic analyses. The static mesh sensitivity study (see Figure 33) converges quickly to a solution. The mesh sensitivity study consisted of five static analyses on the PMR1 profile subjected to a 10 kN load. Each analysis used a different mesh starting with Mesh 1, the coarsest and ending with Mesh 5, the finest mesh. Since Mesh 5 is the finest mesh, it is assumed to be the most accurate. The midpoint deflection of for each analysis is recorded (See Table 10). The percent errors for meshes 1 through 5 are based on Mesh 5's deflection. The dynamic study was more difficult to evaluate. The first 3 milliseconds of experiment 1 is performed with four different average mesh sizes, 0.4mm, 0.3mm, 0.25 mm and 0.15mm (See Figure 34). The data from the experiment was much smoother than the data from the finite element analysis.

Table 10 - Static Mesh Sensitivity

	Mesh 1	Mesh 2	Mesh 3	Mesh 4	Mesh 5
Global Element Size (G) [mm]	0.5	0.4	0.3	0.2	0.1
Number of Elements	8,162	12,721	22,888	52,377	218,022
Deflection [mm]	0.54570	0.54600	0.54600	0.54700	0.54700
Percent Error from Mesh 5	0.238%	0.183%	0.183%	0.000%	0.000%

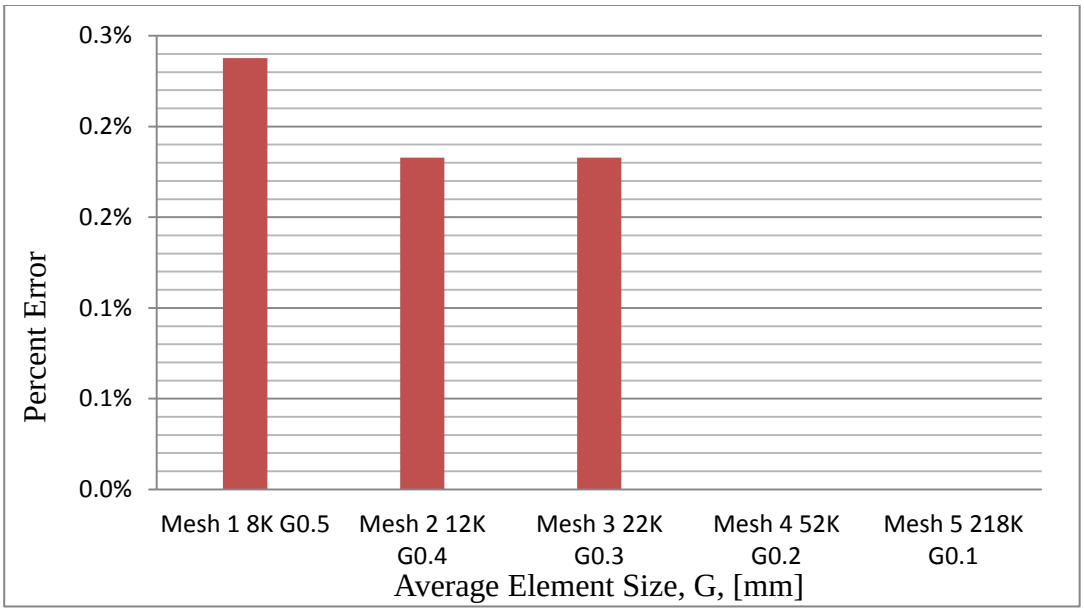

Figure 33- Static Mesh Size vs Percent Error from Mesh 5

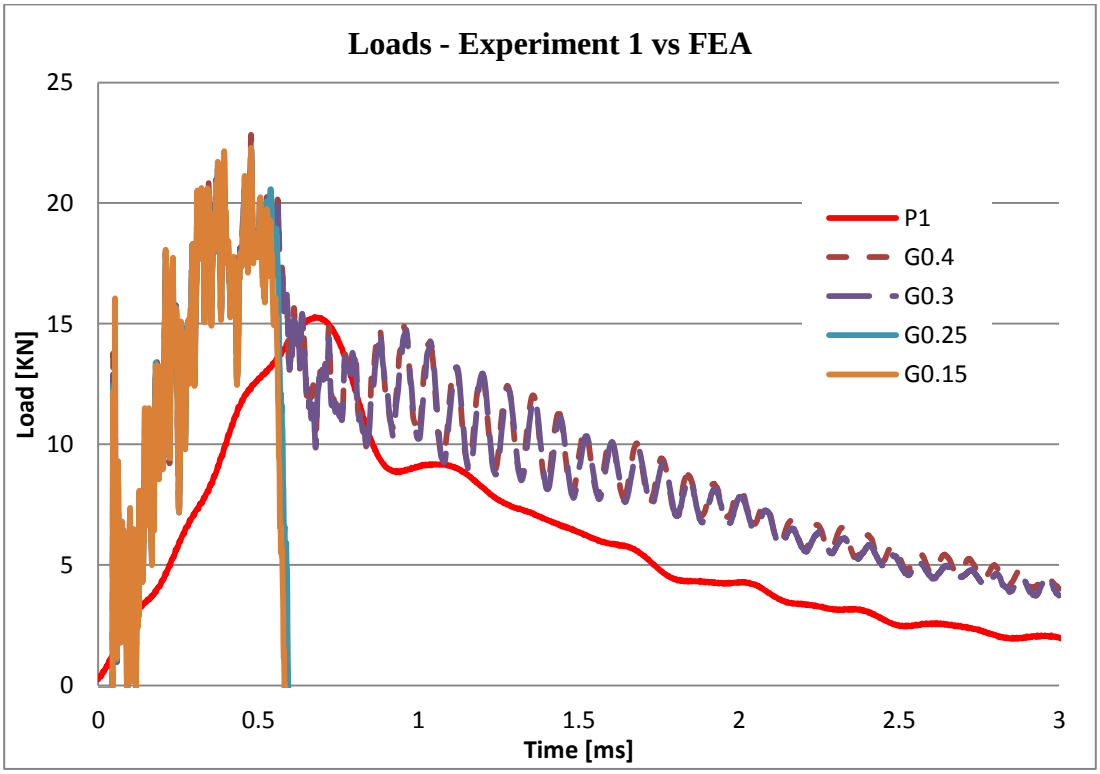

Figure 34 - Dynamic Mesh Sensitivity

The finer mesh sizes (0.25mm and 0.15mm) showed unrealistic data after 0.5 milliseconds. The best choice of mesh size is clearly a seed size of 0.3 millimeter. This seed size was used for the internal structure of the topology and creates a very fine mesh Figure 35. A closer look at the mesh shows that it is dominated by four sided elements with some three sided elements Figure 36. The clamping area used a coarser seed size of 1 millimeter to save computational time during dynamic analysis.

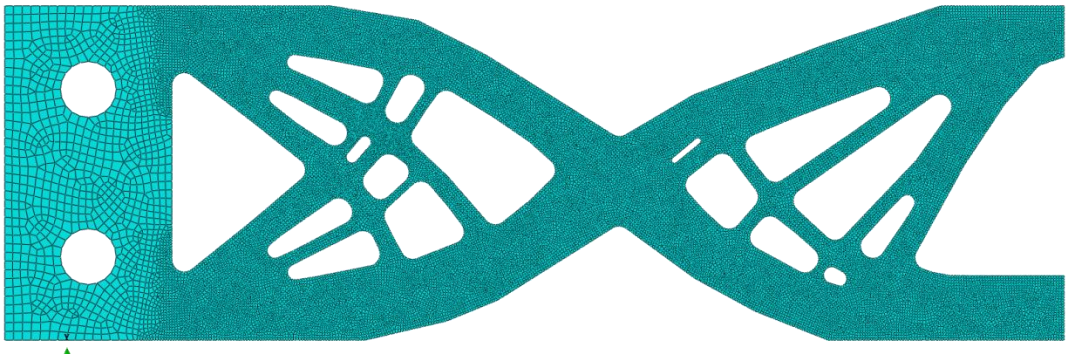

Figure 35 - Mesh PMR7

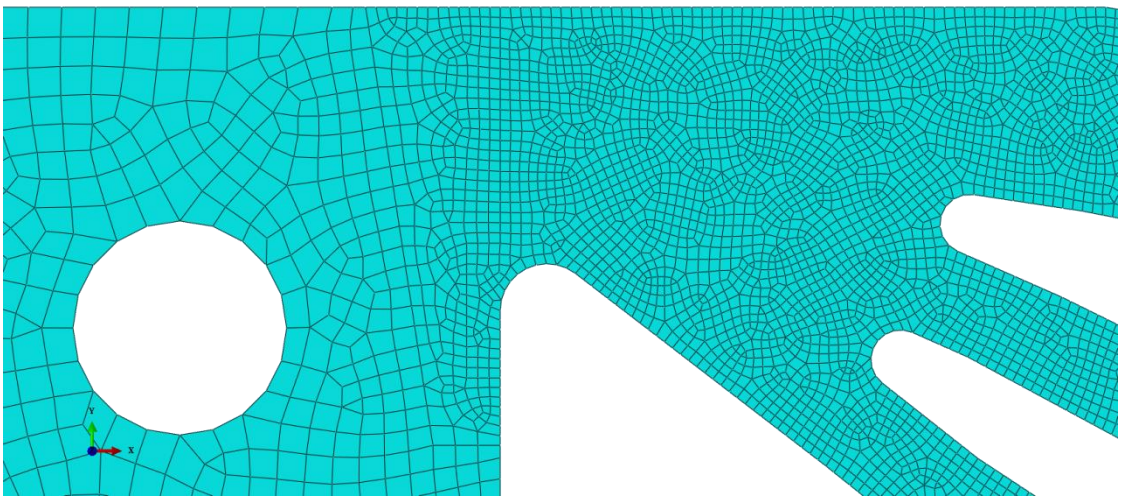

Figure 36 - Mesh Detail PMR7

3.3 STATIC ANALYSIS

Each topology was partitioned into five areas. The design area of the topology is one section. A load area 12.7 mm in length is created at the top right corner of the design area. Outside the design area the clamping area is partitioned into three sections. The largest with be a coarse mesh section and the two smaller section will be used to transition from the fine mesh of the design area to the coarse mesh of the clamping area. For the static analyses the entire clamping area will be fixed and no nodes in this area will be allowed to move. A symmetry condition is again applied to the right side of the domain. A general traction load is applied to loading area on the top right of design domain as shown in Figure 37. The total force of this traction is 7 kN.

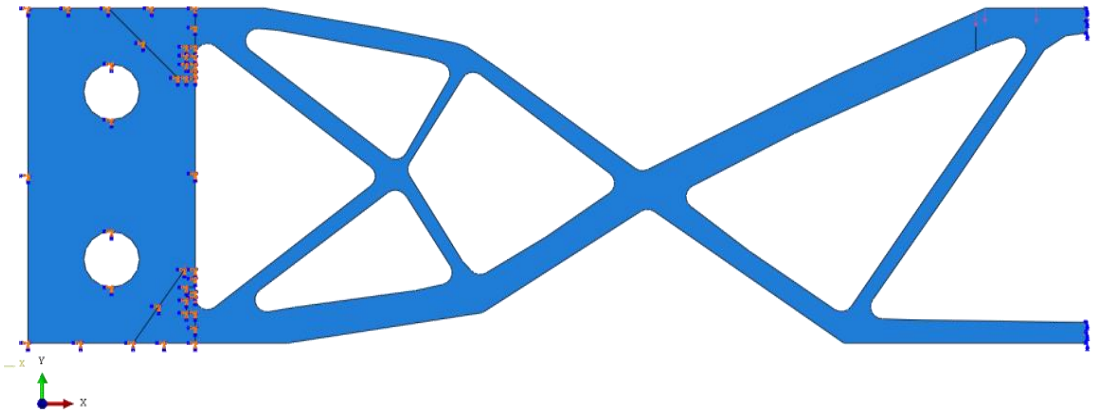

Figure 37- Static Boundary & Load Conditions

The strain energy density of PMR3 and TRI3 is shown in Figure 38 and Figure 39 respectively. The maximum strain energy density for PMR3 is 0.9 and for TRI3 it is 0.97. It is not surprising that it is slightly higher. The most interesting difference is the pattern of the strain energy densities. PMR3 has the load quite evenly throughout the structure with higher levels at member intersections. In contrast, TRI3 has two full

members with an almost zero strain energy density throughout. The four corners of the domain in both structures show elevated stress levels but this cannot be avoided since no more material can be added to these areas.

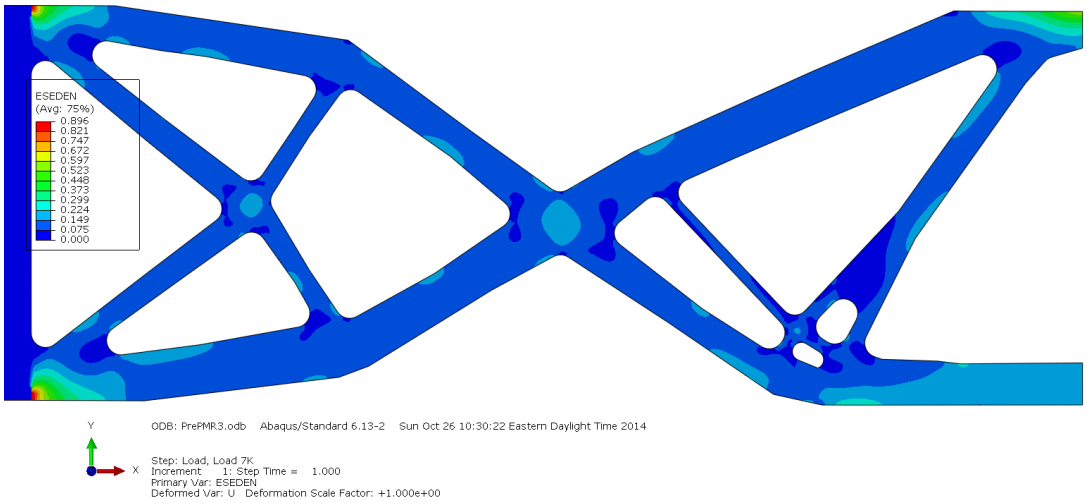

Figure 38- PMR3 Static 7kN Load Stain Energy Density

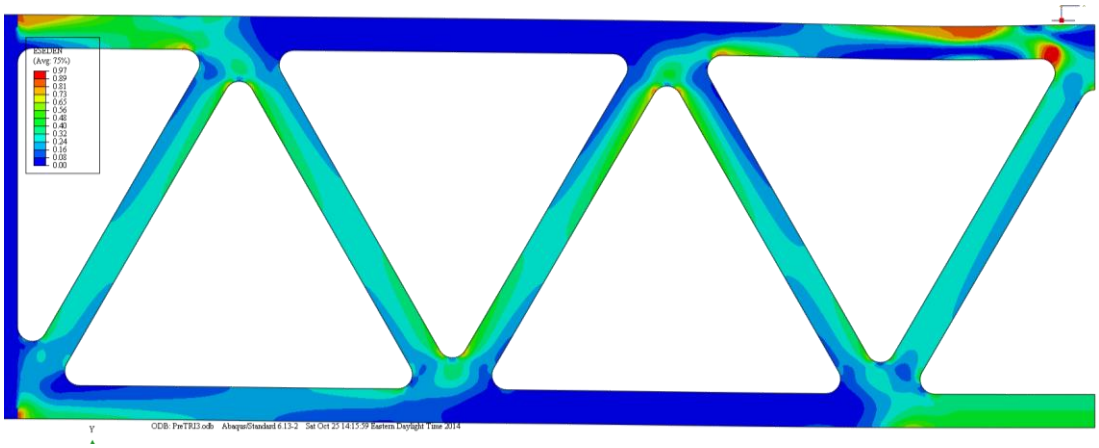

Figure 39 – TRI3 Static 7kN Load Strain Energy Density

This pattern repeats it's self for the rest of the pairs of topologies. The PMR consistently distributes the strain energy better than the typical equilateral triangle structure. The PMR profiles performed better under static loading. The deflection,

U2, of the top mid-point was consistently better than the typical profiles (See Figure 40). The top mid-point is located in the top right corner of the domain along the axis of symmetry. Profiles TRI1 and TRI2 could not hold the 7 kN load and failure to converge to a solution. The load was reduced to 5 kN for these two profiles and their deflections are still more than their paired PMR profiles under 7 kN. The structural stiffness of the profiles was obtained by dividing the applied load by the deflection of the top midpoint of the structure as shown in Figure 41. It is clear that the PMR series is stiffer than the traditional series.

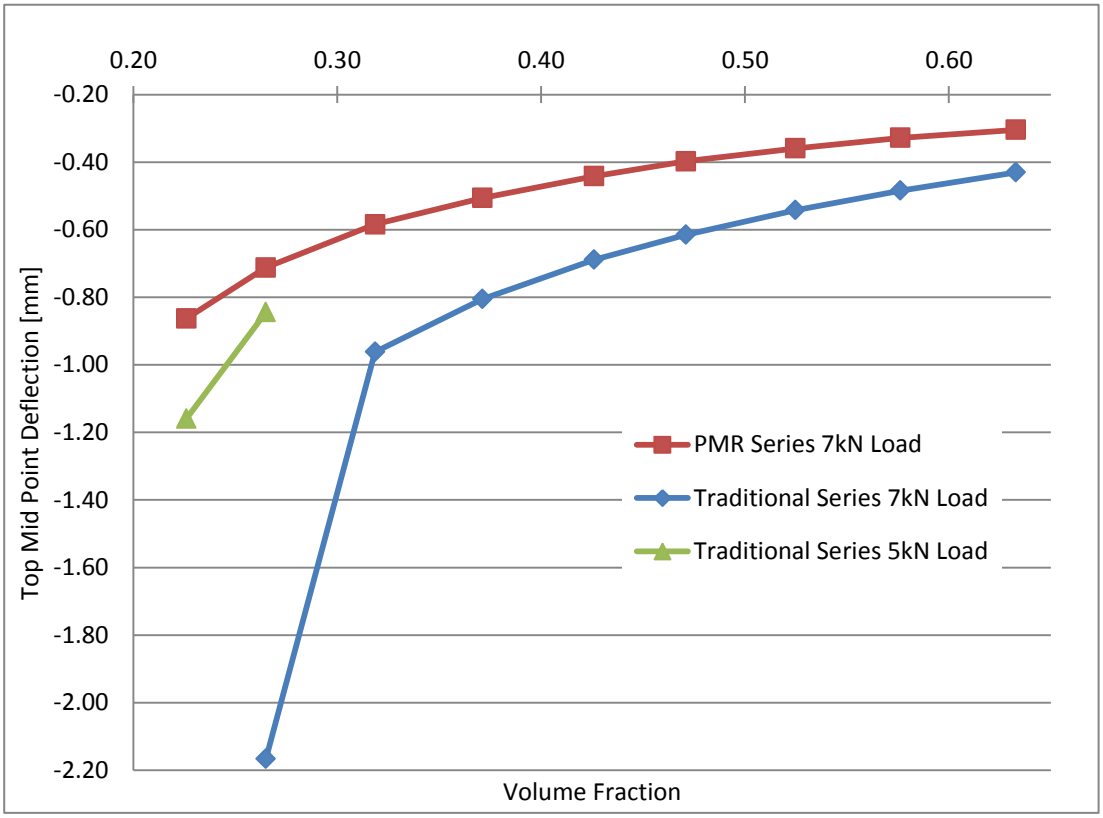

Figure 40 - Static Deflection of Profiles

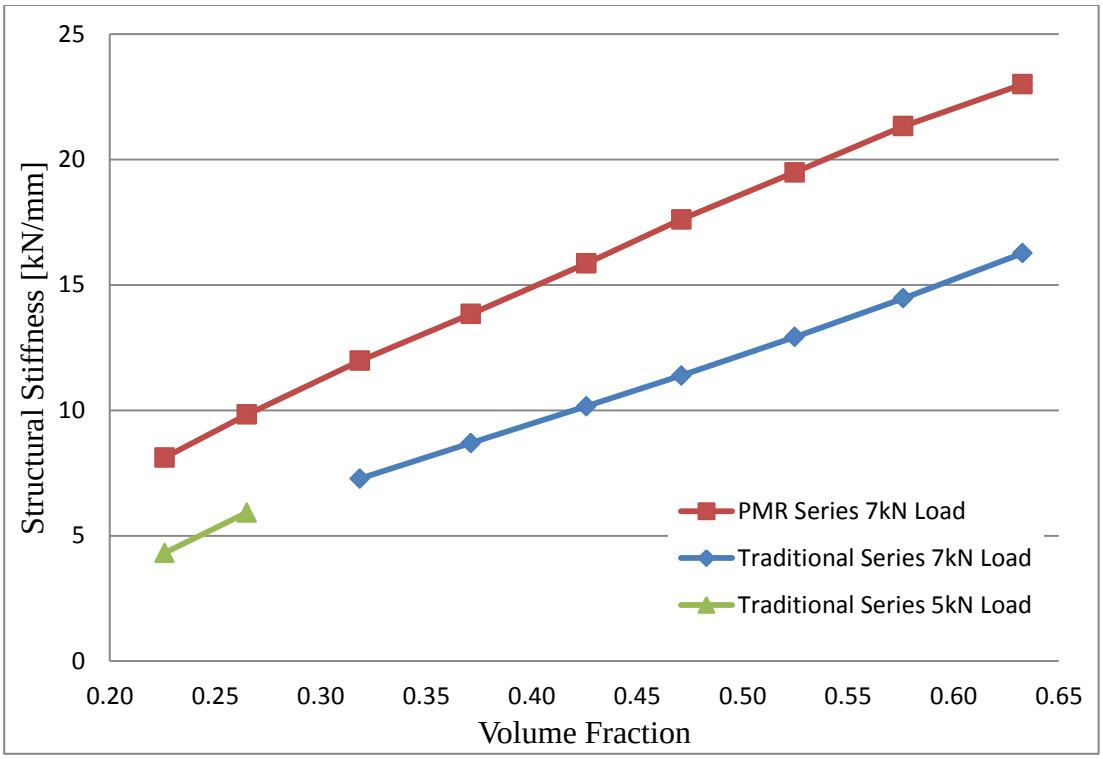

Figure 41 - Static Structural Stiffness

3.4 BUCKLING ANALYSIS

The first six Eigenvalues for all eighteen profiles are obtained by a linear perturbation step. The tup part was removed from this analysis. The rigid striker provided a load of 1N to determine the eigenvalues of the profiles (See Table 11 and Table 12)

Table 11 - Eigenvalues for Typical Profiles

Profile	Volume Fraction	Mode 1	Mode 2	Mode 3	Mode 4	Mode 5	Mode 6
TRI1	0.23	-11204	15198	-17019	-18291	18989	21502
TRI2	0.26	-18536	25287	-28197	-30597	31872	35720
TRI3	0.32	-35924	49675	-54853	-60564	63353	65586
TRI4	0.37	-62336	87216	-95839	106658	-107614	113312
TRI5	0.43	-102890	145239	-159614	174638	-182283	191630
TRI6	0.47	-149033	211534	-233934	250873	-270084	277584
TRI7	0.52	-224574	317764	-357807	368269	384243	405813
TRI8	0.58	-322892	404205	447875	479886	504604	517932
TRI9	0.63	399700	-469189	473986	513556	523120	625103

Table 12 - Eigenvalues PMR Profiles

Profile	Volume Fraction	Mode 1	Mode 2	Mode 3	Mode 4	Mode 5	Mode 6
PMR1	0.23	-14379	17991	35901	-50951	-52852	54184
PMR2	0.26	-37408	64863	70652	-74701	80849	-82875
PMR3	0.32	-71263	-77586	135204	-142975	-142975	-149650
PMR4	0.37	104631	-106490	-116694	125880	-135046	-180828
PMR5	0.43	108175	-155158	199828	-201062	-276736	-297546
PMR6	0.47	106267	197829	206387	-288109	344948	-378609
PMR7	0.52	249437	357600	365730	414088	-430997	482591
PMR8	0.58	346135	388018	536211	571590	-580660	673075
PMR9	0.63	395706	479127	485489	682750	736729	742059

The first positive eigenvalue is of most concern. This can predict at what load the structure starts to buckle. These values are plotted in Figure 42. Starting with the lowest volume fraction the PMR profile has a higher eigenvalue for the first four profile pairs. A higher eigenvalue indicates that it will buckle at a higher load.

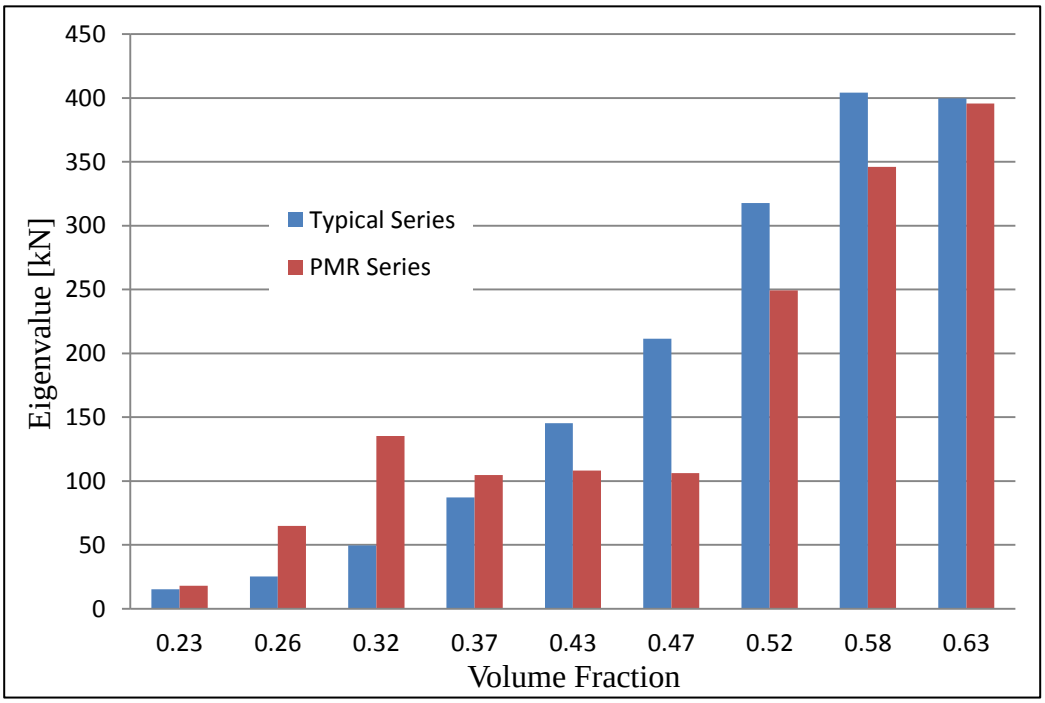

Figure 42 - First Positive Eigenvalues

The mode 2 eigenvalue for PMR1 shows the thin internal member below the point of impact deflecting inward (See Figure 43). The mode 2 eigenvalue for TRI1 shows a member in the center of structure buckling (See Figure 44).

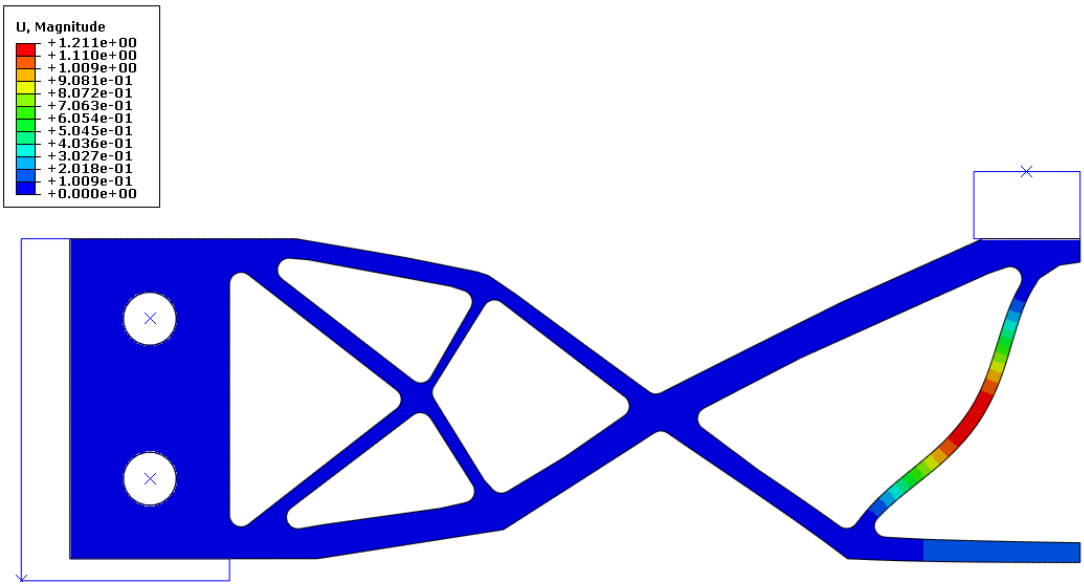

Figure 43 - PMR1 Mode 2

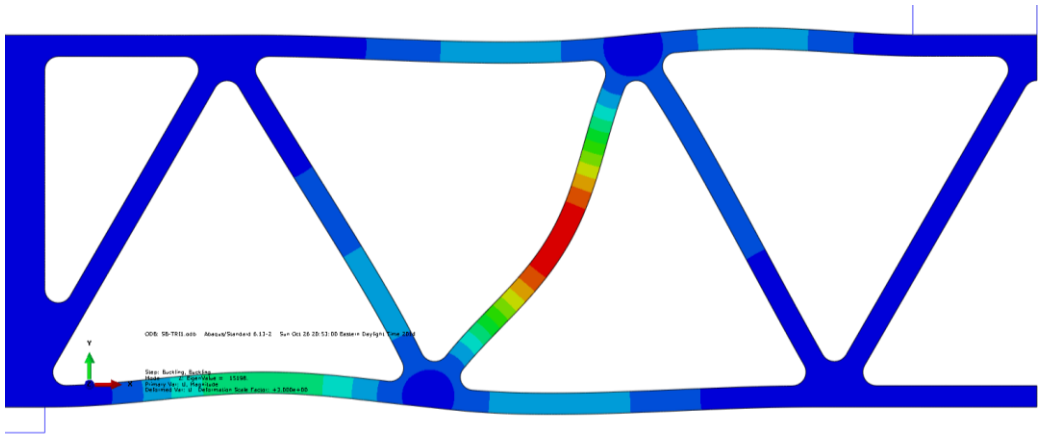

Figure 44 - TRI1 Mode 2

3.5 DYNAMIC ANALYSIS

The dynamic analysis is conducted using Abaqus Explicit. The initial velocity of the tup and rigid striker is set as a predefined field. The initial velocity of the tup and rigid striker combined with their masses provide the kinetic energy of the impact.

Six analyses emulate the conditions of the experiments performed in the laboratory. These are used to validate the FEA model. The impact energy density is defined as the kinetic energy at impact divided by the profile's design area mass. Profiles with a higher mass are hit with a higher kinetic energy. The mass of the tup and rigid striker remains constant while the initial velocity is increased to obtain the desired kinetic energy. An impact energy level of 1.06 Joules per gram is chosen for the remaining profiles PMR1 through PMR9 and TRI1 through TRI9 as shown in Table 13. This is the same energy level as Experiment 5 and 6. The Abaqus input file is for the dynamic analysis is given in APPENDIX 2.

Table 13 - Dynamic FEA Conditions

Profile	Volume Fraction	Design Area Mass [g]	Mass of Rigid Striker [kg]	Mass of Tup [kg]	Total Mass [kg]	Initial Velocity [mm/s]	Impact Kinetic Energy [J]	Impact Energy Density [J/g]
PMR1 & TRI1	0.23	29.9	8.5255	0.127	8.6525	3639	57.3	1.92
PMR1 & TRI1	0.23	29.9	6.0155	0.127	6.1425	3639	40.7	1.36
PMR1 & TRI1	0.23	29.9	6.0155	0.127	6.1425	3209	31.6	1.06
PMR2 & TRI2	0.26	35.0	6.0155	0.127	6.1425	3475	37.1	1.06
PMR3 & TRI3	0.32	42.1	6.0155	0.127	6.1425	3810	44.6	1.06
PMR4 & TRI4	0.37	49.1	6.0155	0.127	6.1425	4113	51.9	1.06
PMR5 & TRI5	0.43	56.3	6.0155	0.127	6.1425	4406	59.6	1.06
PMR6 & TRI6	0.47	62.3	6.0155	0.127	6.1425	4633	65.9	1.06
PMR7 & TRI7	0.52	69.4	6.0155	0.127	6.1425	4890	73.4	1.06
PMR8 & TRI8	0.58	76.2	6.0155	0.127	6.1425	5124	80.6	1.06
PMR9 & TRI9	0.63	83.7	6.0155	0.127	6.1425	5370	88.6	1.06

The maximum displacement of the top midpoint of the topology is recorded in each analysis. Every topology was impacted with an impact energy density of 1.06 Joules per gram. The maximum displacements, peak loads and J Impulse are shown in Figure 45, Figure 46 and Figure 47 respectfully. Apart from the traditional series gross deflections for TRI1, TRI2 and TRI3, the maximum deflections of the top midpoint ranged between 4.4 and 5.9 millimeters. The PMR series has a lower maximum deflection eight times out of nine, but this does not mean the PMR series performed necessary better as will be discuss later. The traditional series performed very consistently at higher volume fractions with a maximum displacement of 5.3 millimeters for the six highest volume fractions. The PMR series showed in a higher peak loads for most of the volume fractions. This is unsurprising given the stiffness of the PMR topologies. The total impulse applied to the striker can be determined by looking at the change in momentum of the striker itself. Impulse, J, is defined as the integral of force, F(t), overtime and this is equal to the change in momentum of the particle (Eq. 11) (Serway 1997). Since the striker mass remains constant and is denoted by m. The impact velocity is V_1 and the rebound velocity is V_2. The rebound velocity has an opposite sign to V_1. The mass and velocities of the striker are easily obtained from the analysis. The rebound velocity for the experiments was not obtainable.

$$J = \int_{t_i}^{t_f} F(t)\, dt = \Delta p = mV_1 - mV_2 \tag{11}$$

The failure mode of each analysis is shown in Table 14 along with the number of elements used and the CPU time to perform the analysis. It took over one hundred hours to perform all the analyses in this study.

The PMR series the traditional series showed similar J impulses except when the PMR topologies failed in tension. In these cases the PMR topologies fell below the traditional series. The impulses are similar even with the large difference in loading profiles because the traditional series has a lower load profile but for a longer time than the high load profile of the PMR series over a short time.

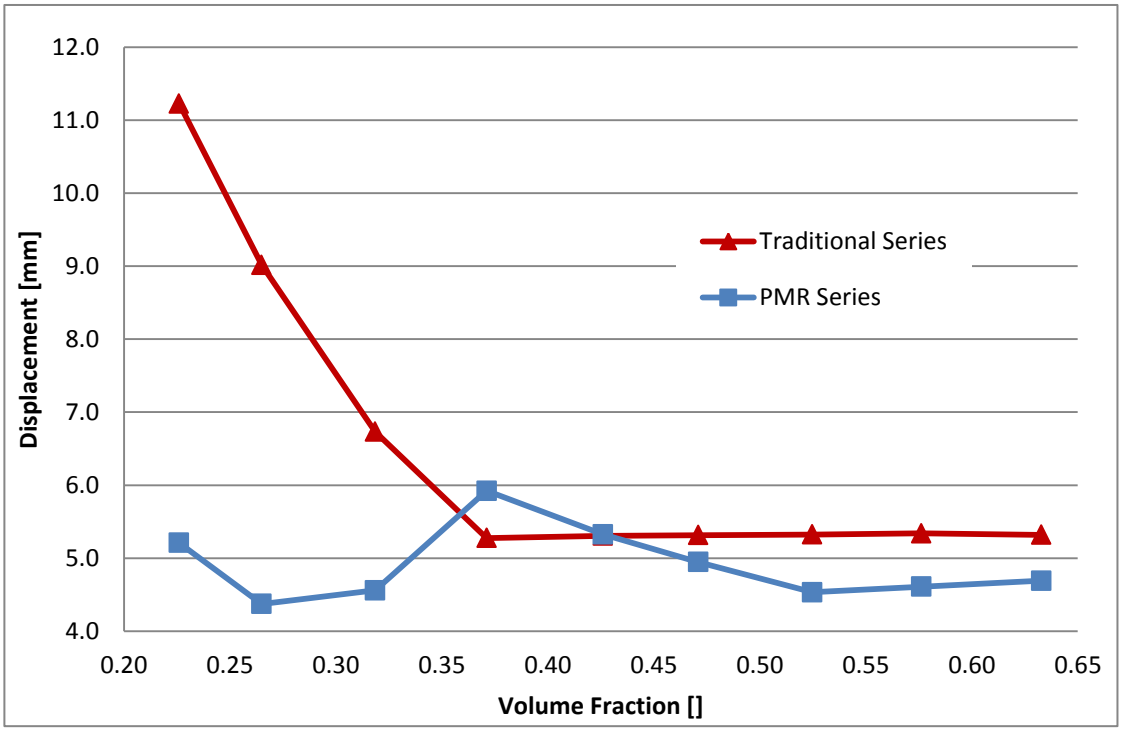

Figure 45 - Maximum Top Mid-Point Displacement

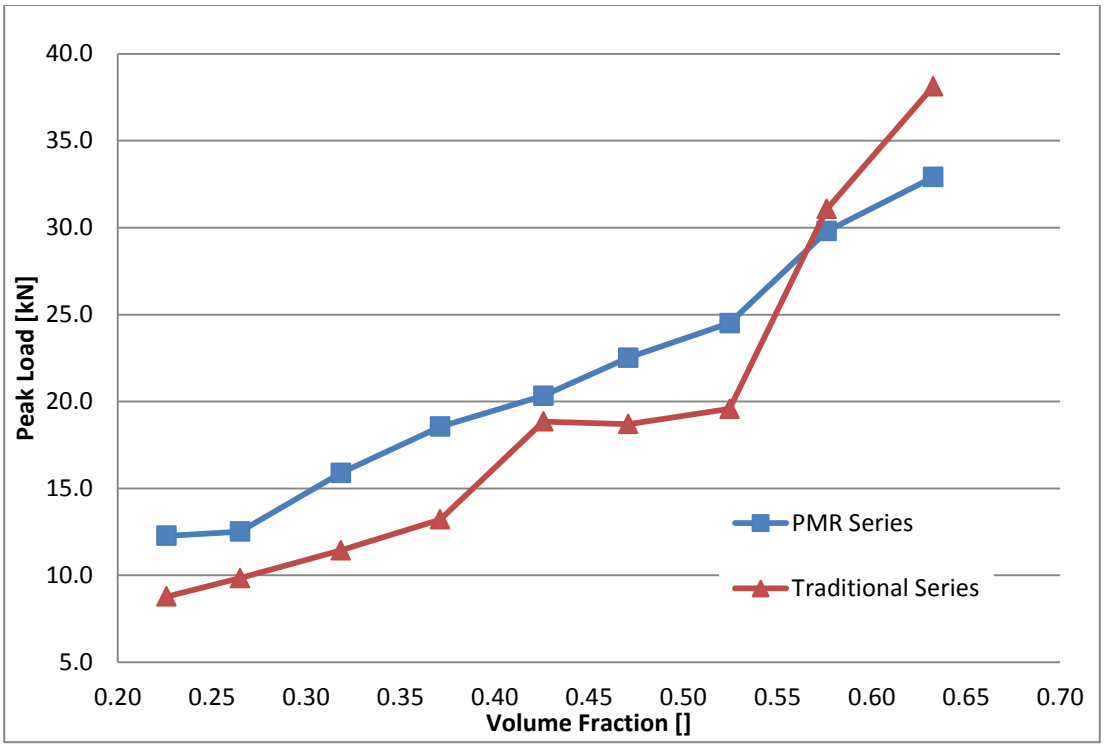

Figure 46 - Dynamic Analyses Peak Loads

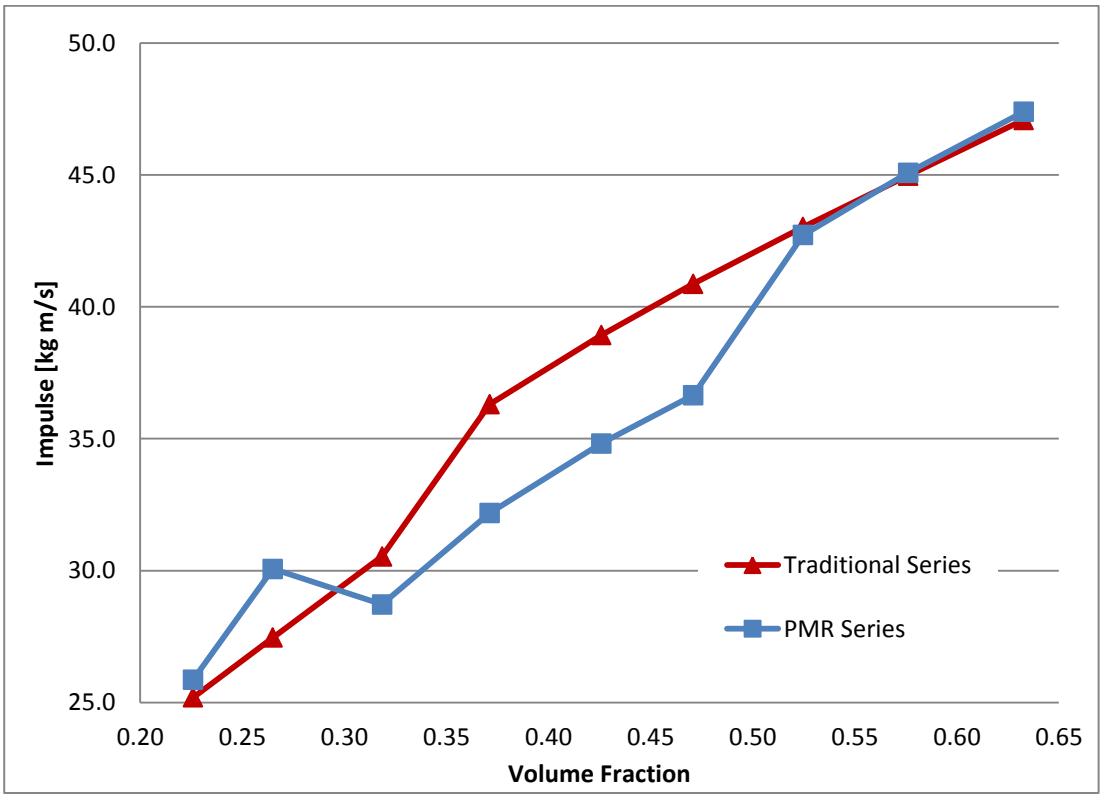

Figure 47 - J Impulse

Table 14- Dynamic Results

	PMR				Traditional			
Volume Fraction	Analysis	Number of Elements	CPU Time [hours]	Failure Mode	Analysis	Number of Elements	CPU Time [hours]	Failure Mode
0.23	PMR1-E1	15748	6.5	Buckling	TRI1-E2	15160	11.6	Tensile & Buckling
0.23	PMR1-E3	15748	6.5	Buckling	TRI1-E4	15160	11.5	Tensile & Buckling
0.23	PMR1-E5	15748	6.4	Buckling	TRI1-E6	15160	5.8	Tensile & Buckling
0.26	PMR2	17867	2.1	Buckling	TRI2	17528	2.9	Buckling
0.32	PMR3	20364	2.3	Tensile	TRI3	19931	3.2	Buckling
0.37	PMR4	23188	1.7	Tensile	TRI4	23087	2.6	Plastic
0.43	PMR5	26535	3.6	Tensile	TRI5	26651	3.7	Plastic
0.47	PMR6	29048	3.2	Tensile	TRI6	28210	3.0	Plastic
0.52	PMR7	32125	5.4	Plastic	TRI7	31418	3.3	Plastic
0.58	PMR8	34732	3.8	Plastic	TRI8	34161	3.8	Plastic
0.63	PMR9	38036	4.4	Plastic	TRI9	37464	2.7	Plastic

The complete series of plots of the von Mises stress for each profile shortly after impact and after the tup loses contact with the topology are given in APPENDIX 1.

4. VALIDATION OF FEA MODEL

The six experiments were reproduced using finite element analysis. Two metrics are used to evaluate the finite element model, maximum deflection of the top mid-point of the structure and the peak load (See Table 15). The analysis of the first experiment, PMR1-E1 recorded a maximum deflection much less than the experiment. The peak load was recorded from the FEA was around 83% recorded by the Instron. In contrast the analysis of experiment 2, TRI1-E2 failed to arrest the tup and rigid striker after 30 milliseconds. As a result its max deflection far exceeds that recorded in experiments.

Table 15 - FEA vs Experimental Data

Analysis	FEA Max Deflection Top Mid [mm]	DIC Max Deflection Top Mid [mm]	FEA Peak Load [kN]	Instron Peak Load [kN]
PMR1-E1	17.8	31.0	12.8	15.3
TRI1-E2	41.1	23.8	9.1	8.4
PMR1-E3	6.7	25.7	12.9	15.0
TRI1-E4	17.4	15.2	9.0	9.3
PMR1-E5	5.2	17.0	12.3	14.8
TRI1-E6	11.2	9.7	8.8	9.8

The peak loads showed good correlation between experimental results and finite elements analyses. The FEA peak loads ranged from 83% and 108% of the experimental data. The data collected from experiments was generally higher than FEA (See Figure 48). The traditional topologies correlated better than the PMR topologies.

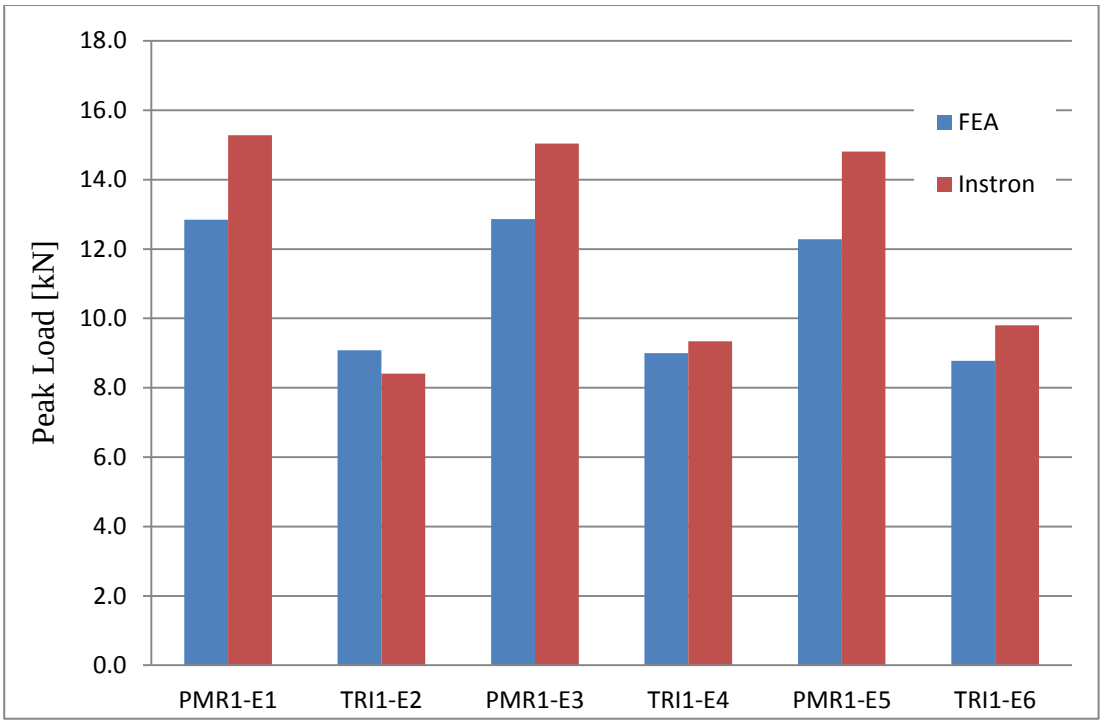

Figure 48 - Peak Load Comparison FEA vs Experiment

Figure 49 shows the maximum midpoint deflection of the FEA analyses versus the experimental values. The analyses of the PMR showed that they were much stiffer in FEA that in the experiments. The deflection in the FEA was much less than the experimental values. While conversely the typical structures showed more deflection in FEA than in experiments. The lower energy experiments, Experiments 5 and 6 showed the best correlation to the finite element model results as a pair.

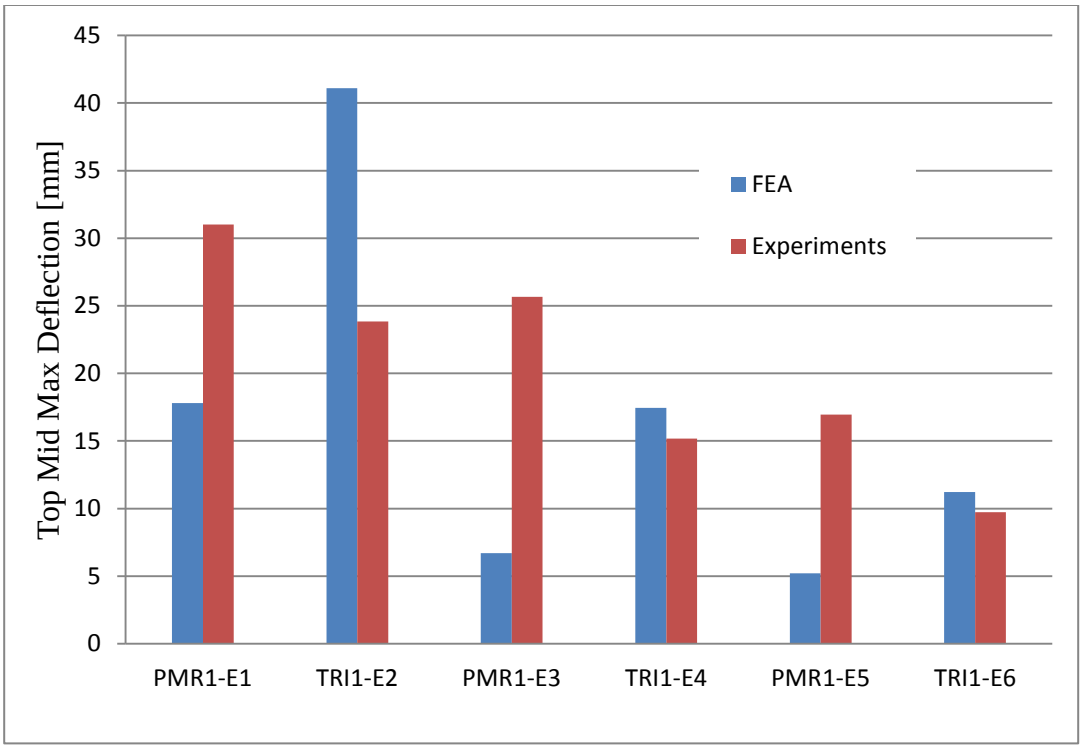

Figure 49 - Max Deflection Comparison FEA vs Experiment

It is also interesting to compare the load over time and how the FEA differs from the experimental results. The following two charts compare the load profile of experiment 5 and 6 with the load profile from their respective finite element analysis (See Figure 50 and Figure 51). As stated the peak loads are lower for the FEA than in the experiments. The general shape of the profiles does match up. The PMR shows a sudden peak and a quick reduction followed by the gentle decay. The traditional profiles shows a peak with a plateau followed by a sudden drop. After which the FEA becomes erratic and difficult to compare to the experimental results.

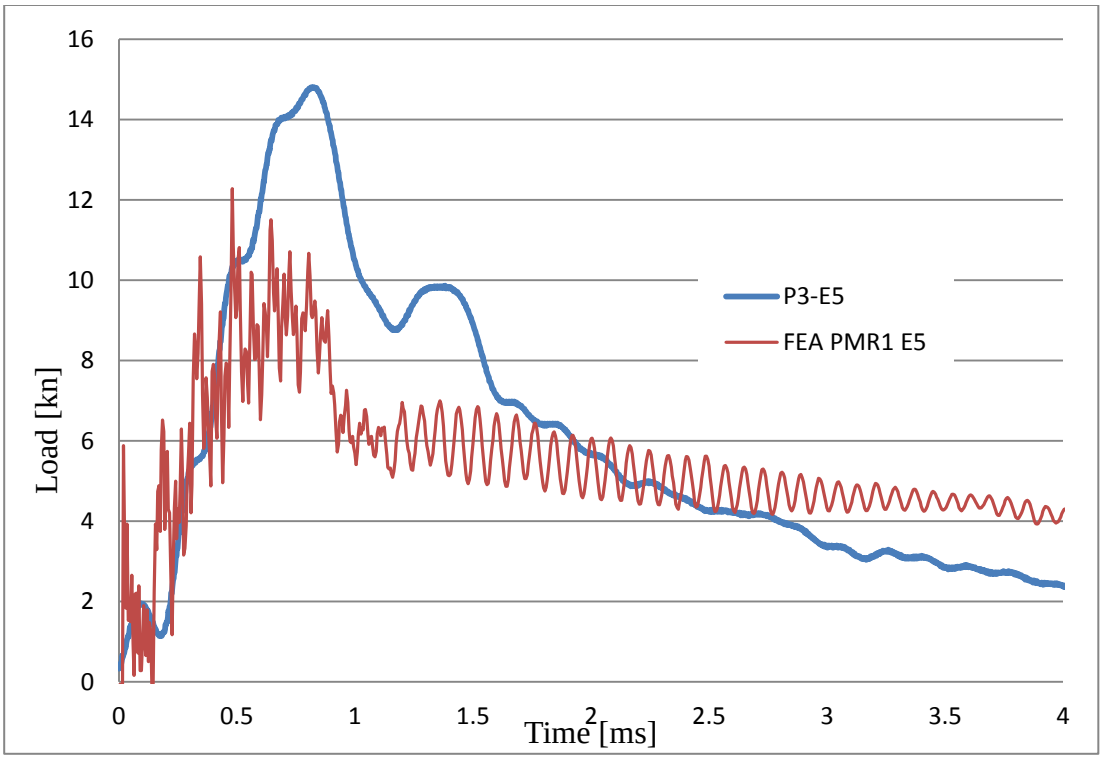

Figure 50 – Load Profile - Experiment 5 vs FEA

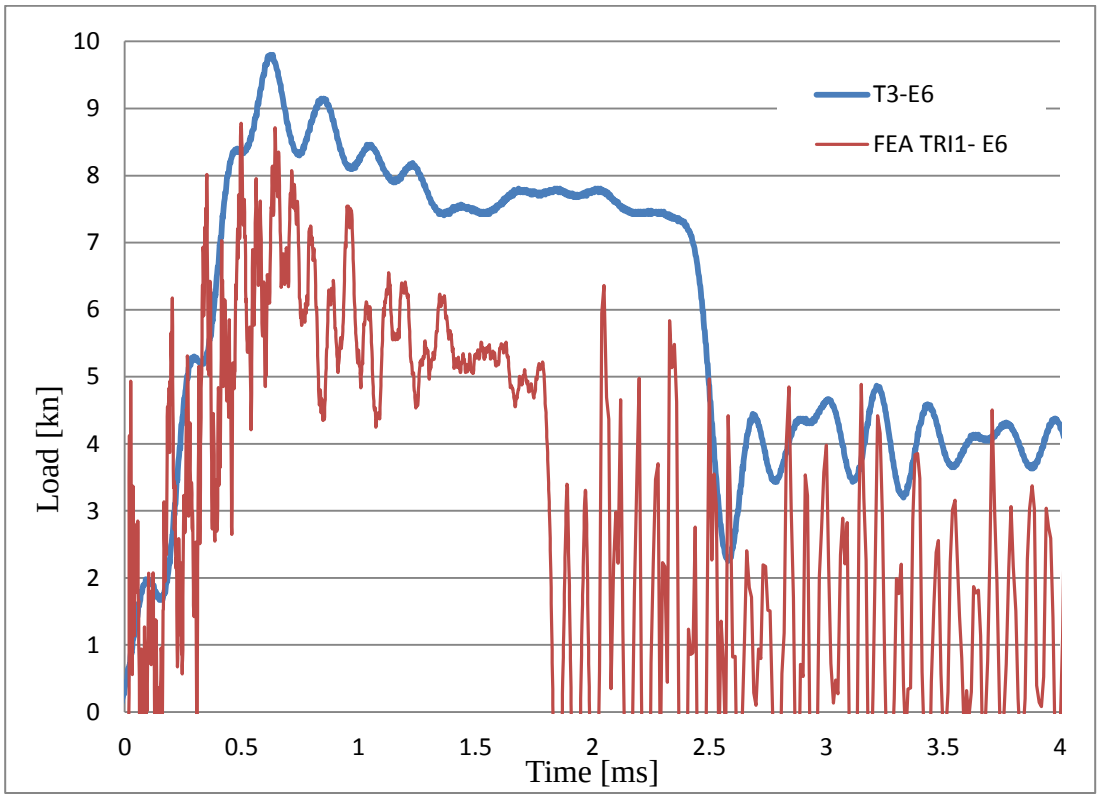

Figure 51 – Load Profile - Experiment 6 vs FEA

Figure 52 through Figure 57 show the tup losing contact in each of the dynamic analysis performed with the exception of E2L-TRI1. In this analysis the tup and rigid striker are not arrested by the end of the analysis. Figure 52 shows the results of PMR1 after being exposed to the same loading as conducted in experiment 1. The buckling failure is similar to the Mode 2 failure predicted by the buckling analysis. In this case however the member buckles outward to the left side instead of inward as with the experiment. The direction of the buckling is difficult to predict and plays little role in the overall outcome. The FEA predicts the same failure as seen in the experiments (See Figure 20)

Figure 53 shows the dynamic FEA of the traditional profile exposed to the same loading as experiment 2. The FEA differs from the experiment in that the analysis does not show the sample arresting the crosshead. The simulation continues until the maximum time of 30 milliseconds without the crosshead coming to a stop. The FEA does predict the similar failures observed in the experiment (See Figure 23). The sample fails in tension in the same location and the internal member below the structure buckles internally as it did in the experiment. One explanation for the difference may be that the material model undervalues the energy of fracture. In that the energy required to make the tensile fracture is more than what the program has allocated. This could be because the fracture in the FEA is very smooth as compared to the fracture observed in the experiments (See Figure 21). Rough cracks are high energy because a rough crack has a high surface area. In the FEA the crack surface area is lower and therefor the energy required to create that fracture is less than observed in the experiments.

Figure 54 and Figure 55 show the results of the FEA of Experiments 3 and 4. The failures observed in the analysis again match what was observed in the experiments. In these cases both were able to arrest the crosshead. However the FEA of experiment 4 shown in Figure 55 predicts the tensile failure of the member in the upper left corner. While the experimental specimen did show some plastic deformation in this area in the way of necking (See Figure 22), it did not in fact break as shown in the FEA. This again indicates that the dynamic analysis undervalues the energy required to break the specimen in tension.

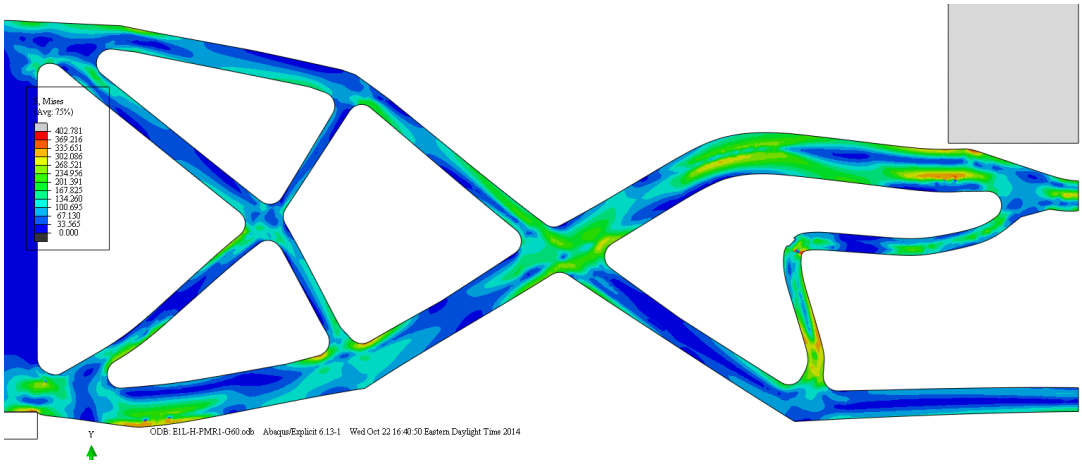

Figure 52 - E1L-PMR1 Mises Stress 21.5 ms

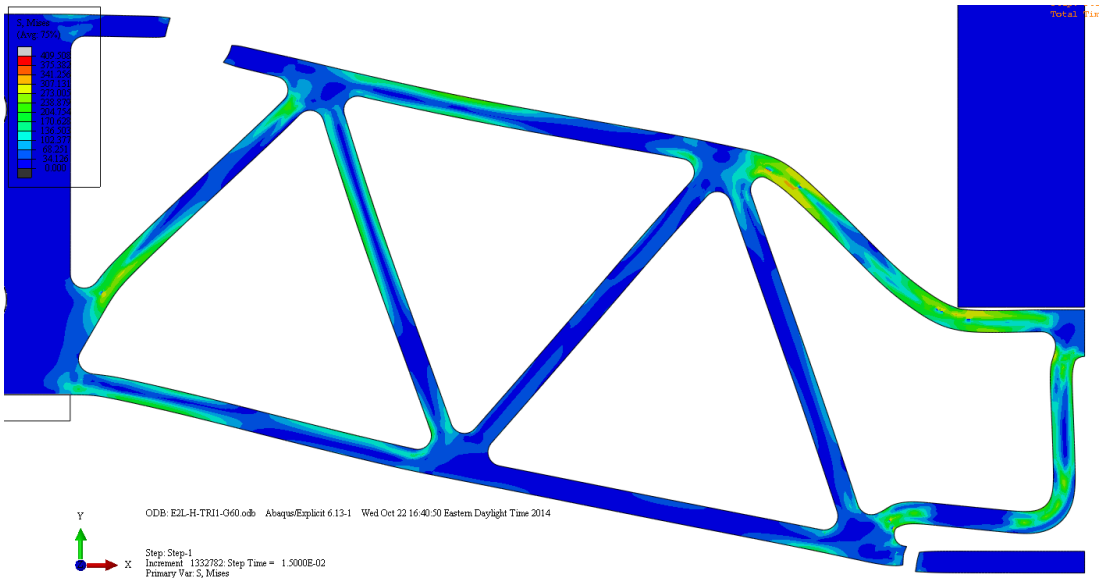

Figure 53 - E2L-TRI1 Mises Stress 15ms

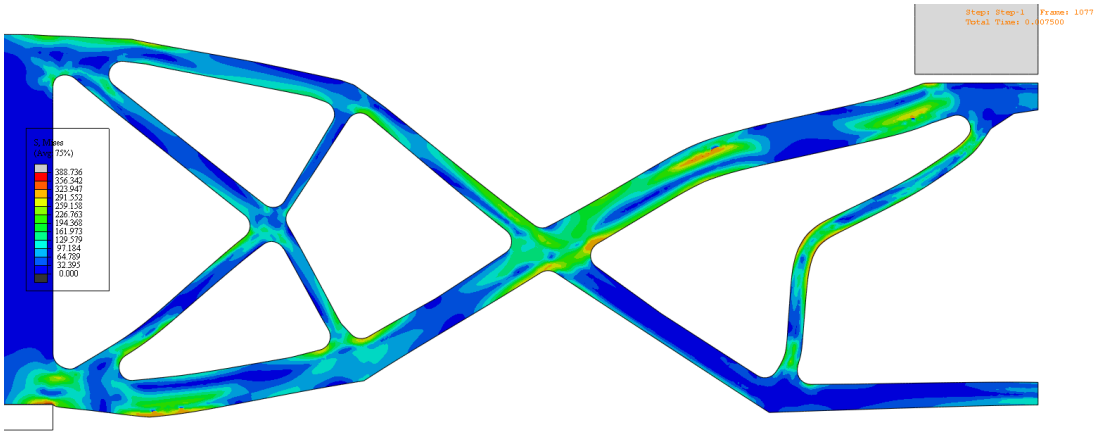

Figure 54 - E3L-PMR1 Mises Stress 7.5ms

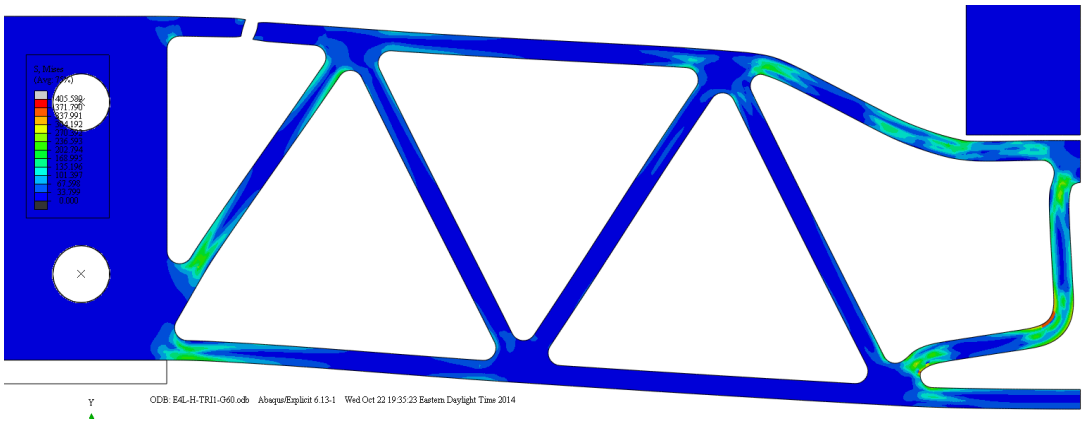

Figure 55 - E4L-TRI1 Mises Stress 22.5ms

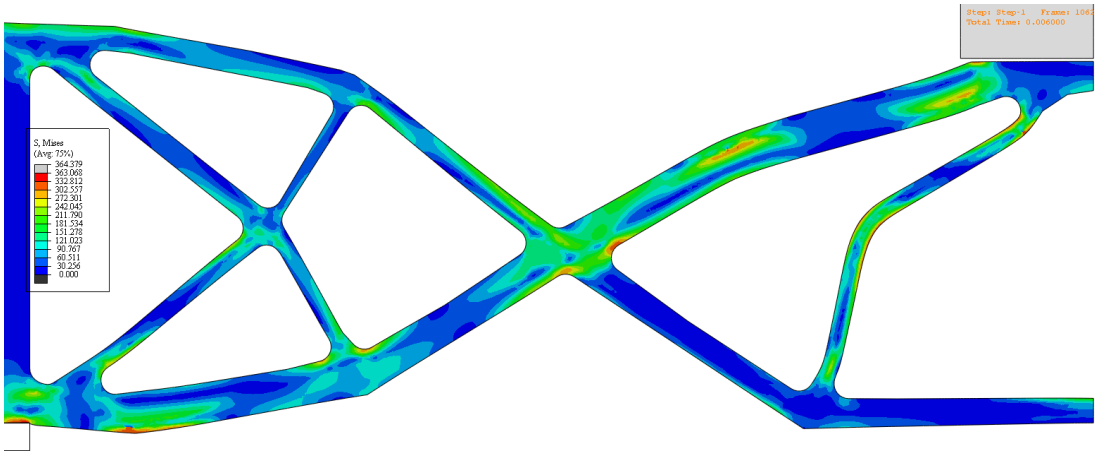

Figure 56 - E5L-PMR1 Mises Stress 6ms

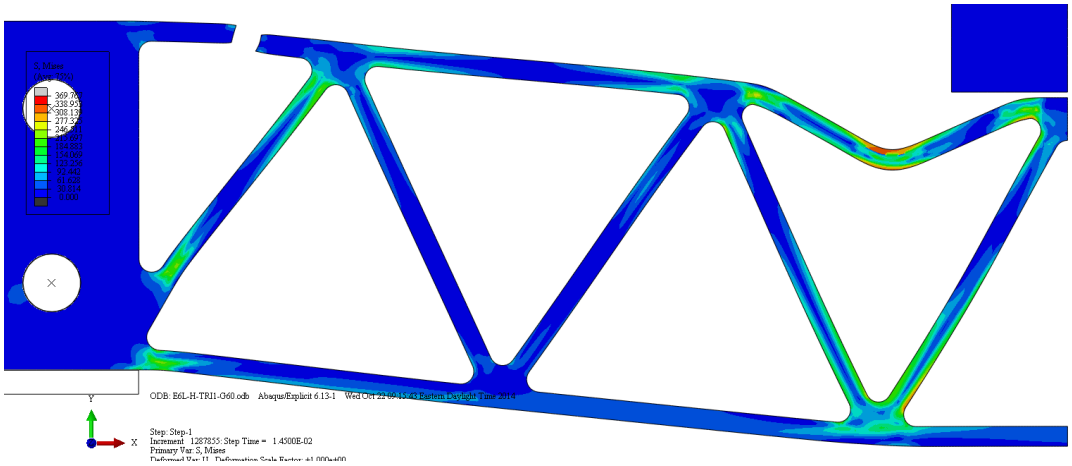

Figure 57 - E6L-TRI1 Mises Stress 14.5ms

The finite element model does predict how the profiles tested fail. While the higher kinetic energy impacts do not correlate well with the experimental results. The lower energy impacts E5L-PMR1 and E6L-TRI1 provide the best correlation between FEA and experimental results. The higher volume fraction topologies are tested at similar energy levels.

5. EVALUATION OF TOPOLOGIES

Three main sources of failures are observed, plastic deformation, buckling, and tensile failure. The first two PMR profiles failed due to buckling while PMR3 through PMR6 failed in tension in the upper left corner of the domain (See Figure 58, Figure 59 & Figure 60).

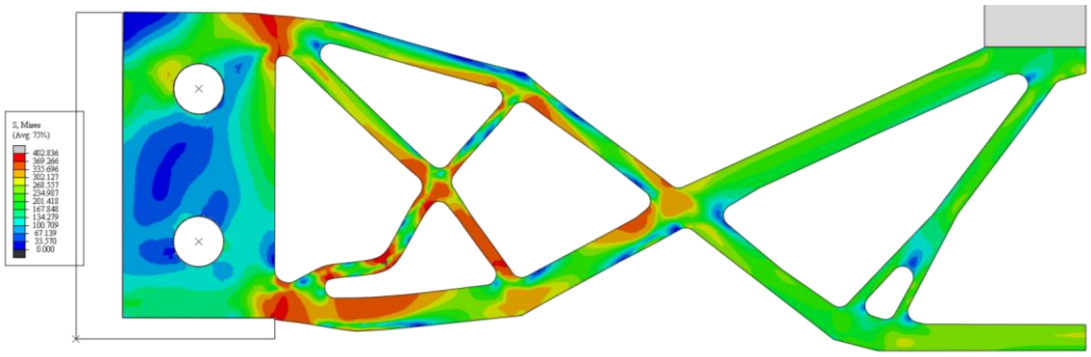

Figure 58 - PMR2 Dynamic Failure 2.1ms

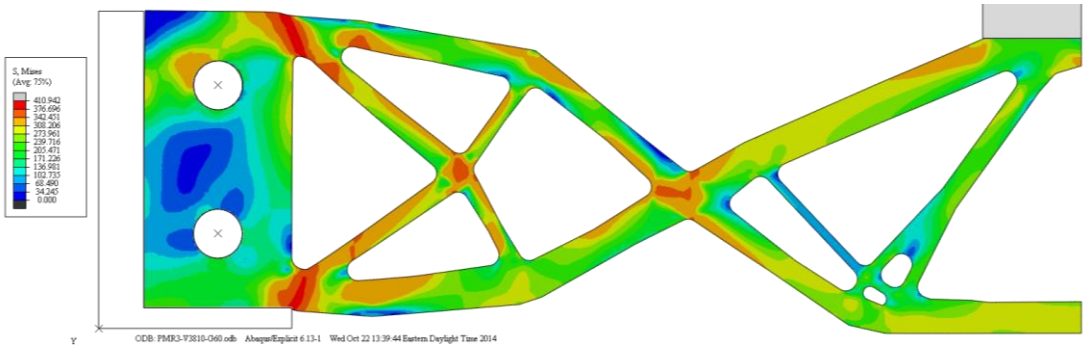

Figure 59 - PMR3 Dynamic Failure 1.2ms

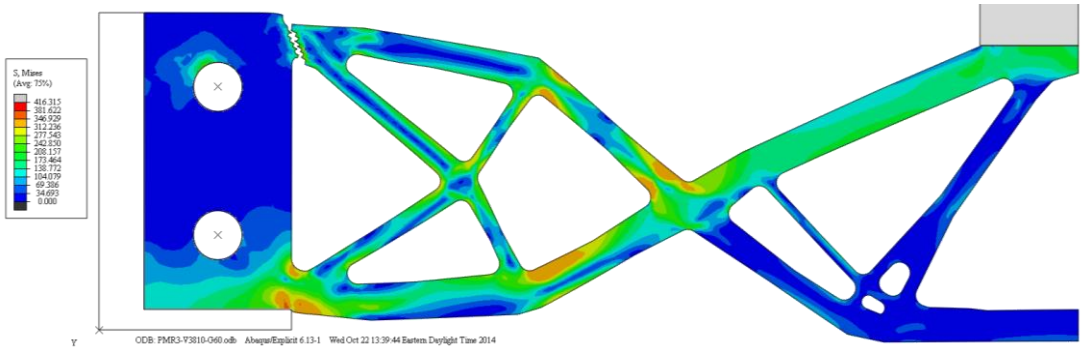

Figure 60 - PMR3 Tensile Failure 1.9ms

TRI1 suffered from both buckling and tensile failure. TRI2 and TRI3 also buckled but did not fail in tension anywhere.

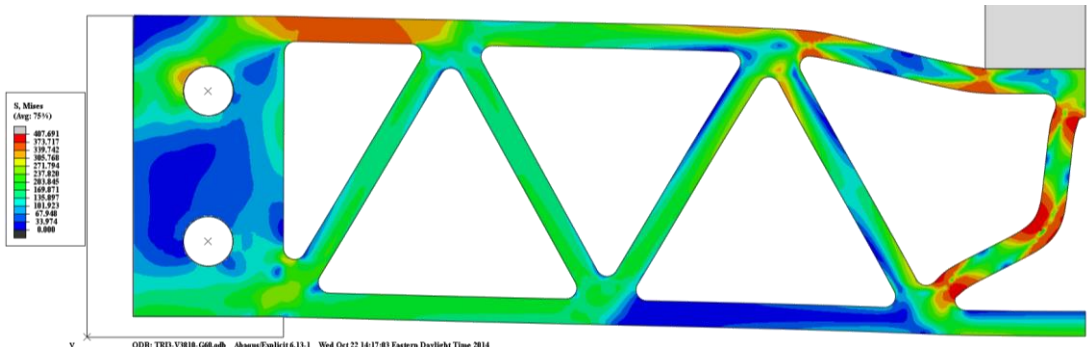

Figure 61 - TRI3 Buckling Failure 5.3ms

PMR7 through PMR9 and TRI4 through TRI9 suffered only plastic deformation at the around the left side of the design domain. After dynamic analysis the stiffness of the profiles is again obtained. The post impact static analysis uses the original mesh from the dynamic analysis. All variable from the last increment of the dynamic analysis are imported into the static analysis as a predefined field. This includes stress, displacement, velocity, acceleration etc. Also the status variable is also imported. The status variable keeps track of element deletion. Any elements deleted in the dynamic analysis are also deleted from the dynamic analysis. The post and pre impact structural stiffness of all the profiles are shown in Figure 63.

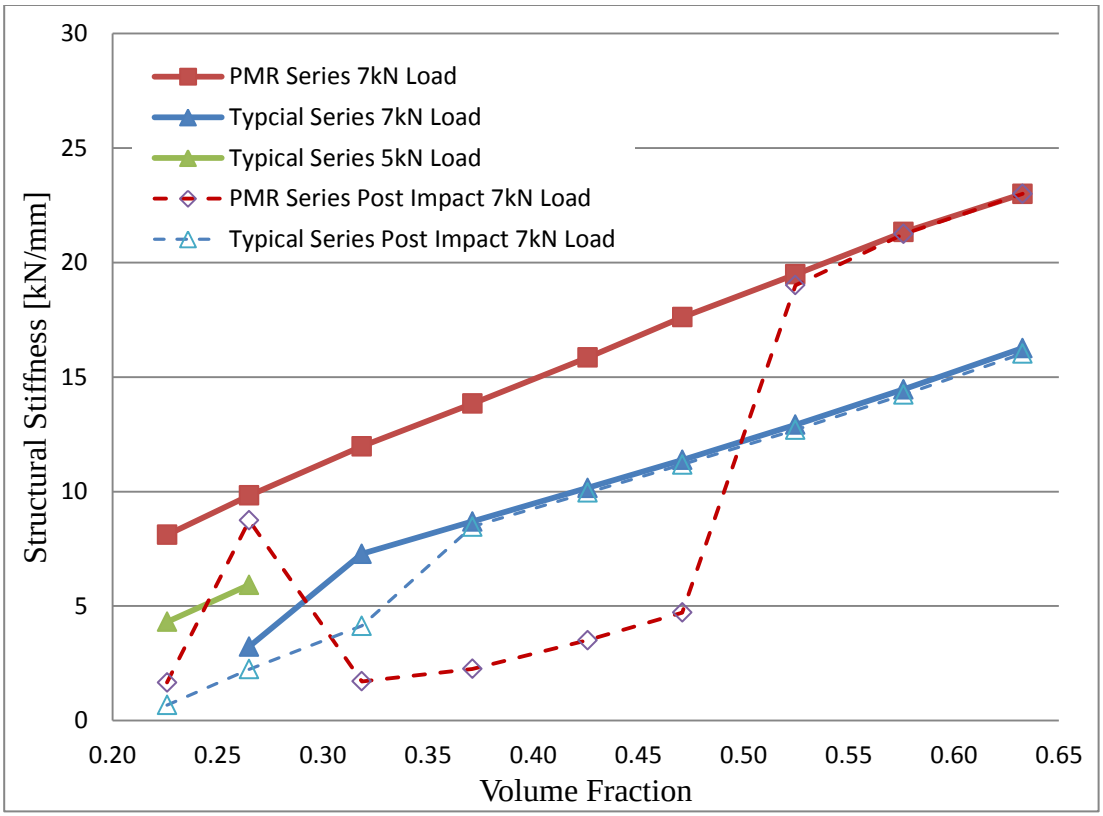

Figure 62 – Structural Stiffness Pre and Post Dynamic Impact

The PMR structures that suffered tensile failure at the attachment point showed severe reduction in stiffness. The stiffness of these structures fell well below their typical counterparts. The three smallest typical structures buckled and showed a large drop in stiffness. The larger typical profiles underwent plastic deformation and saw little reduction in structural stiffness. Of all the failure mechanism seen, tensile failure causes the greatest reduction in stiffness for these cases.

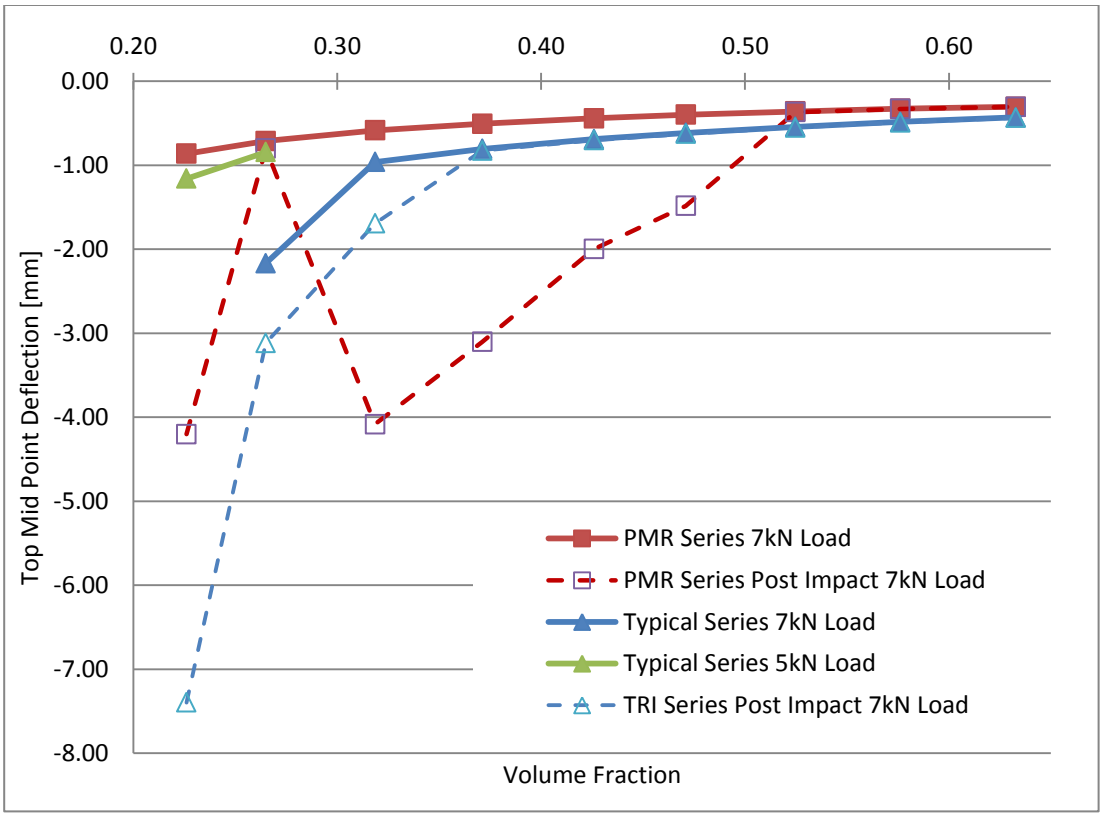

Figure 63 – Static Deflection of Profiles Pre and Post Impact

6. CONCLUSION

It is clear that topologies that are optimized for stiffness perform extremely well under static loading conditions as compared to traditional lightweight structures. Under dynamic impact conditions, the stiffness of the structure determines the load. The stiffer the structure the higher the load response will be. This was observed in both the experimental and FEA results. The PMR series of topologies showed high load response that slowed the impact load more quickly than the traditional series. The lighter topologies with lower volume fraction sustained large deformation and damage.

At higher volume fractions (0.52, 0.58 and 0.68), where the structures are larger and more robust, the impact is less severe and the topologies, PMR and traditional, are able to withstand the impact with only slight plastic deformation. The kinetic energy is increased linearly as the volume fraction is increased, but the results are not uniform. The low volume fraction topologies saw high damage and as the volume fraction was increased the damage observed decreased. The traditional series saw marked improvement with only slight plastic deformation starting at a volume fraction of 0.37. The PMR series began showing only plastic deformation at a volume fraction of 0.52. However once both topologies showed only plastic deformation the PMR topologies clearly performed better with a much high stiffness before and after impact and deflected less during the impact.

The PMR series performs better than the traditional series until the kinetic energy increases enough to compromise the structure in the form of tensile failures, as observed in the lower volume fraction topologies.

Once the impacts are large enough to cause large deformation failures like buckling or tensile failures, the traditional structures with an equilateral triangle topology tend to perform better because they are able to arrest the impact over a longer time period of time because of their reduced load response. When the traditional structures did fail due to tension or buckling, another load path was available to transmit the load, allowing the structure to absorb additional energy. The enhanced static strength of the optimized topologies was a hindrance at critical levels of dynamic loading. The optimized structures are so stiff they do not allow for the mass to be slowed gradually over time. This caused high member loads leading to tensile failures. The tensile failure did absorb energy and allowed the impact to be arrested quickly. But these failures severely reduced the load bearing capacity of the overall structure because the optimized structure depends on all members to remain intact in order to effectively carry the load. The statically optimized structures performed well for low kinetic energy levels but tended to fail critically before the traditional series and once they had failed they did not carry loads as effectively as the traditional series. Structures optimized for stiffness can be used when the dynamic impacts are expected to be low and when minimal deflection in static and dynamic situations is desirable. In situations where high energy impacts must be accounted for, some stiffness must be sacrificed in order to reduce damage. The addition of members might be required to provide additional load paths in the event of any failed members.

In order to optimize the structural resistance to high energy impact, the results indicate the need for alternative optimization procedures for use in the design of these structures. Future work will focus on creating a new optimization algorithm. This

algorithm will use an iterative prescribed material distribution scheme but instead of performing a static analysis for each iteration, a dynamic analysis will be performed instead. The results of the dynamic analysis will be used by the PMR to redistribute material from low strain energy locations to high strain energy locations. This new method may be able to optimized structures for dynamic loading conditions.

APPENDIX 1: Dynamic Results Figures

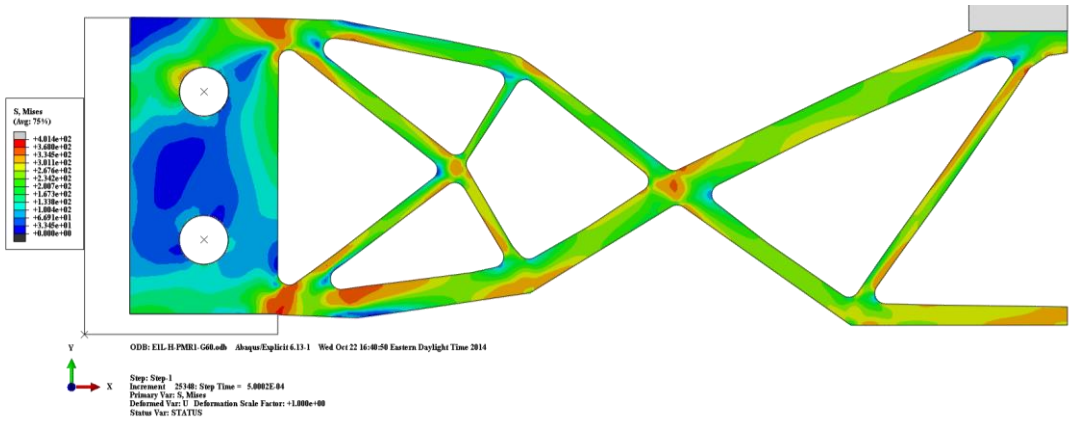

Figure 64 - PMR1 Experiment 1 - 0.5ms

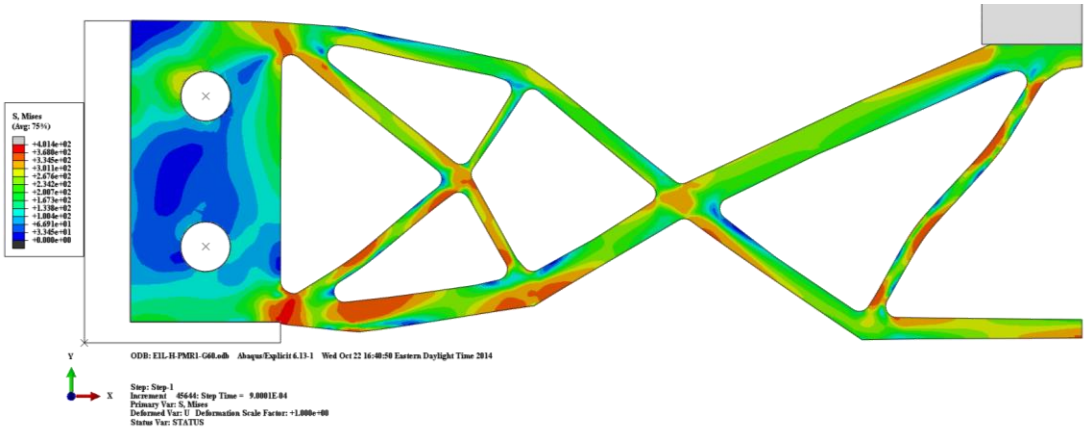

Figure 65 - PMR1 Experiment 1 - 0.9ms

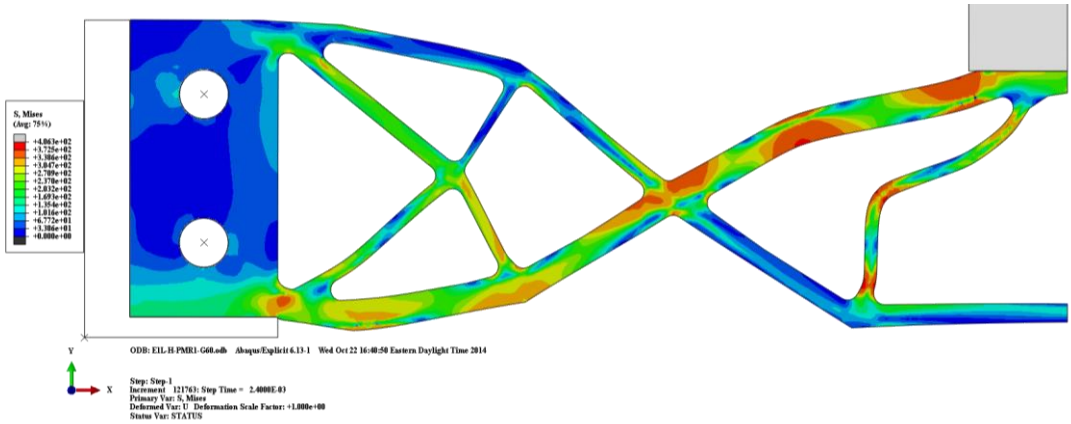

Figure 66 - PMR1 Experiment 1 - 2.4ms

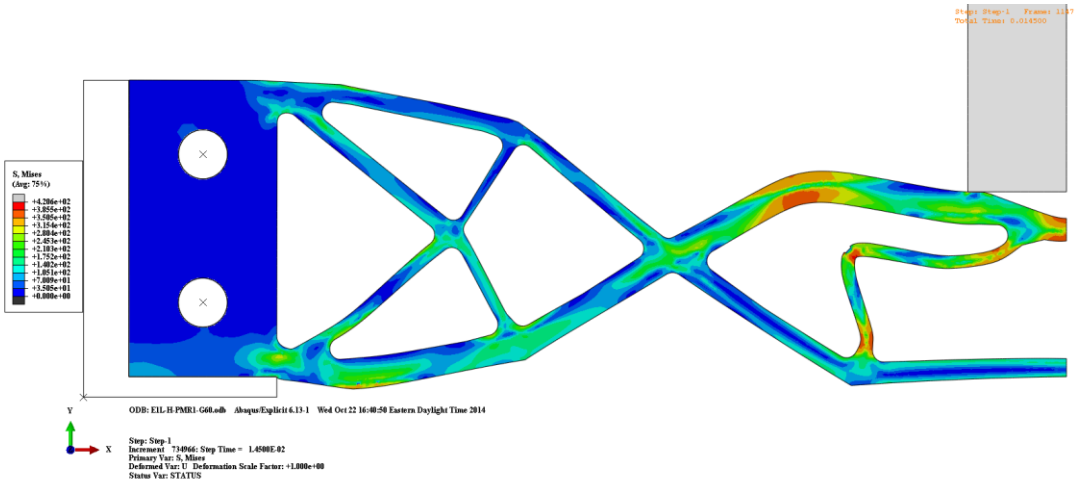

Figure 67 - PMR1 Experiment 1 - 14.5ms

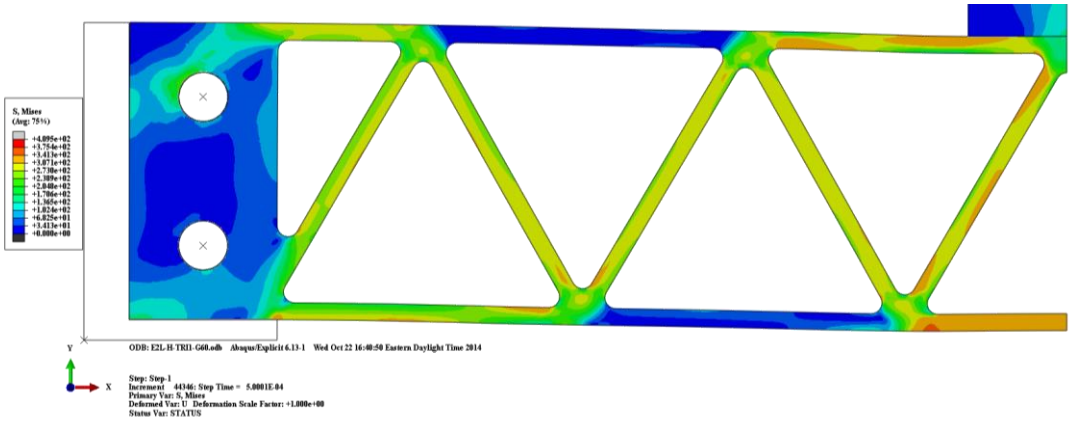

Figure 68 - TRI1 Experiment 2 - 0.5ms

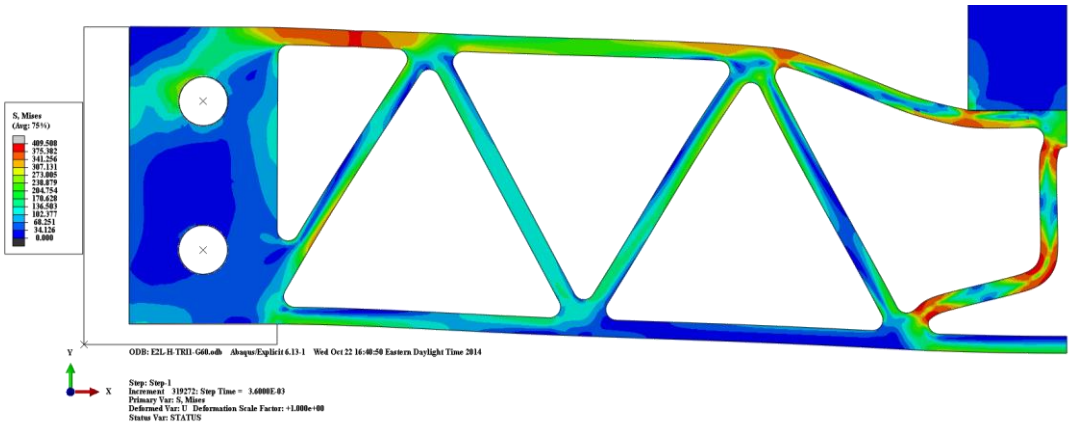

Figure 69 - TRI1 Experiment 2 - 3.6ms

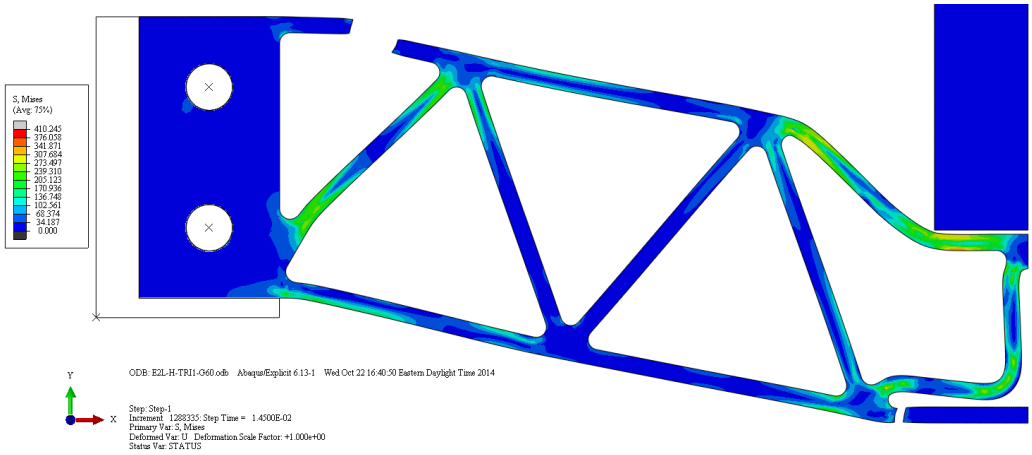

Figure 70 - TRI1 Experiment 2 - 14.5ms

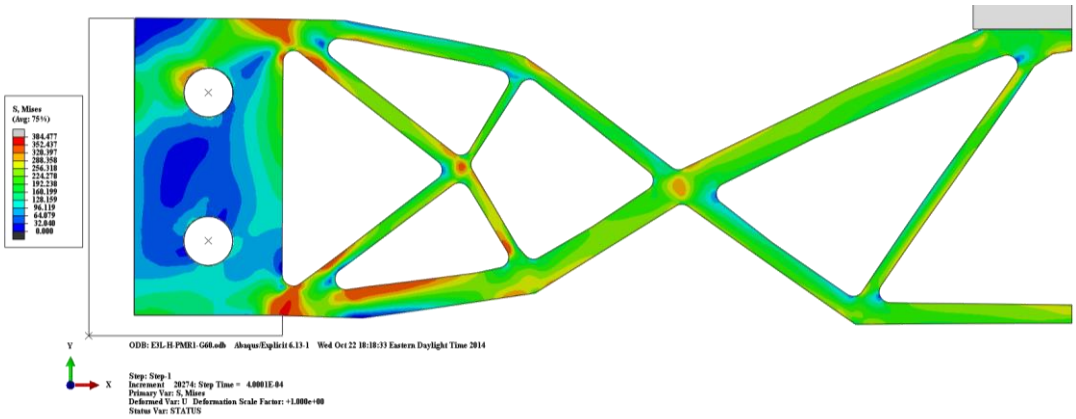

Figure 71 – PMR1 Experiment 3 - 0.4ms

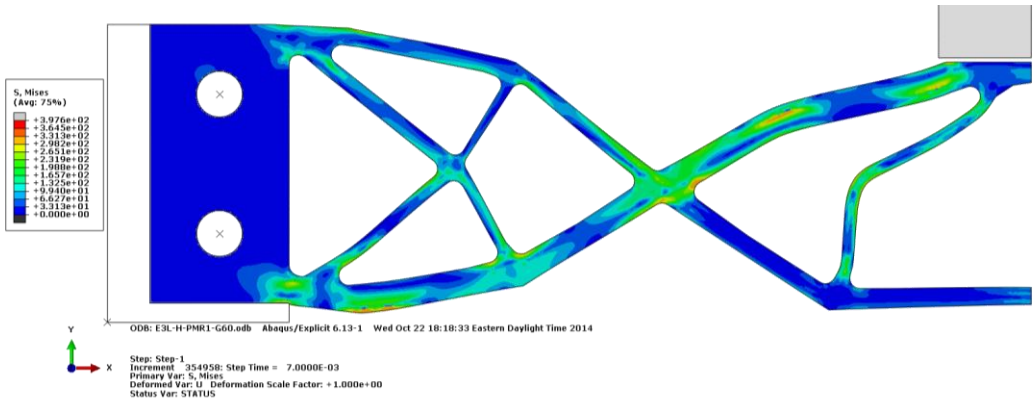

Figure 72 - PMR1 Experiment 3 - 7ms

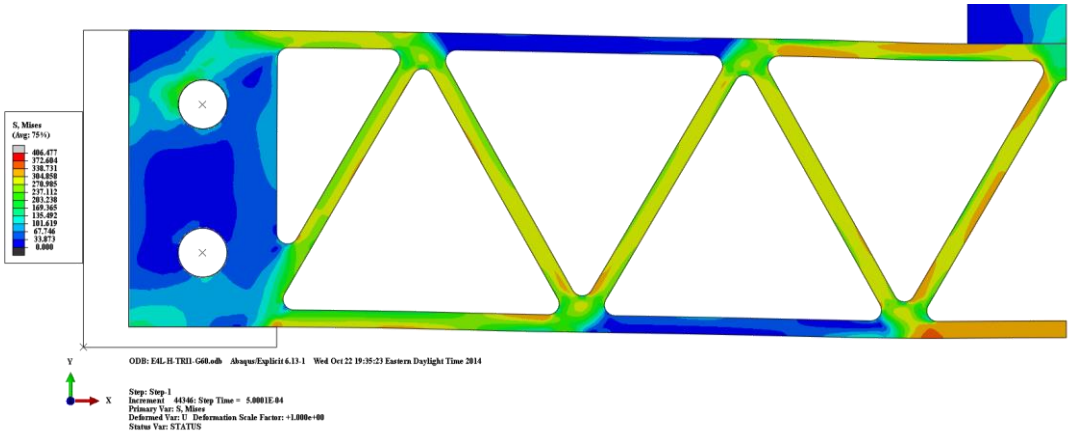

Figure 73- TRI1 Experiment 4 - 0.5ms

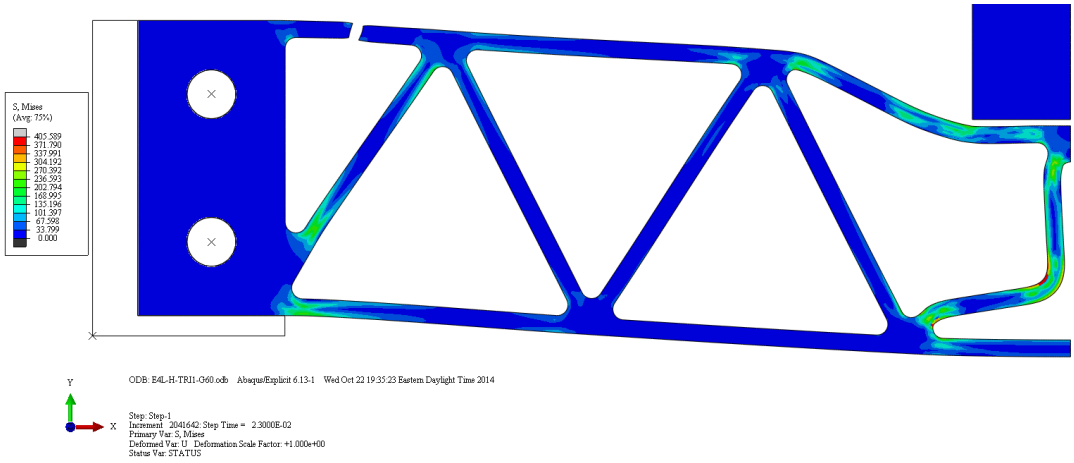

Figure 74 - TRI1 Experiment 4 - 23ms

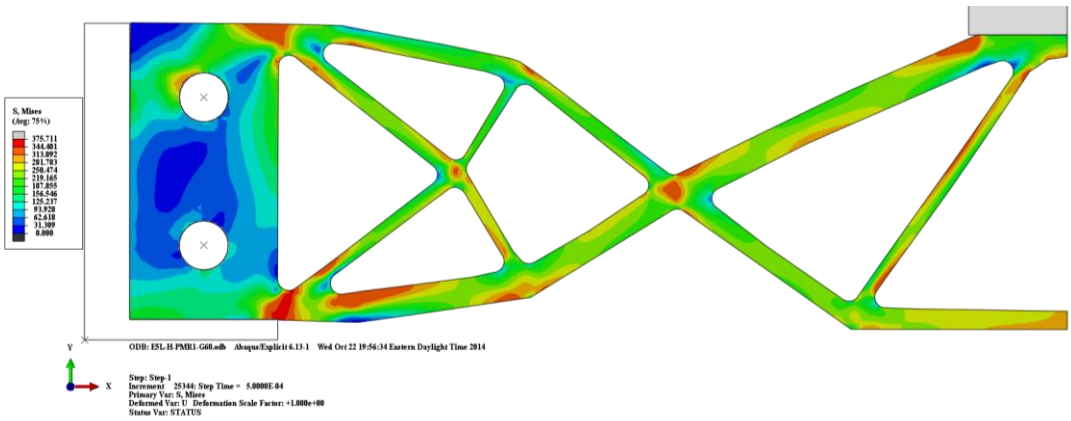

Figure 75 - PMR1 Experiment 5 - 0.5ms

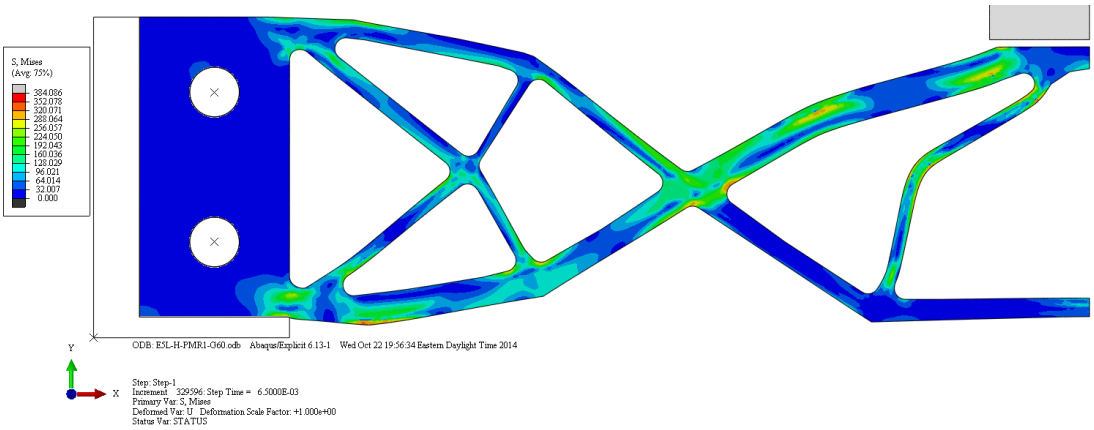

Figure 76 - PMR1 Experiment 5 - 6.5ms

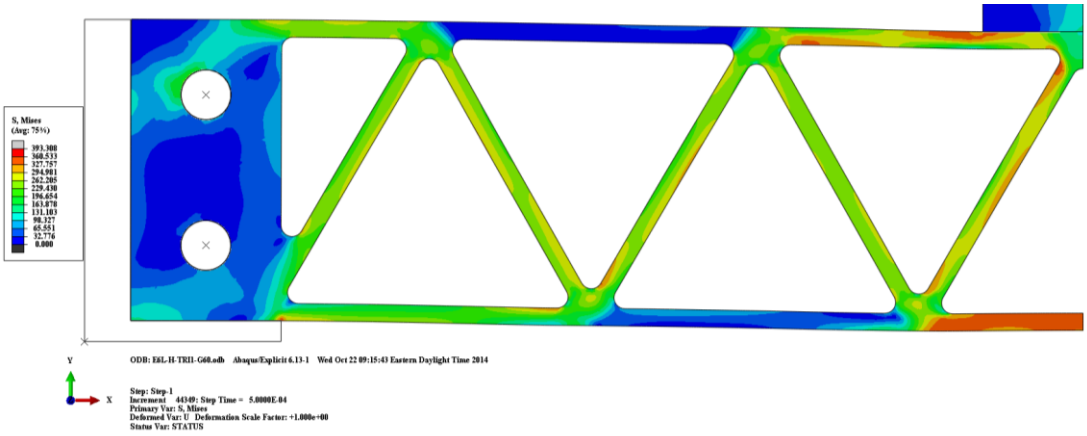

Figure 77 - TRI1 Experiment 6 - 0.5ms

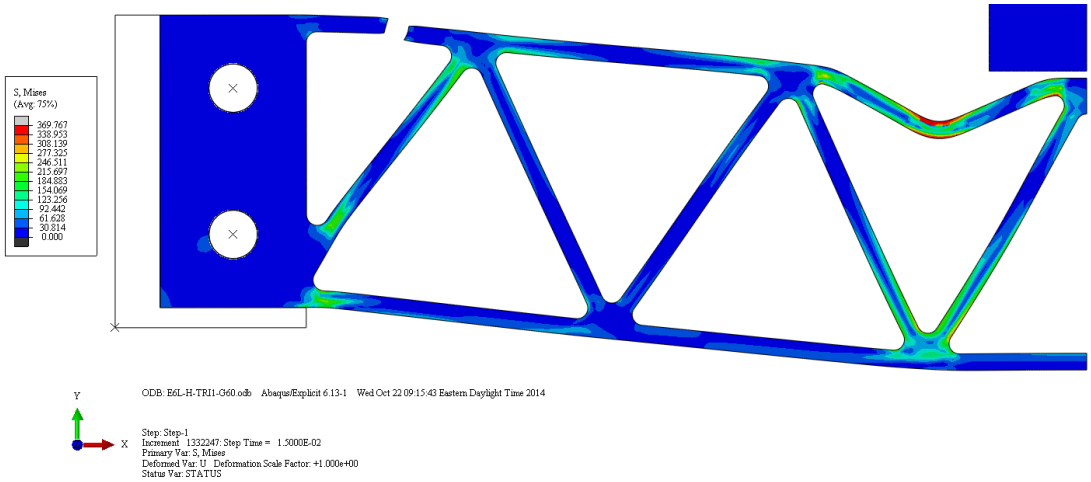

Figure 78 - TRI1 Experiment 6 - 15ms

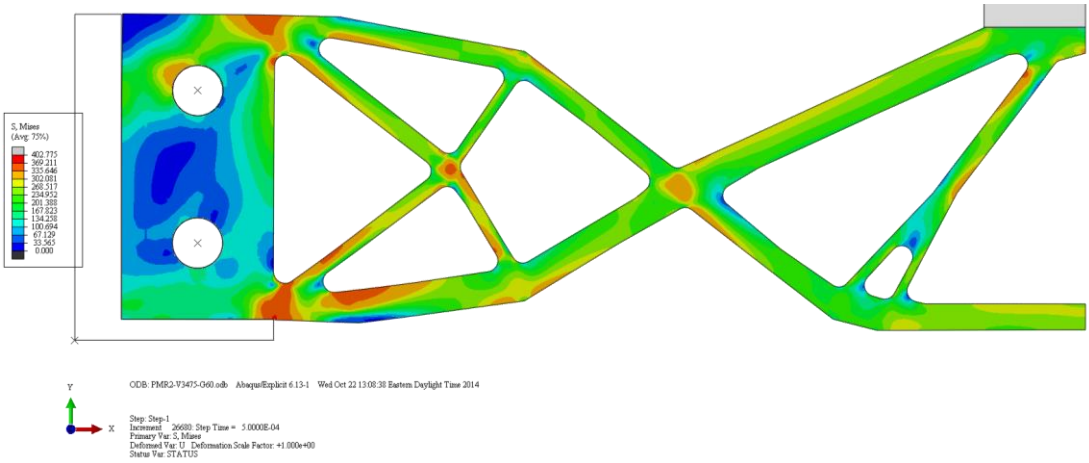

Figure 79 - PMR2 - 0.5ms

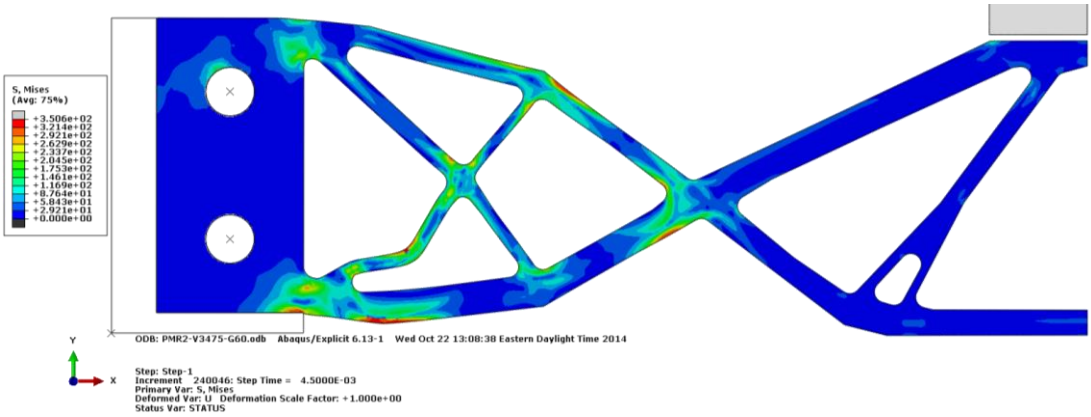

Figure 80 - PMR2 - 4.5ms

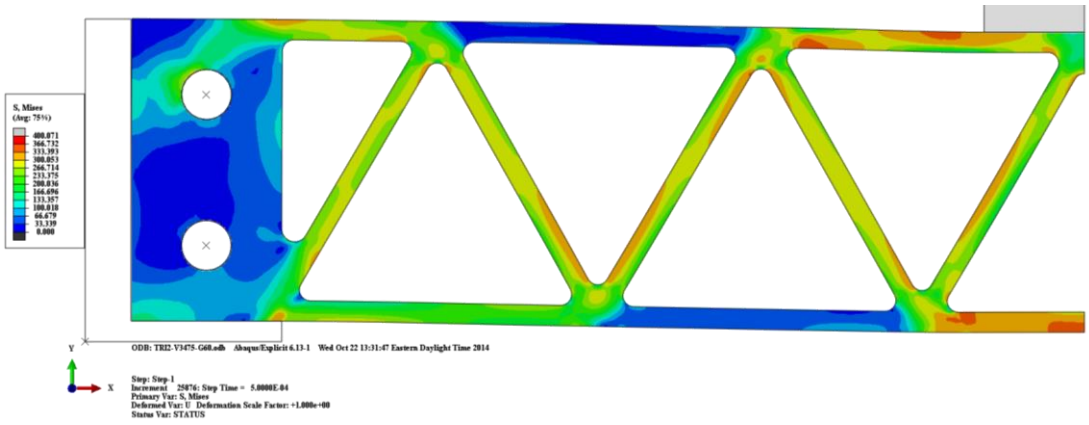

Figure 81 - TRI2 - 0.5ms

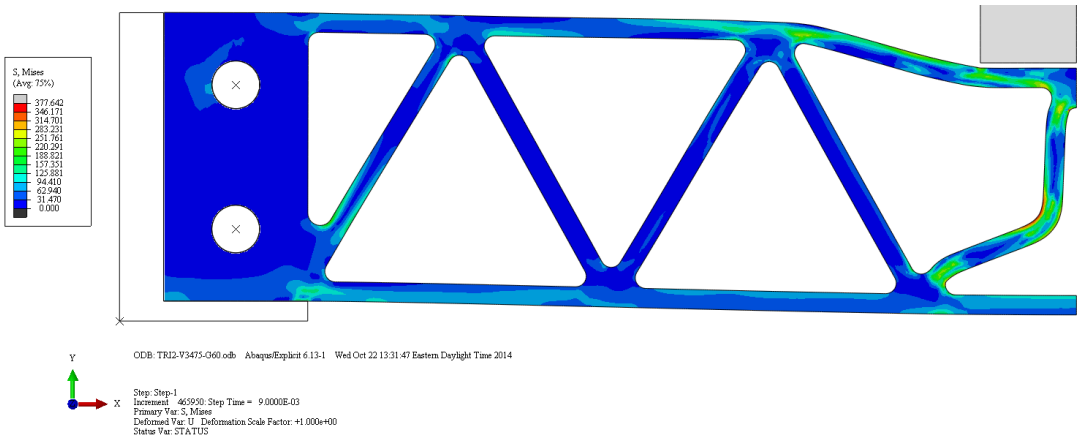

Figure 82 - TRI2 - 9ms

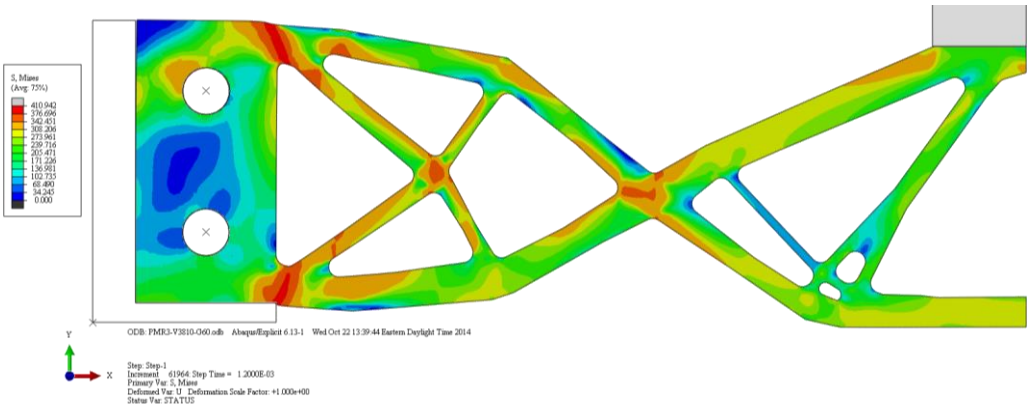

Figure 83 - PMR3 - 1.2ms

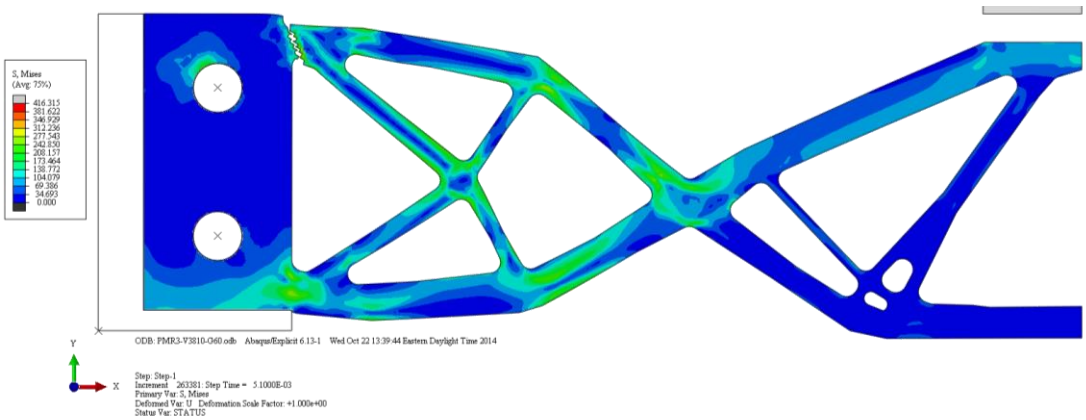

Figure 84 - PMR3 - 5.1ms

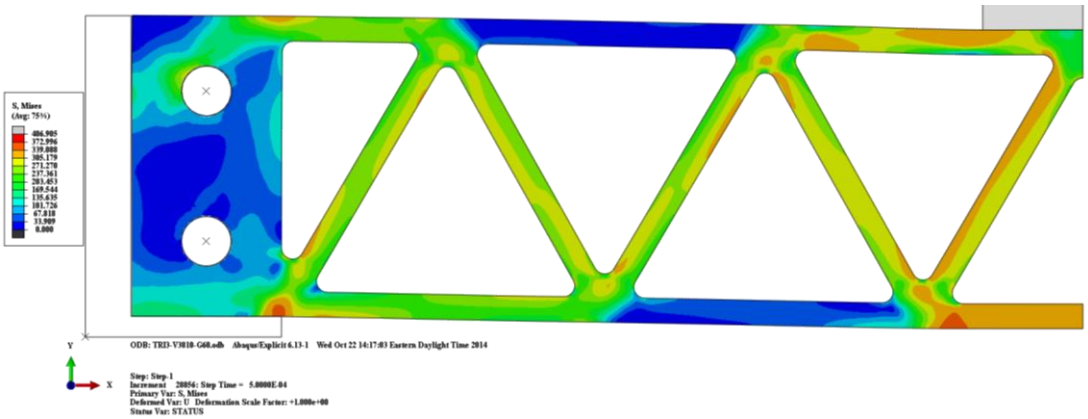

Figure 85 - TRI3 - 0.5ms

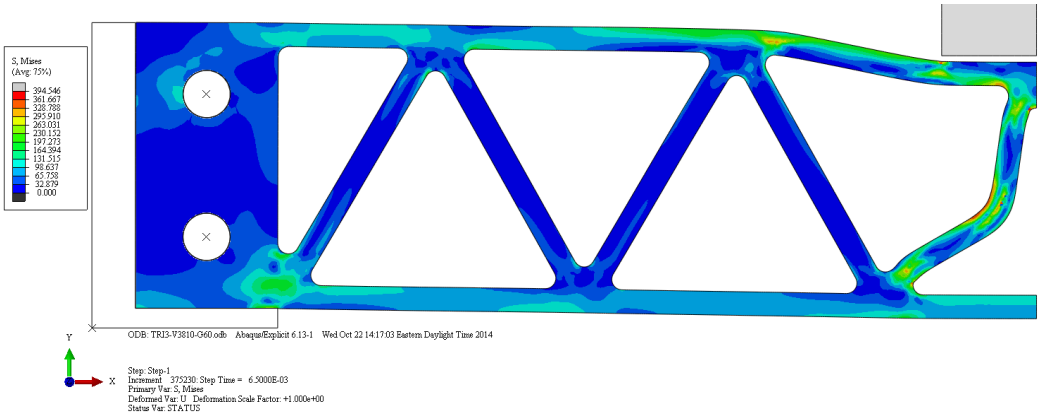

Figure 86 - TRI3 - 6.5ms

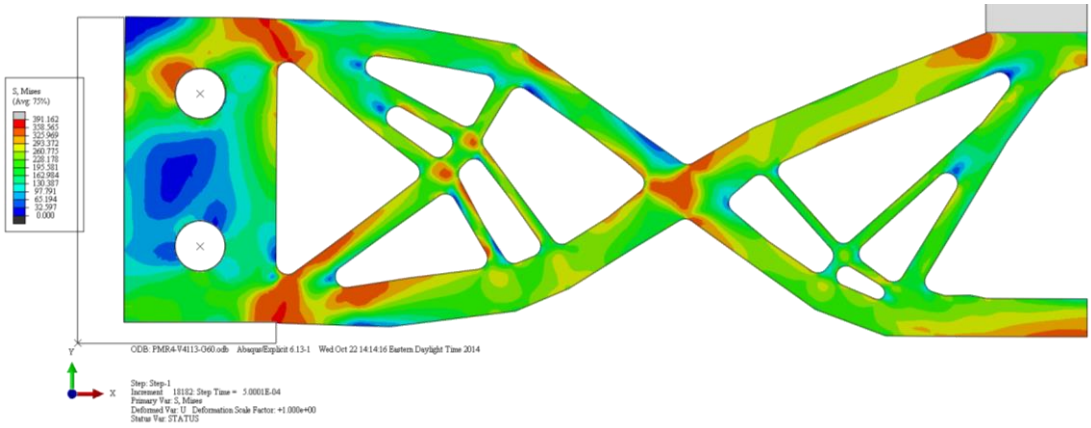

Figure 87 - PMR4 - 0.5ms

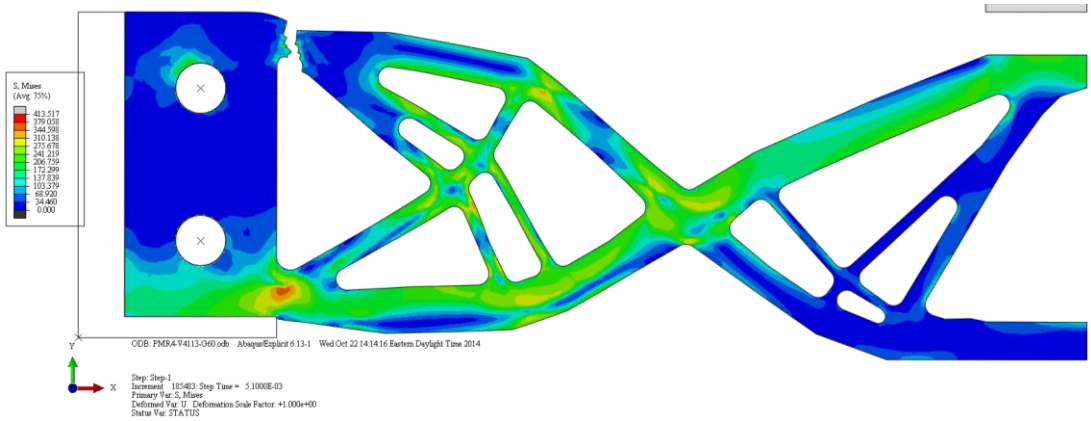

Figure 88 - PMR4 - 5.1ms

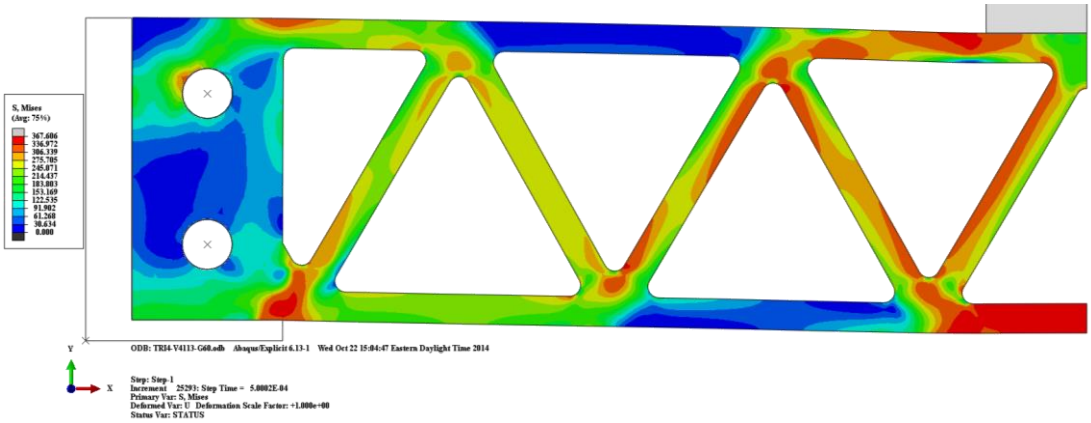

Figure 89 - TRI4 - 0.5ms

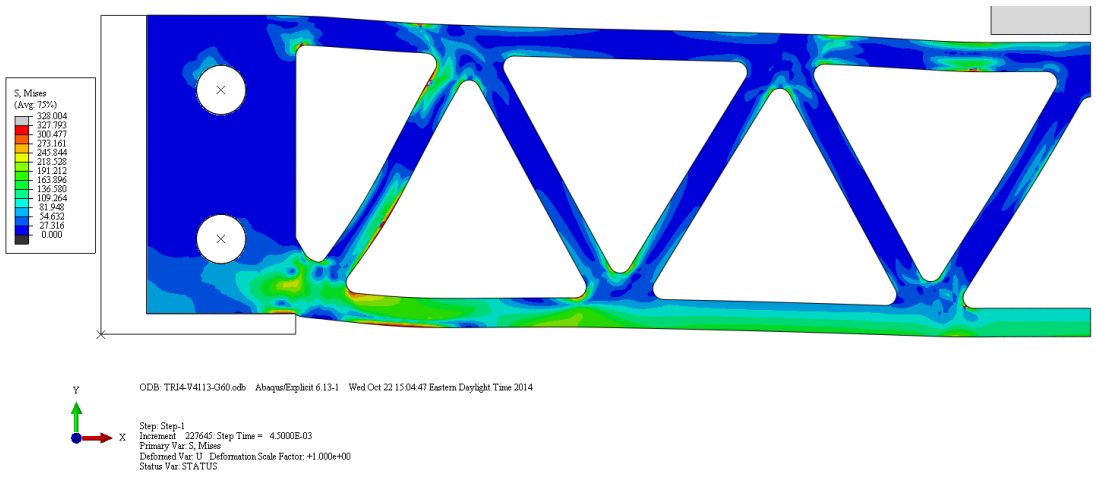

Figure 90 - TRI4 - 4.5ms

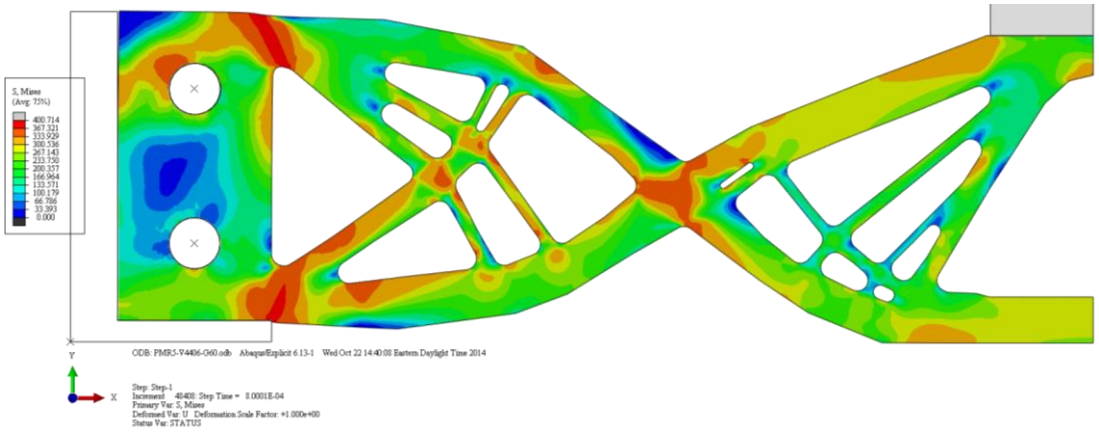

Figure 91 - PMR5 - 0.8ms

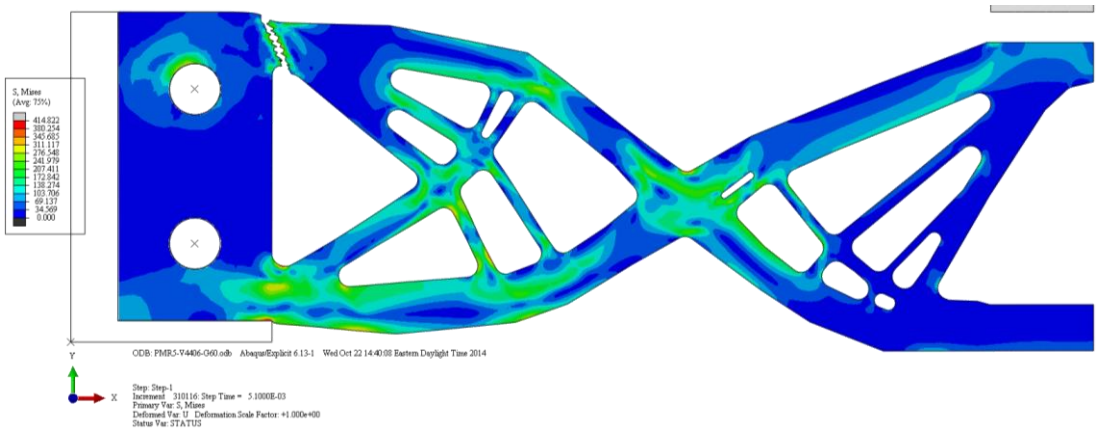

Figure 92 - PMR5 - 5.1ms

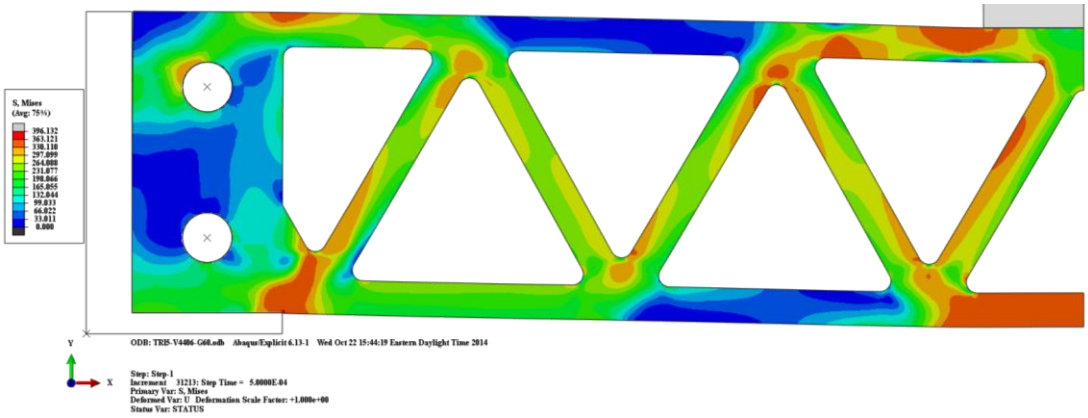

Figure 93 - TRI5 - 0.5ms

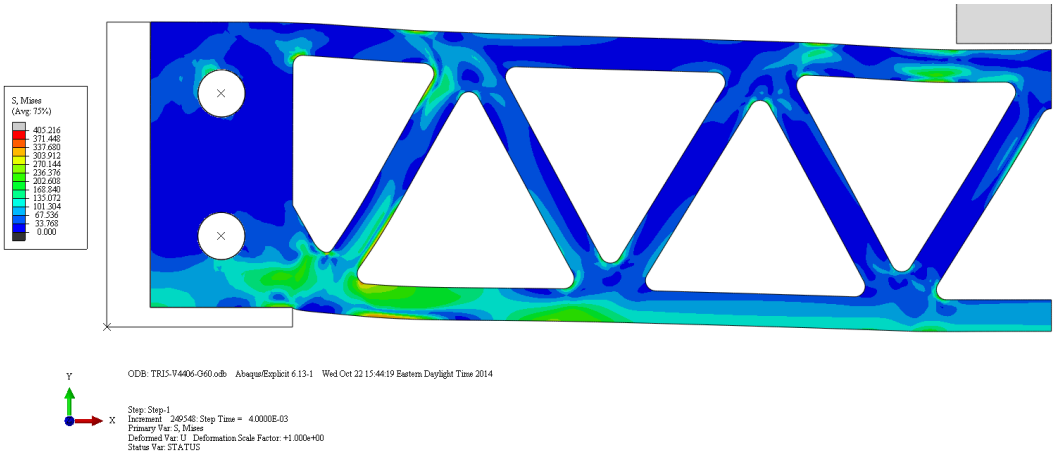

Figure 94 - TRI5 - 4ms

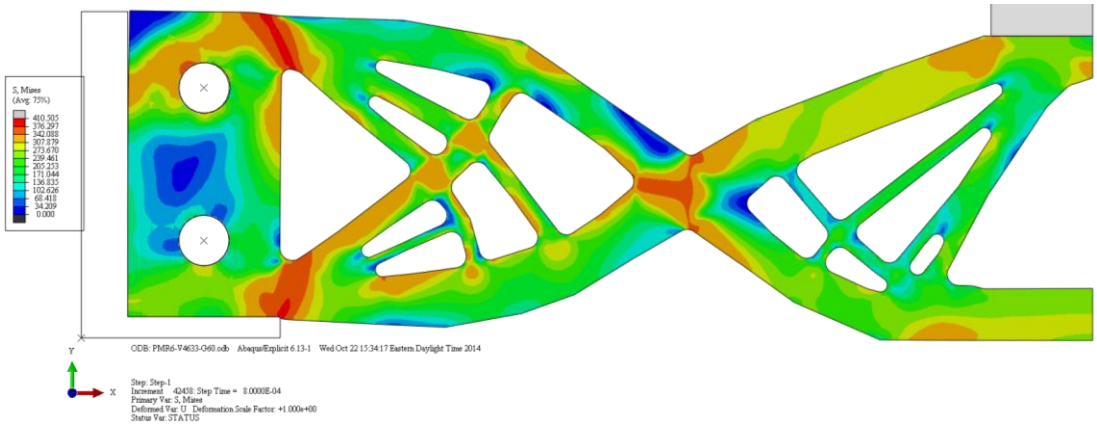

Figure 95- PMR6 - 0.8ms

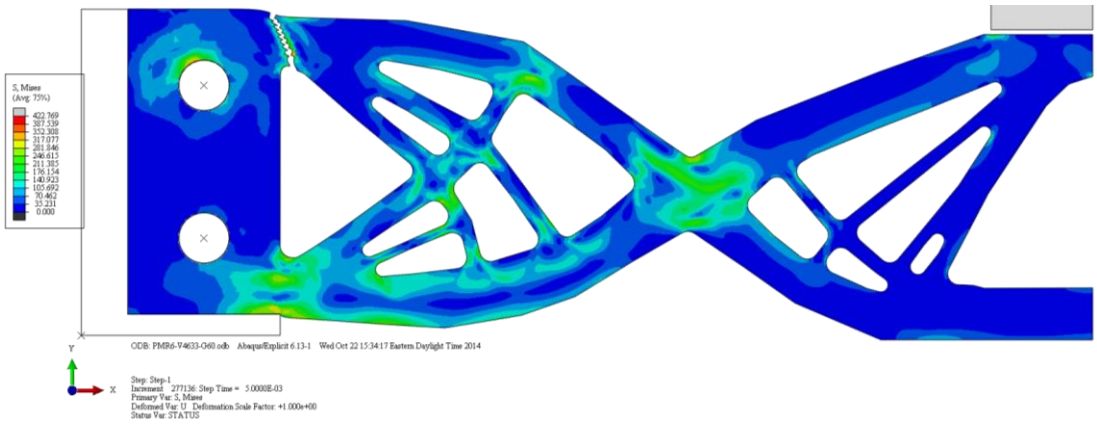

Figure 96- PMR6 - 5ms

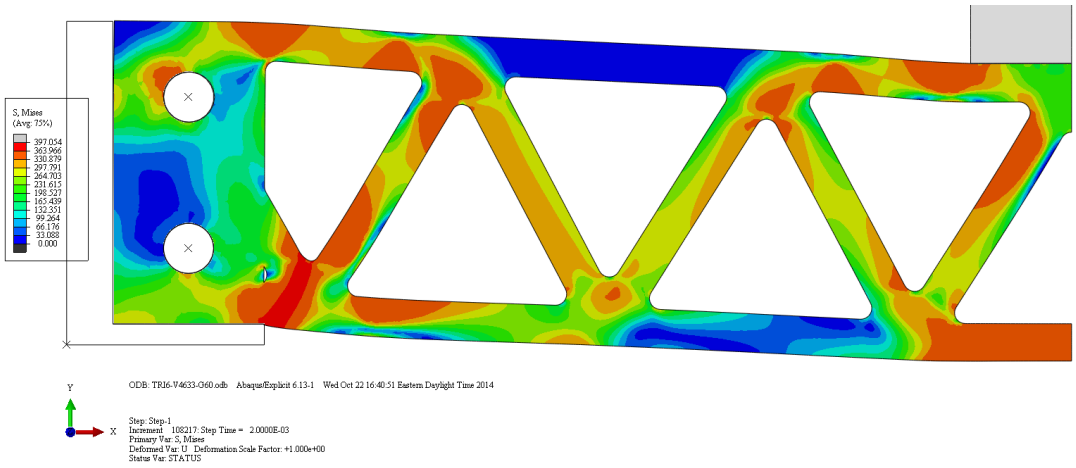

Figure 97 - TRI6 - 2ms

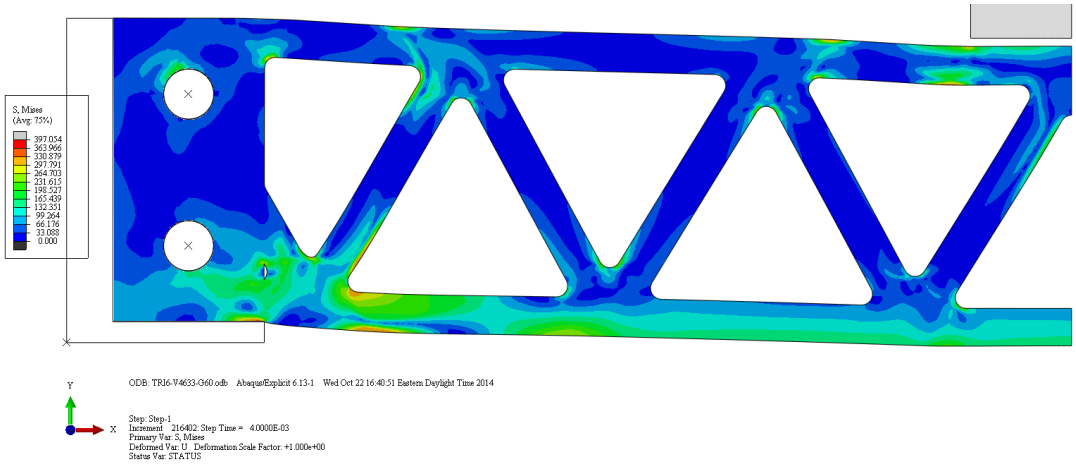

Figure 98 - TRI6 - 4ms

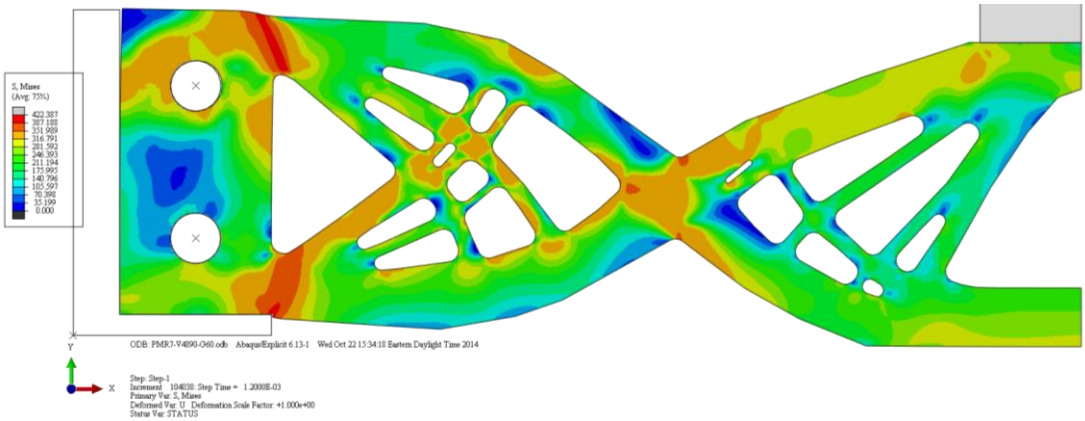

Figure 99 - PMR7 - 1.2ms

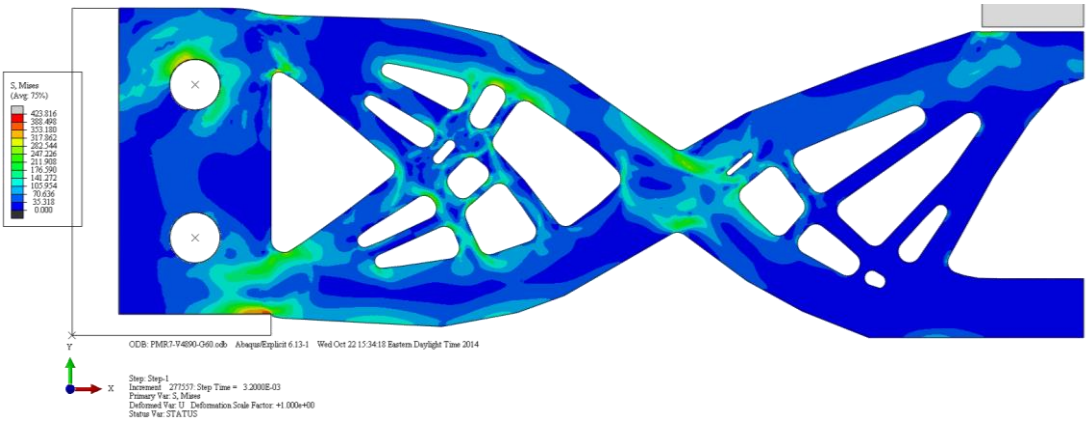

Figure 100 - PMR7 - 3.2ms

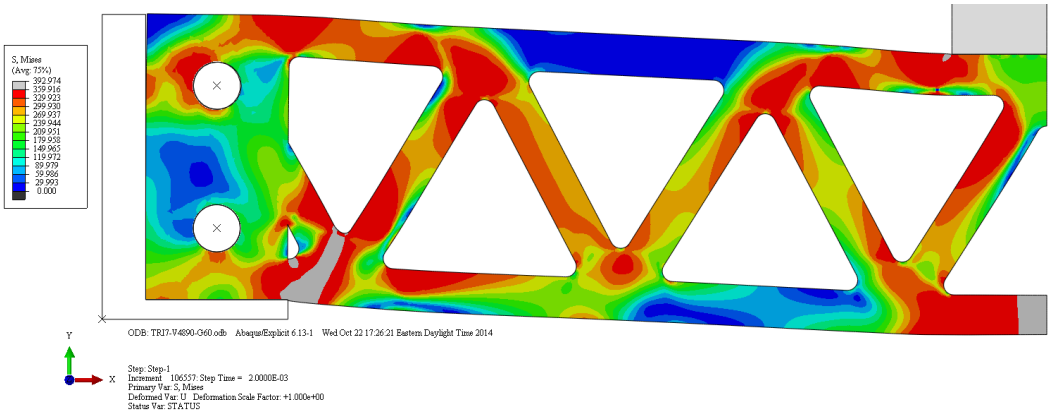

Figure 101 - TRI7 - 2ms

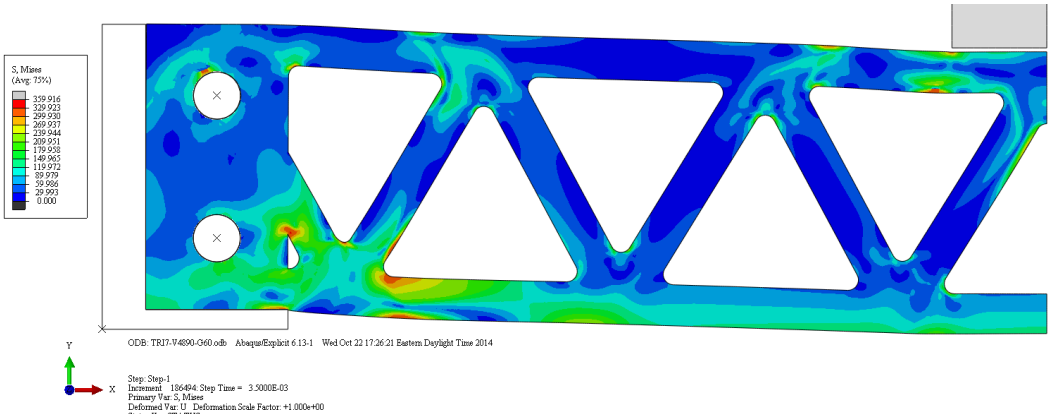

Figure 102 - TRI7 – 3.5ms

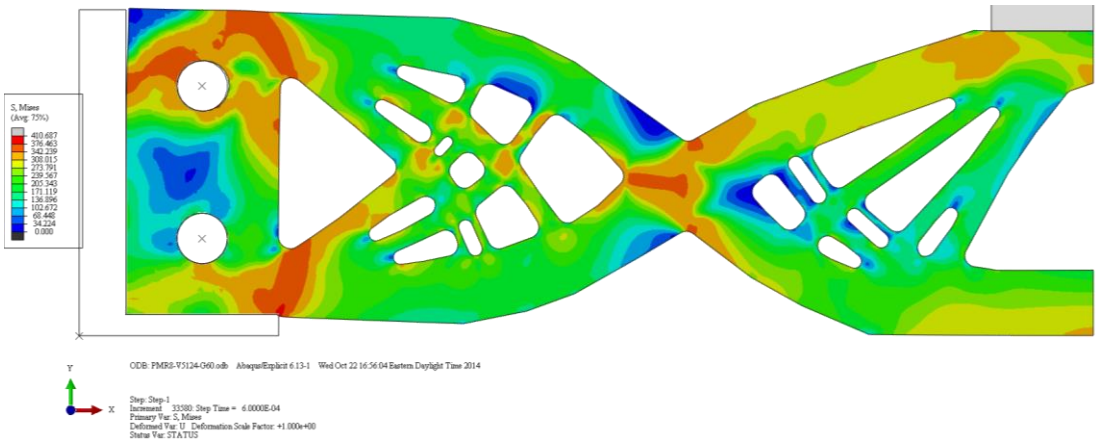

Figure 103 - PMR8 – 0.6ms

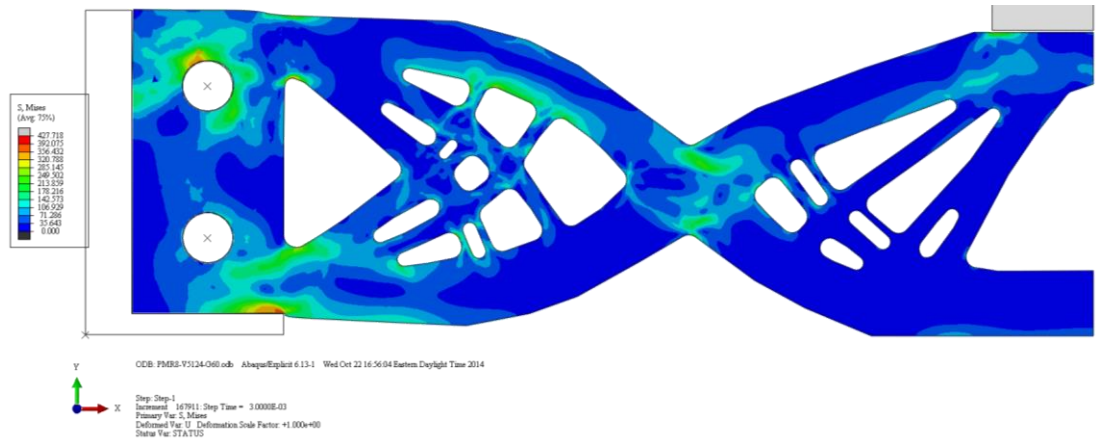

Figure 104- PMR8 – 3ms

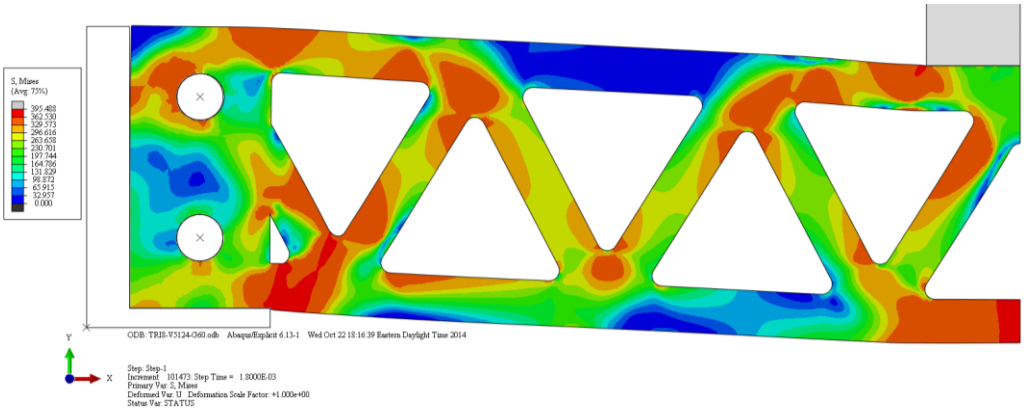

Figure 105 - TRI8 – 1.8ms

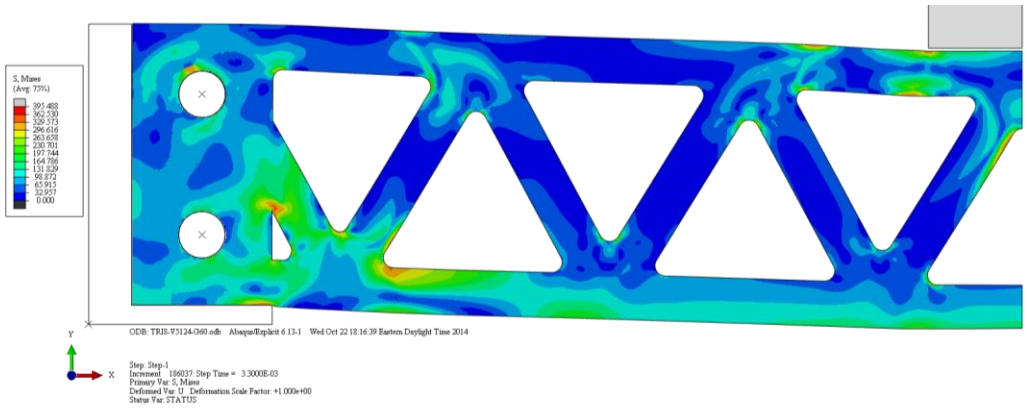

Figure 106- TRI8 – 3.3ms

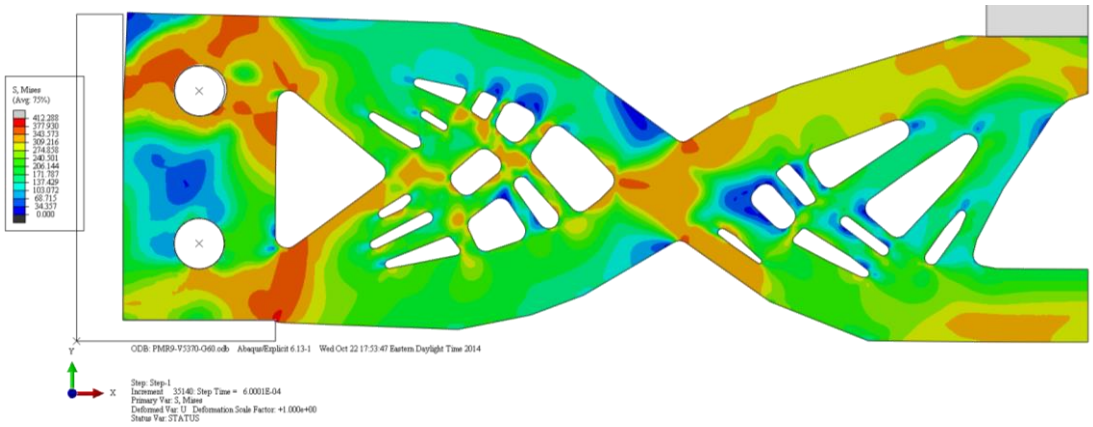

Figure 107- PMR9 – 0.6ms

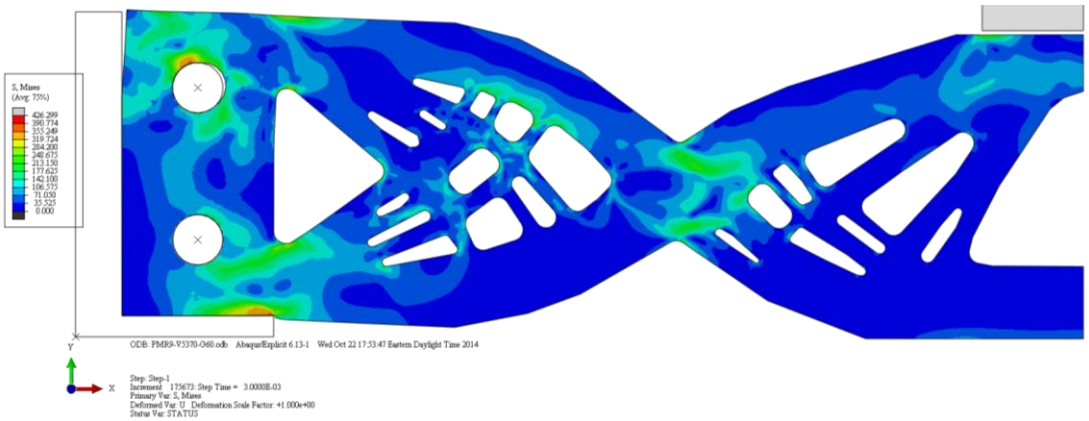

Figure 108 - PMR9 – 3ms

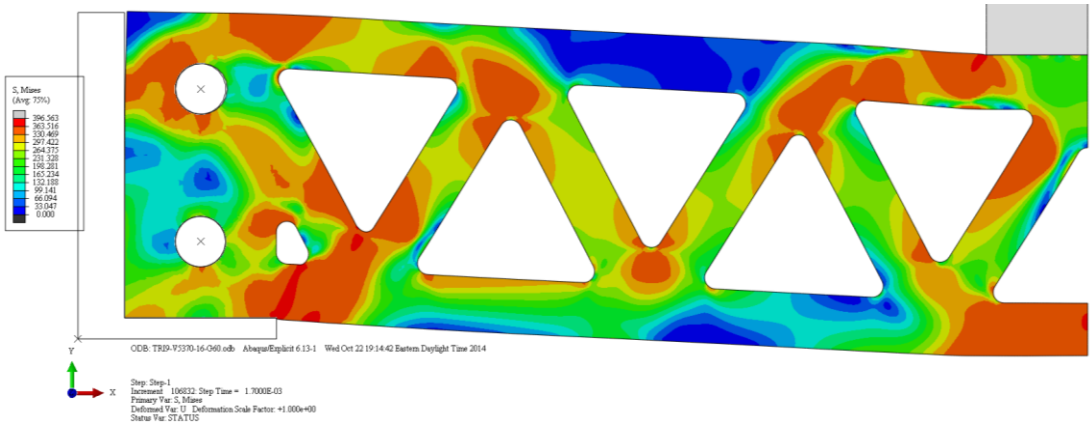

Figure 109 - TRI9 – 1.7ms

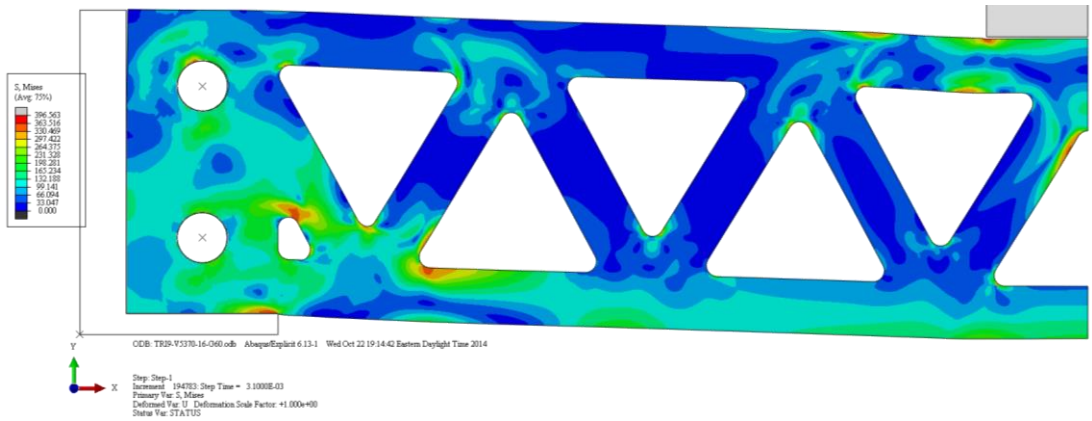

Figure 110 - TRI9 – 3.1ms

APPENDIX 2: Abaqus Input Script

```
*Heading
** Job name: TRI2-V3475 Model name: Model-1
** Generated by: Abaqus/CAE 6.13-1
*Preprint, echo=NO, model=NO, history=NO, contact=NO
** PARTS
*Part, name=fixture
*End Part
**
*Part, name=sample
*Element, type=CPS4R
*Nset, nset=sampleXsym
   45,   46,   50,   51, 1835, 1836, 1837, 1838, 1839, 1840,
1841, 1842, 2013, 2014, 2015, 2016
 2017, 2018, 2019, 2020, 2021, 2022, 2023, 2024, 2025, 2026,
2027, 2028
*Elset, elset=sampleXsym
 3592, 3595, 3836, 3838, 3844, 3848, 3852, 3856, 3860, 3864,
3865, 6858, 6859, 6860, 6861, 6862
 6863, 6905, 6907, 6908, 6909, 7189, 8796, 8799, 8800, 8804
*Nset, nset=wholesample, generate
     1,  16132,      1
*Elset, elset=wholesample, generate
     1,  14832,      1
*Nset, nset=topmid
 51,
*Nset, nset=botmid
 45,
** Section: AL
*Solid Section, elset=wholesample, controls=EC-1, material="AL
6061-T6mm Rule G375"
12.7,
*End Part
*Part, name=striker
*End Part
*Part, name=strikerhead
*Element, type=CPS3

** Section: steel
*Solid Section, elset=Set-1, controls=EC-2, material="AISI4340
E"
12.7,
*End Part
**
*Part, name=topbolt
*Element, type=R2D2
*End Part
** ASSEMBLY
*Assembly, name=Assembly
*Instance, name=Tri-1, part=sample
```

```
  -70.374997,      -22.775,           0.
*End Instance
*Instance, name=striker-1, part=striker
       122.6,      144.075,           0.
*Node
      1,   -2.4749999,         6.25,           0.
*Nset, nset=striker-1-RefPt_, internal
1,
*Nset, nset=_PickedSet11, internal
 1,
*Surface, type=SEGMENTS, name=bottom
START,       -8.825,         6.25
 LINE,        3.875,         6.25
 LINE,        3.875,        -1.75
 LINE,       -8.825,        -1.75
 LINE,       -8.825,         6.25
*Rigid Body, ref node=striker-1-RefPt_, analytical
surface=bottom
*Element, type=MASS, elset=_PickedSet11_Inertia-1_MASS_
1, 1
*Mass, elset=_PickedSet11_Inertia-1_MASS_
0.0060155,
*Element, type=ROTARYI, elset=_PickedSet11_Inertia-1_ROTI_
2, 1
*Rotary Inertia, elset=_PickedSet11_Inertia-1_ROTI_
1., 1., 1., 0., 0., 0.
*End Instance
**
*Instance, name=strikerhead-1, part=strikerhead
     113.775,      129.625,           0.
*End Instance
**
*Instance, name=fixture-1, part=fixture
      24.875,        2.625,           0.
*Node
      1,      -24.875,       -2.625,           0.
*Nset, nset=fixture-1-RefPt_, internal
1,
*Surface, type=SEGMENTS, name=leftbottom
START,       -19.05,           0.
 LINE,           0.,           0.
 LINE,           0.,       -2.625
 LINE,      -24.875,       -2.625
 LINE,      -24.875,         38.1
 LINE,       -19.05,         38.1
 LINE,       -19.05,           0.
*Rigid Body, ref node=fixture-1-RefPt_, analytical
surface=leftbottom
*End Instance
**
*Instance, name=topbolt-1, part=topbolt
       15.35,         31.2,           0.
```

```
*End Instance
**
*Instance, name=bottombolt, part=topbolt
       15.35,        12.15,           0.
*End Instance
*End Assembly
**
** ELEMENT CONTROLS
**
*Section Controls, name=EC-1, DISTORTION CONTROL=YES, ELEMENT
DELETION=YES, hourglass=ENHANCED, second order accuracy=YES
1., 1., 1.
*Section Controls, name=EC-2, second order accuracy=YES
1., 1., 1.
**
** MATERIALS
**
** Steel AISI 4340 Elastic mm
*Material, name="AISI4340 E"
*Density
 7.75e-09,
*Elastic
205000., 0.3
** Aluminum 6061-T6 units mm Ref Rule
*Material, name="AL 6061-T6mm Rule G375"
*Damage Initiation, criterion=JOHNSON COOK
 -0.77, 1.45, 0.47,   0.,  1.6, 925., 294.,   1.
*Damage Evolution, type=ENERGY
60.,
*Density
 2.69e-09,
*Elastic
69000., 0.33
*Plastic, hardening=JOHNSON COOK
324.,  114.,  0.42,    0.,  925., 293.2
*Rate Dependent, type=JOHNSON COOK
 0.002,1.
**
** INTERACTION PROPERTIES
**
*Surface Interaction, name=Contact
*Friction
 0.61,
*Surface Behavior, pressure-overclosure=HARD
*Time Points, name=Coarse, GENERATE
0., 3e-05, 1e-06
3e-05, 0.0001, 2e-06
0.0001, 0.025, 0.0001
*Time Points, name=Fine, GENERATE
0., 0.001, 1e-05
0.001, 0.005, 1e-05
0.005, 0.025, 0.0005
```

```
**
** PREDEFINED FIELDS
**
** Name: Predefined Field-1   Type: Velocity
*Initial Conditions, type=VELOCITY
Set-10, 1, 0.
Set-10, 2, -3475.
** ----------------------------------------------------------------
----
**
** STEP: Step-1
**
*Step, name=Step-1, nlgeom=YES
*Dynamic, Explicit
, 0.012
*Bulk Viscosity
0.06, 1.2
**
** BOUNDARY CONDITIONS
**
** Name: SampleXsym Type: Symmetry/Antisymmetry/Encastre
*Boundary
Tri-1.sampleXsym, XSYMM
** Name: encastre Type: Symmetry/Antisymmetry/Encastre
*Boundary
Set-17, ENCASTRE
** Name: xsym Type: Symmetry/Antisymmetry/Encastre
*Boundary
Set-19, XSYMM
** Name: zsym Type: Symmetry/Antisymmetry/Encastre
*Boundary
Set-18, ZSYMM
**
** LOADS
**
** Name: Load-1   Type: Gravity
*Dload
, GRAV, 9810., 0., -1.
**
** INTERACTIONS
**
** Interaction: Leftbottom
*Contact Pair, interaction=Contact, mechanical
constraint=KINEMATIC, cpset=Leftbottom
fixture-1.leftbottom, Tri-1.leftbottom
** Interaction: bottomhole
*Contact Pair, interaction=Contact, mechanical
constraint=KINEMATIC, cpset=bottomhole
bottombolt.boltsurf, Tri-1.bottomhole
** Interaction: contact
*Contact Pair, interaction=Contact, mechanical
constraint=KINEMATIC, cpset=contact
```

```
strikerhead-1.strikerplatebot, Tri-1.sampetop
** Interaction: tophole
*Contact Pair, interaction=Contact, mechanical
constraint=KINEMATIC, cpset=tophole
topbolt-1.boltsurf, Tri-1.tophole
**
** OUTPUT REQUESTS
**
*Restart, write, number interval=1, time marks=NO
**
** FIELD OUTPUT: F-Output-1
**
*Output, field, time points=Coarse
*Node Output, nset=Tri-1.wholesample
U,
*Element Output, elset=Tri-1.wholesample, directions=YES
EDCDEN, EDT, ELEDEN, ELEN, ENER, ER, LE, MISES, PEEQ, S,
STATUS, TRIAX
**
** FIELD OUTPUT: Loadcell
**
*Output, field, time points=Fine
*Node Output, nset=Set-6
A, U, V
**
** HISTORY OUTPUT: striker
**
*Output, history
*Energy Output, elset=strikerwhole
ALLAE, ALLCD, ALLCW, ALLDC, ALLDMD, ALLFD, ALLIE, ALLKE, ALLMW,
ALLPD, ALLPW, ALLSE, ALLVD, ALLWK, ETOTAL
**
** HISTORY OUTPUT: H-Output-1
**
*Output, history, variable=PRESELECT
**
** HISTORY OUTPUT: sample
**
*Output, history
*Node Output, nset=Tri-1.wholesample, variable=PRESELECT
*Element Output, elset=Tri-1.wholesample, variable=PRESELECT
*Integrated Output, elset=Tri-1.wholesample, variable=PRESELECT
*Energy Output, elset=Tri-1.wholesample, variable=PRESELECT
*Incrementation Output, variable=PRESELECT
*End Step
```

APPENDIX 3: PMR Matlab Input File

```
function PMR_threepointbend
clc; clear all; close all
%60 elements per inch
t=0; %thickness of outline
w=30; %striker half width 0.5 inches
nelx=240; %base half width
nely=90; %domain height
vol_frac=.3;

%clear common variables between cases to prevent contamination
clear fixeddofs F node_type node_F node inode jnode design_node_flag
x y dense_node
global fixeddofs F node_type
%ForceD=.01; %40 nodes on top

iter=100;
%
F=sparse(2*(nely+1)*(nelx+1),1);
%node numbers for top pressure load
node_F = (1+(nely+1)*(nelx-w)):(nely+1):(1+(nely+1)*(nelx));

% fixeddofs=[2*nely,2*nely+1,2*(nelx+1)*(nely+1)-
1,2*(nelx+1)*(nely+1)];

%fixes left edge, then applies symetry in x to right edge
fixeddofs=[[1:1:2*(nely+1)],[(2*(nely+1)*nelx)+1:2:(2*(nelx+1)*(nely+
1)-1)]];
F(2*node_F,1)=-1;
%
% define node numbers
%
node=0;
for inode=1:nelx+1
    for jnode=1:nely+1
        node=node+1;
        x(node)=inode-1;
        y(node)=nely-(jnode-1);
        node_type(node)=1;
    end
end
design_node_flag=ones(node,1);
plot(x,y,'b.')
hold on
x0=mean(x);
y0=mean(y);
numdense=0;

if t>0
    for i=1:node
        if y(i)<=t||y(i)>=nely-t||x(i)<=t

            numdense=numdense+1;
            dense_node(numdense)=i;
```

```
            node_type(i)=3;
        end
    end

    % node_type'
    plot(x(dense_node(1:numdense)),y(dense_node(1:numdense)),'ko')
    axis equal
    figure
end
tic
pmr_3_2013_predefined_regions(nelx,nely,vol_frac,iter)
toc
filename=['L' num2str(nelx) '_h' num2str(nely) '_w' num2str(w) '_VF'
num2str(vol_frac) '.jpg'];
saveas(gcf,filename)
```

APPENDIX 4: Drawings

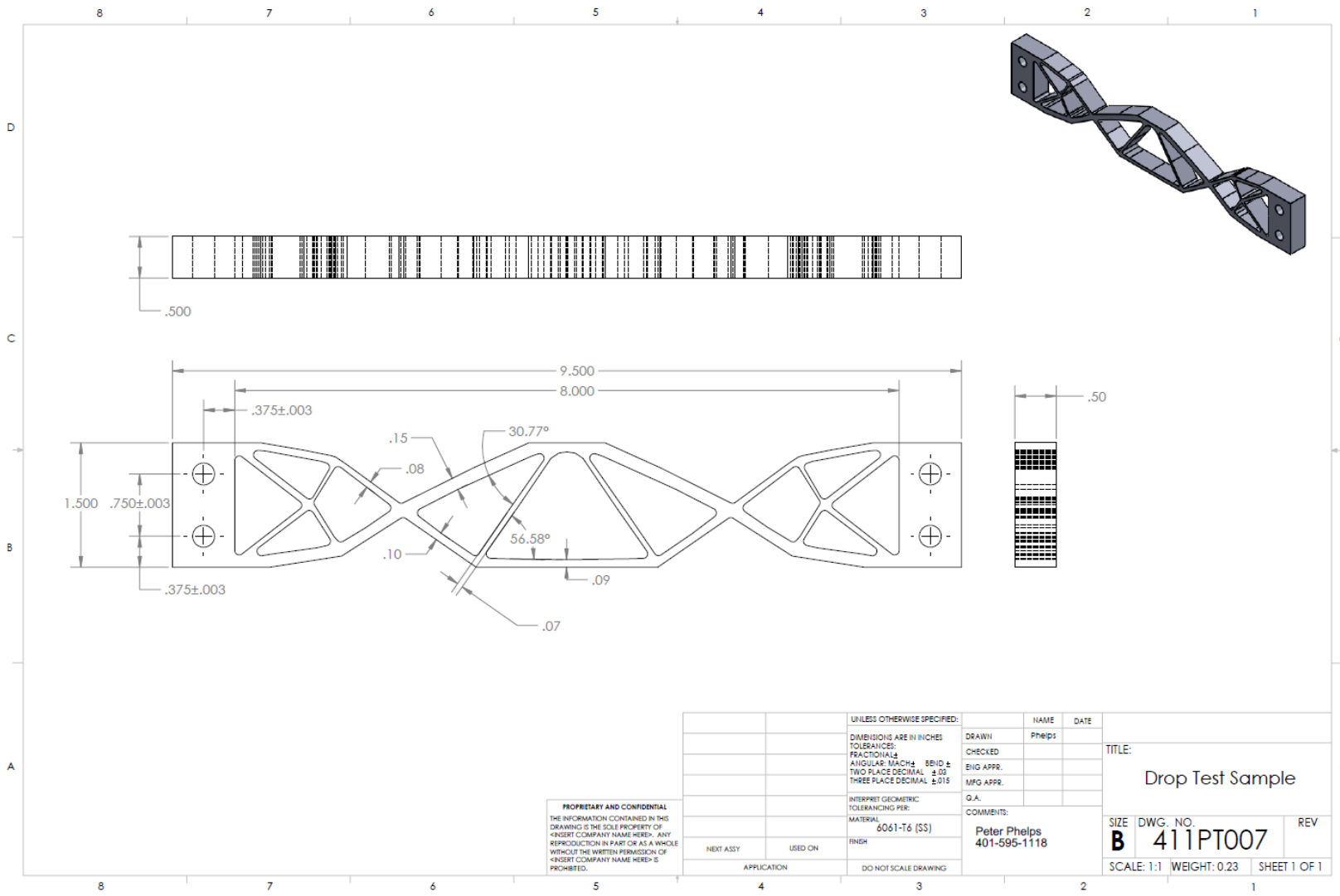
8
7
6
5
4
3
2
1
D
C
B
A
.500
9.500
8.000
.375±.003
.15
.08
30.77°
1.500
.750±.003
.10
56.58°
.09
.375±.003
.07
.50
PROPRIETARY AND CONFIDENTIAL
THE INFORMATION CONTAINED IN THIS DRAWING IS THE SOLE PROPERTY OF <INSERT COMPANY NAME HERE>. ANY REPRODUCTION IN PART OR AS A WHOLE WITHOUT THE WRITTEN PERMISSION OF <INSERT COMPANY NAME HERE> IS PROHIBITED.
NEXT ASSY
USED ON
APPLICATION
UNLESS OTHERWISE SPECIFIED:
DIMENSIONS ARE IN INCHES
TOLERANCES:
FRACTIONAL ±
ANGULAR: MACH ± BEND ±
TWO PLACE DECIMAL ±.02
THREE PLACE DECIMAL ±.015
INTERPRET GEOMETRIC TOLERANCING PER:
MATERIAL
6061-T6 (SS)
FINISH
DO NOT SCALE DRAWING
NAME
DATE
DRAWN
Phelps
CHECKED
ENG APPR.
MFG APPR.
Q.A.
COMMENTS:
Peter Phelps
401-595-1118
TITLE:
Drop Test Sample
SIZE
B
DWG. NO.
411PT007
REV
SCALE: 1:1
WEIGHT: 0.23
SHEET 1 OF 1

ITEM NO.	PART NUMBER	DESCRIPTION	QTY.
1	ASME B18.8.2 - 0.2502x1.5	Dowel Pin 1/4" x 1.5"	2
2	HX-SHCS 0.375-16x1.75x1.25-N	SHCS 3/8"-16 x 1.75"	4
3	91259A103	Shoulder Screw 1/4" x 2"	4
4	Preferred Narrow FW 0.25	Washer 1/4	8
5	HX-SHCS 0.375-16x3x1.5-N	SHCS 3/8"-16 x 1.5"	4
6	94831A011	Flange Hex Nut #10-24	4
7	Preferred Narrow FW 0.375	Washer 3/8	4
8	L240H90W30VF2fillet	Drop Test Sample	1
9	411PT010	Cross Bar	2
10	411PT009	End Block	2

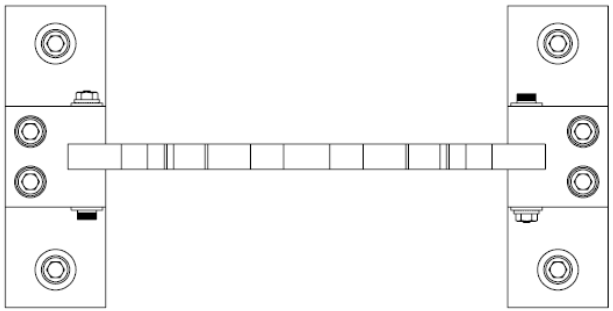

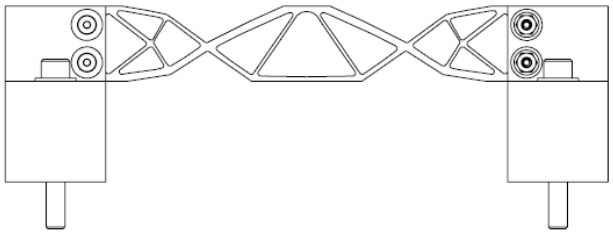

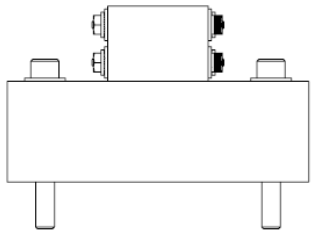

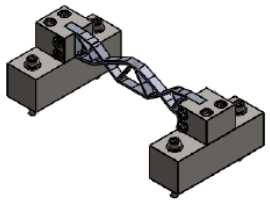

		UNLESS OTHERWISE SPECIFIED:		NAME	DATE
		DIMENSIONS ARE IN INCHES TOLERANCES: FRACTIONAL ± ANGULAR: MACH ± BEND ± TWO PLACE DECIMAL ±.03 THREE PLACE DECIMAL ±.015	DRAWN	Phelps	
			CHECKED		
			ENG APPR.		
			MFG APPR.		
		INTERPRET GEOMETRIC TOLERANCING PER:	Q.A.		
		MATERIAL	COMMENTS:		
NEXT ASSY	USED ON	FINISH	Peter Phelps 401-595-1118		
APPLICATION		DO NOT SCALE DRAWING			

TITLE: Drop Fixture

SIZE	DWG. NO.	REV
B	411PT008	

SCALE: 1:2 | WEIGHT: | SHEET 1 OF 2

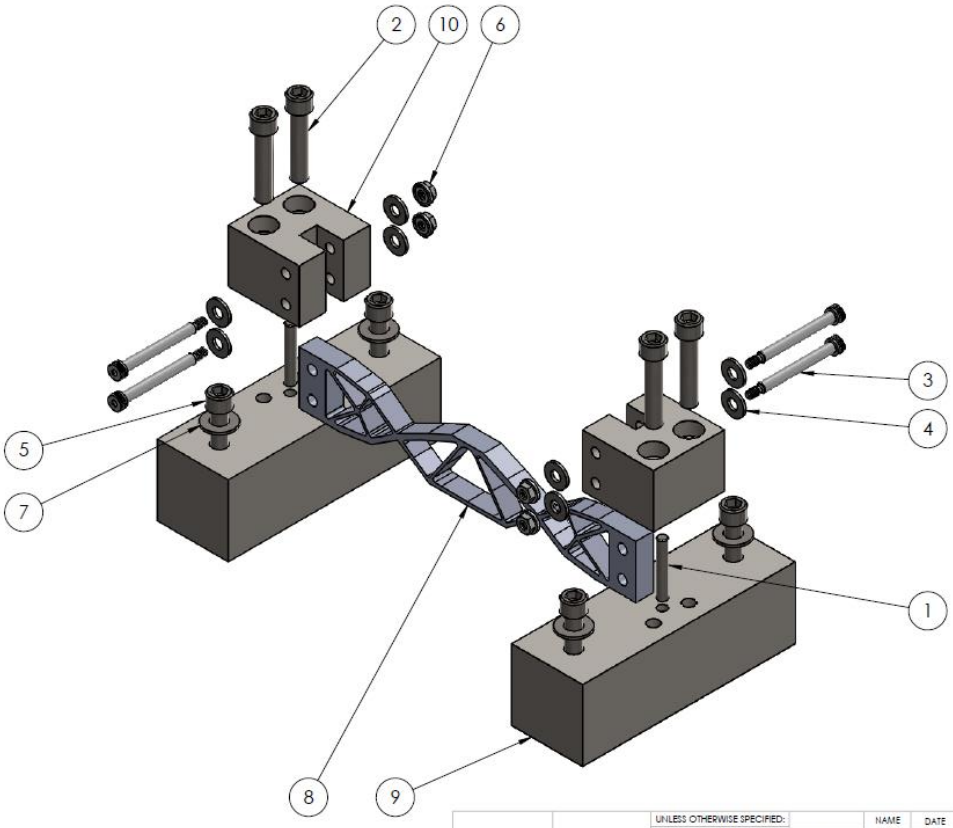

		UNLESS OTHERWISE SPECIFIED:		NAME	DATE
		DIMENSIONS ARE IN INCHES TOLERANCES: FRACTIONAL ± ANGULAR: MACH ± BEND ± TWO PLACE DECIMAL ±.03 THREE PLACE DECIMAL ±.015	DRAWN	Phelps	
			CHECKED		
			ENG APPR.		
			MFG APPR.		
		INTERPRET GEOMETRIC TOLERANCING PER:	Q.A.		
		MATERIAL	COMMENTS:		
		FINISH	Peter Phelps 401-595-1118		
NEXT ASSY	USED ON				
APPLICATION		DO NOT SCALE DRAWING			

TITLE: Drop Fixture

SIZE	DWG. NO.	REV
B	411PT008	

SCALE: 1:2 | WEIGHT: | SHEET 2 OF 2

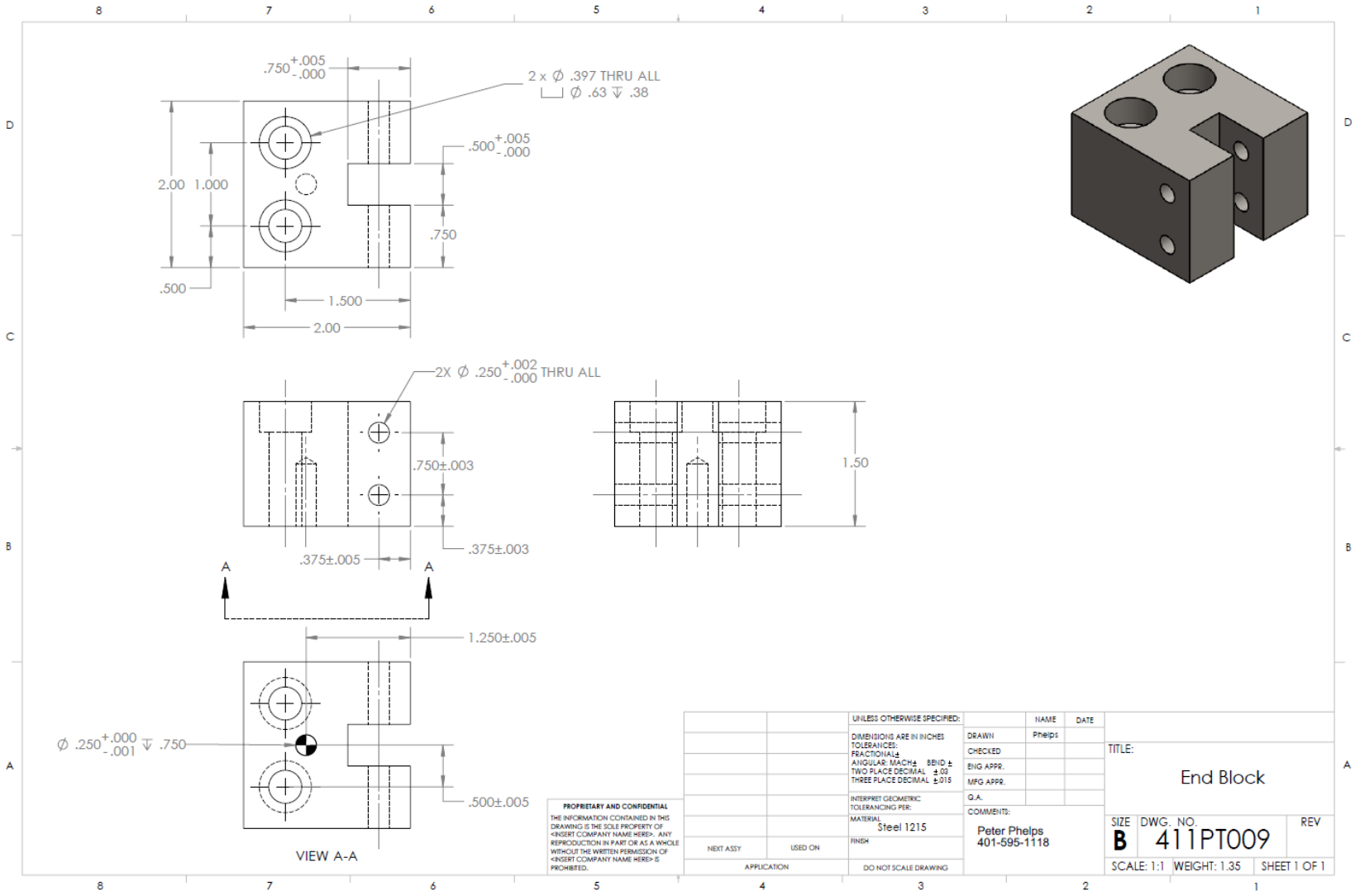
.750 +.005 -.000
2 x Ø .397 THRU ALL
⌴ Ø .63 ↧ .38
.500 +.005 -.000
2.00
1.000
.750
.500
1.500
2.00
2X Ø .250 +.002 -.000 THRU ALL
.750±.003
.375±.005
.375±.003
1.50
A
A
1.250±.005
Ø .250 +.000 -.001 ↧ .750
.500±.005
VIEW A-A
PROPRIETARY AND CONFIDENTIAL
THE INFORMATION CONTAINED IN THIS DRAWING IS THE SOLE PROPERTY OF <INSERT COMPANY NAME HERE>. ANY REPRODUCTION IN PART OR AS A WHOLE WITHOUT THE WRITTEN PERMISSION OF <INSERT COMPANY NAME HERE> IS PROHIBITED.
UNLESS OTHERWISE SPECIFIED:
DIMENSIONS ARE IN INCHES
TOLERANCES:
FRACTIONAL
ANGULAR: MACH BEND ±
TWO PLACE DECIMAL ±.03
THREE PLACE DECIMAL ±.015
INTERPRET GEOMETRIC TOLERANCING PER:
MATERIAL
Steel 1215
FINISH
NEXT ASSY
USED ON
APPLICATION
DO NOT SCALE DRAWING
NAME
DATE
DRAWN
Phelps
CHECKED
ENG APPR.
MFG APPR.
Q.A.
COMMENTS:
Peter Phelps
401-595-1118
TITLE:
End Block
SIZE
B
DWG. NO.
411PT009
REV
SCALE: 1:1
WEIGHT: 1.35
SHEET 1 OF 1

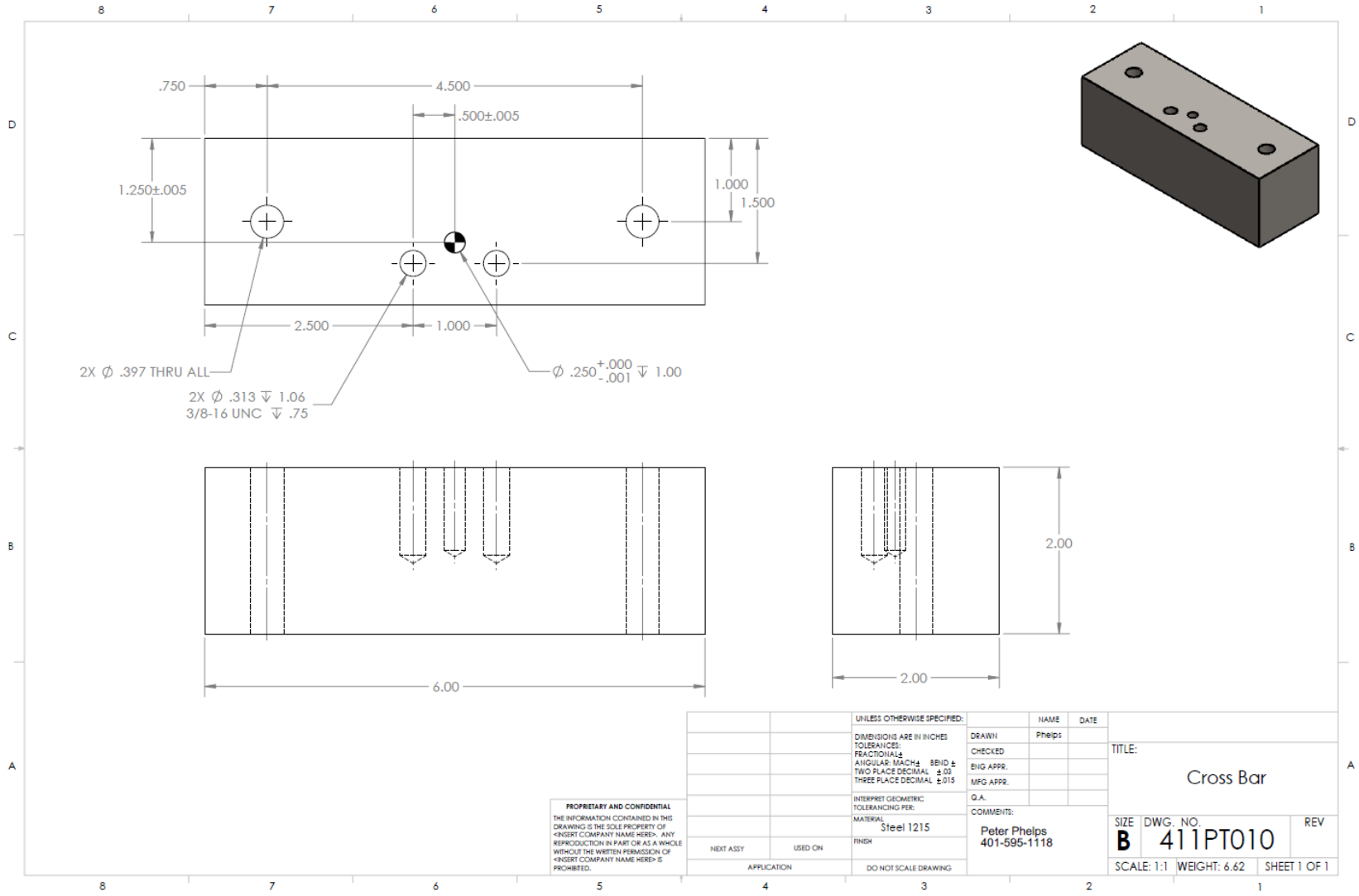
.750
4.500
.500±.005
1.250±.005
1.000
1.500
2.500
1.000
2X Ø .397 THRU ALL
2X Ø .313 ↧ 1.06
3/8-16 UNC ↧ .75
Ø .250 +.000 -.001 ↧ 1.00
2.00
6.00
2.00
UNLESS OTHERWISE SPECIFIED:
DIMENSIONS ARE IN INCHES
TOLERANCES:
FRACTIONAL ±
ANGULAR: MACH ± BEND ±
TWO PLACE DECIMAL ±.03
THREE PLACE DECIMAL ±.015
INTERPRET GEOMETRIC TOLERANCING PER:
MATERIAL
Steel 1215
FINISH
NEXT ASSY
USED ON
APPLICATION
DO NOT SCALE DRAWING
NAME
DATE
DRAWN
Phelps
CHECKED
ENG APPR.
MFG APPR.
G.A.
COMMENTS:
Peter Phelps
401-595-1118
PROPRIETARY AND CONFIDENTIAL
THE INFORMATION CONTAINED IN THIS DRAWING IS THE SOLE PROPERTY OF <INSERT COMPANY NAME HERE>. ANY REPRODUCTION IN PART OR AS A WHOLE WITHOUT THE WRITTEN PERMISSION OF <INSERT COMPANY NAME HERE> IS PROHIBITED.
TITLE:
Cross Bar
SIZE
B
DWG. NO.
411PT010
REV
SCALE: 1:1
WEIGHT: 6.62
SHEET 1 OF 1

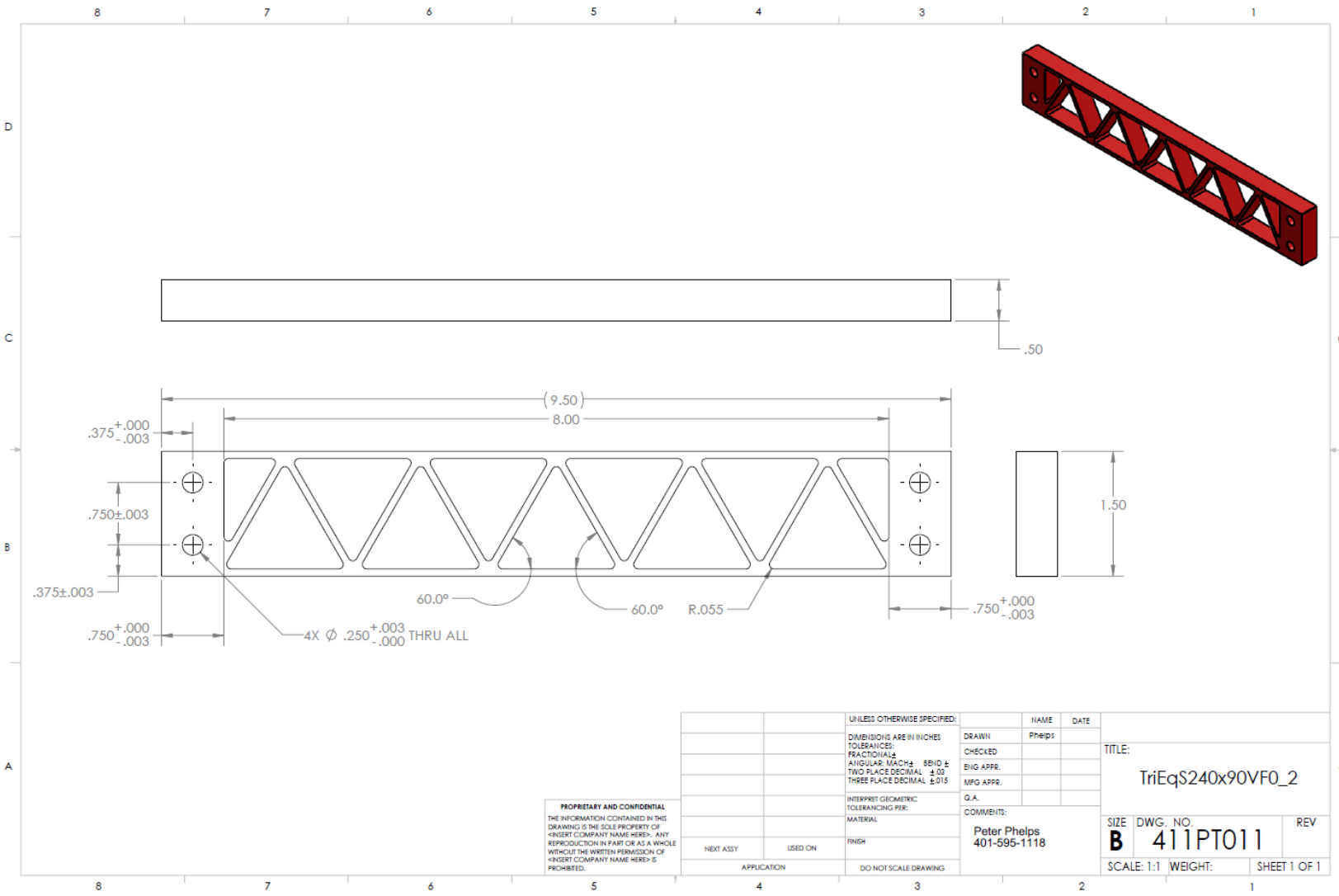
8
7
6
5
4
3
2
1
D
C
B
A
.50
(9.50)
8.00
.375 +.000 -.003
.750±.003
.375±.003
.750 +.000 -.003
4X Ø .250 +.003 -.000 THRU ALL
60.0°
60.0°
R.055
1.50
.750 +.000 -.003
PROPRIETARY AND CONFIDENTIAL
THE INFORMATION CONTAINED IN THIS DRAWING IS THE SOLE PROPERTY OF <INSERT COMPANY NAME HERE>. ANY REPRODUCTION IN PART OR AS A WHOLE WITHOUT THE WRITTEN PERMISSION OF <INSERT COMPANY NAME HERE> IS PROHIBITED.
NEXT ASSY
USED ON
APPLICATION
UNLESS OTHERWISE SPECIFIED:
DIMENSIONS ARE IN INCHES
TOLERANCES:
FRACTIONAL ±
ANGULAR: MACH ± BEND ±
TWO PLACE DECIMAL ±.03
THREE PLACE DECIMAL ±.015
INTERPRET GEOMETRIC TOLERANCING PER:
MATERIAL
FINISH
DO NOT SCALE DRAWING
NAME
DATE
DRAWN
Phelps
CHECKED
ENG APPR.
MFG APPR.
Q.A.
COMMENTS:
Peter Phelps
401-595-1118
TITLE:
TriEqS240x90VF0_2
SIZE
B
DWG. NO.
411PT011
REV
SCALE: 1:1
WEIGHT:
SHEET 1 OF 1

BIBLIOGRAPHY

ASM Aerospace Specification Metals Inc. *AISI 4340 Steel.* MatWeb LLC. n.d. http://asm.matweb.com/search/SpecificMaterial.asp?bassnum=M434AA (accessed October 2, 2014).

ASM Aerospace Specification Metals Inc. *Aluminum 6061-T651.* MatWeb LLC. n.d. http://asm.matweb.com/search/SpecificMaterial.asp?bassnum=MA6061t6 (accessed October 2, 2014).

Bendsoe, M., Kikuchi, N. "Generating Optimal Topologies in Structural Design using a Homogenization Method." *Computer Methods in Applied Mechanics and Engineering*, 1988: 197-224.

Budynas, Nisbett. *Shigley's Mechanical Engineering Design.* McGraw Hill, 2008.

Chan, A.,. *"The design of Michell optimum structures" Report No. 142.* Cranfield UK: College of Aeronautics, December 1960.

Johnson G., Cook W. "Fracture Characteristics of Three Metals Subjected to Various Strains, Strain Rates, Temperatures and Pressures." *Engineering Fracture Mechanics* 21, no. No. 1 (1985): 31-48.

Lesuer D., Kay G., LeBlanc M. "Modeling Large-Strain, High-Rate Deformation in Metals." *Third Biennial Tri-Laboratory Engineering Conference Modeling and Simulation.* Pleasanton, CA, 2001.

Michell, A. "The Limits of Economy of Material in Frame Structures." *Philosophical Magazine*, 1904: 589-597.

Okruta, Matt. *Three-Dimensional Topology Optimization of Statically Loaded Porous and Multi-Phase Structures.* M.S. Thesis, University of Rhode Island, 2014.

Rozvany, G., Zhou, M., Birker, T. "Generalized shape optimization without homogenization." *Structural Optimization*, 1992: 250-252.

Serway, Raymond. *Physics for Scientists & Engineers.* Orlando: Saunders College Publishing, 1997.

Shukla, Arun. *Practical Fracture Mechanics in Design.* New York: marcel Dekker, 2005.

Simulia. *Abaqus 6.13 Analysis User's Guide Volume III: Materials.* Providence, RI: Dassault Systems, 2013.

Taggart, D.G., Dewhurst, P., Dobrot, L., Gill, D.D. "Development of a Beta Function Based Topology Optimization Procedure." *Abaqus Users Conference.* Newport, RI, 2008.

Taggat, D.G., Dewhurst, P. "Development and validatino of a numerical topology optimization scheme for two and three dimensional structures." *Advances in Engineering Software*, 2010: 910-915.

Xie, Y., Steven, G. "A Simple Evolutionary Procedure for Structural Optimization." *Computers and Structures*, 1993: 885-896.